AN EXPERIMENTAL STUDY OF THERMAL CONVECTION IN A ROTATING LIQUID

By R. HIDE*

Department of Geodesy and Geophysics, University of Cambridge

(*Communicated by R. Stoneley, F.R.S.—Received* 21 *June* 1957—*Revised* 20 *November* 1957—*Read* 6 *February* 1958)

[Plates 5 to 12]

CONTENTS

An investigation is described of the hydrodynamical flow that ensues when a liquid which rotates uniformly at Ω rad/s about a vertical axis is subject to a horizontal temperature gradient. Although Ω was sufficiently large for primary effects due to Coriolis forces to arise, centripetal forces never exceeded a small fraction of those due to gravity. Laboratory investigations of this type are of some geophysical interest. They may have a direct bearing on the study of the general atmospheric circulation, and with suitable extensions they may eventually lead to a better understanding of the hydrodynamical flow which is supposed to occur in the earth's liquid core, where the geomagnetic field originates.

Water, the only liquid which was used, filled the annular space between two concentric cylinders of radii a and b $(b>a)$ to a depth of d cm. The cylinders were maintained at different temperatures T_a and T_b. The general properties of the flow depend on the value of a certain parameter

$$\Theta \equiv 2gd[\rho(T_a)-\rho(T_b)]/\Omega^2(b-a)^2\,[\rho(T_b)+\rho(T_a)],$$

where g is the acceleration of gravity and $\rho(T)$ is the density of water at temperature T. When Θ exceeds a certain value, $\Theta_{\text{crit.}}$, the flow is essentially a meridional circulation, in which the motion perpendicular to the axis of rotation is deflected by Coriolis forces. When Θ is somewhat less than $\Theta_{\text{crit.}}$ the flow is characterized by a regular quasi-horizontal wave-like pattern in which the motion is almost but not entirely confined to a thin meandering 'jet' stream. The transition between these two régimes of flow takes place quite sharply when $\Theta = \Theta_{\text{crit.}} = 1{\cdot}58 \pm 0{\cdot}05$.

The train of waves in the wave-flow régime drifts relative to the rotating system at a uniform angular rate, in the same general direction as that of the flow in the top surface 'jet' stream. The wave number m increases as Θ decreases, until a certain point is reached, corresponding to an amplitude to wavelength ratio of about two-thirds, when no further increase in m can be produced by reducing Θ. At this point a steady repeating fluctuation of the flow pattern occurs. This phenomenon has been termed 'vacillation'. At even smaller values of Θ the flow is 'turbulent' in the sense that rapid and complicated fluctuations occur.

These flow phenomena appear to have their counterparts in the general atmospheric circulation.

Specific investigations are described, including heat transport measurements and a study of the thermal structure of a typical flow field. Theoretical considerations lead to an interpretation of the

* Now at the Department of Physics, King's College, Newcastle upon Tyne, 1.

meaning of Θ, which is tentatively identified with appropriate Rossby and Richardson numbers, and some of the results of theories due to Davies (1956) and Kuo (1953) are compared with the experimental measurements. A certain measure of agreement is found.

1. Introduction

The problem of the origin of the earth's main magnetic field is even now incompletely solved, although recent advances in geophysics have been responsible for considerable progress towards a solution. The main geomagnetic field originates within the earth, and it is almost certainly due to ordinary electric currents. Further evidence strongly suggests that these currents are generated by fluid motions in the earth's liquid core, so that the understanding of the hydrodynamics of the core will be an essential step towards an adequate theory of geomagnetism.

The detailed arguments leading to the foregoing statements have been reviewed recently (Inglis 1955; Hide 1956; Elsasser 1956) and need not be repeated here. Briefly, although it has not yet proved possible to establish the nature of the cause of core motions, it is not unlikely that these motions are thermally driven, perhaps by radioactive heating. Order-of-magnitude estimates of forces involved in the dynamical equations governing the flow suggest that in the core Coriolis forces due to the earth's rotation, and hydromagnetic forces due to inductive interaction between the moving fluid conductor and a magnetic field, are likely to be dynamically more important than inertial and viscous forces. Thus, the study of thermal convection in a rotating, electrically conducting fluid in the presence of a magnetic field is likely to yield results which bear *inter alia* on the hydrodynamics of the earth's core and on geomagnetism.

The experiments described in this paper were begun in 1950 at the suggestion of Dr S. K. Runcorn, hoping that they would lead to a better understanding of core hydrodynamics. No claim is made to have even crudely 'modelled' the core. This would involve use of a conducting fluid in the presence of a strong magnetic field, a future step which might be made when the influence of Coriolis forces acting alone has been understood. And in the absence of a suitable method of simulating a gravitating fluid sphere in the laboratory, any laboratory model will differ from its prototype in an essential way.

(*a*) *Scope of the present work*

In most of the experiments here described, thermally induced flow in water contained between two concentric cylinders, radii a and b ($b>a$), was studied. The cylinders were mounted on a horizontal turn-table with their axis vertical. The turn-table could be rotated at eight different angular speeds of rotation, Ω, ranging from 0·86 to 8·23 rad/s. The space between the cylinders, which were sealed on to a flat base plate, was filled with water to a depth of d cm. In all the investigations conducted to date, the internal radius of the outer cylinder, b, was fixed at 4·85 cm. Several inner cylinders, of outside radius a cm, were employed, the range of a being from 1·06 to 3·54 cm. The depth of water, d, was varied from about 3 cm to 11 cm.

The two cylinders were maintained at different temperatures, T_b and T_a, by means of temperature baths containing water. Although it was possible to secure a temperature difference in excess of 40 °C in this way, rarely was such a high value imposed.

Techniques for rendering the flow visible were employed, and an optical device was used which allowed direct observations to be made as from a frame of reference rotating with the apparatus. Photographic observations, mainly of the top-surface flow pattern, were made.

Rough heat flow determinations were made and with apparatus designed specifically for the purpose an investigation of the temperature distribution in the convecting system was carried out.

Within the range of Ω studied the *form* of the flow pattern does not appear to depend on whether the outer cylinder is warmer or colder than the inner cylinder. The *direction* of the hydrodynamical flow relative to the rotating system does, however, depend on the sign of $T_b - T_a$. These facts lead to the conclusion that of the two agencies responsible for buoyancy effects, namely, gravity and centripetal forces, the latter is relatively unimportant.

The nature of the flow appears to depend on the value of a certain dimensionless parameter

$$\Theta \equiv \frac{2gd}{\Omega^2(b-a)^2}\left[\frac{\rho(T_a)-\rho(T_b)}{\rho(T_a)+\rho(T_b)}\right], \tag{1·1}$$

where $\rho(T)$ is the density of the water at temperature T. When Θ exceeds a certain value, $\Theta_{\text{crit.}}$, the flow is essentially meridional and resembles that in a Hadley cell (see below, §4 (*b*)). The main effect of rotation seems to be the deflexion of the motion perpendicular to the axis of rotation, which thus produces an azimuthal component of the flow velocity. However, when Θ is somewhat less than $\Theta_{\text{crit.}}$ the flow is then characterized by a top-surface flow pattern which has the form of a regular series of waves. The motion is almost, although not entirely, confined to a thin meandering 'jet' stream about a centimetre wide. The wave pattern persists at all depths, the motion being strongly, but not entirely, horizontal. The transition between these two types of flow takes place fairly suddenly at

$$\Theta = \Theta_{\text{crit.}} = 1{\cdot}58 \pm 0{\cdot}05 \text{ (standard error)}.$$

An important feature of the wave-flow régime is a steady drift of the whole pattern relative to the rotating system, in the same general direction as that of the flow in the top-surface 'jet' stream. This direction is westward or eastward according as the sign of $T_b - T_a$ is negative or positive.

The first effect of decreasing Θ from $\Theta_{\text{crit.}}$ is to increase m, the wave number. However, when m reaches that value for which the wave amplitude is about two-thirds of the wavelength, no further increase in m can be produced by reducing Θ. At this point, the regular drifting wave pattern gives way to a steady repeating fluctuation which has been termed 'vacillation'. At lower values of Θ rapid and complicated turbulent fluctuations arise.

Perhaps the most remarkable feature of these flow phenomena is that they appear to have their counterparts in the general circulation of the earth's atmosphere, which is thermally driven by solar radiation and strongly influenced by the earth's rotation.

There have been previous experimental investigations of thermal convection in rotating liquids. Although these investigations have one common feature—they were all attempts to simulate atmospheric motions in the laboratory—the earlier ones at least were otherwise unconnected, qualitative and hence of limited value (see Fultz 1951*a*). In 1946 Fultz and his collaborators at the University of Chicago began a determined attack on the problem of

simulating atmospheric motions in the laboratory, and these workers have subsequently reported a number of experiments, some of which are quantitative (Fultz 1949, 1951*a*, 1953, 1956; Long 1952).It was Dr Dave Fultz who, several months after the experiments described in this paper had been begun, drew the writer's attention to their possible bearing on the general atmospheric circulation.

This paper is made up as follows. In § 2 are made some general remarks on the dynamics of rotating fluids, leading to a discussion of dimensionless parameters through which the physical significance of Θ emerges. Apparatus and techniques are described in § 3, and in § 4 an account of the main flow phenomena, illustrated by photographs, is given. The initial observations of these phenomena led to a series of quantitative experiments, described in § 5 and discussed in § 6.

Brief reports on this work have already been published (Hide 1953*a*, *b*; Runcorn 1954).

2. Some general comments on the dynamics of rotating fluids

Although the experiments were begun with virtually no idea of what was to be expected, as they progressed it became evident that the parameter Θ, formed by combining the variables at one's disposal in a particular way (see equation (1·1)), is important. The physical significance of Θ is probably best understood in terms of the general ideas presented in this section.

The equation of motion governing the flow of an incompressible fluid of density ρ and kinematical viscosity ν relative to a system rotating at $\boldsymbol{\Omega}$ rad/s is

$$\rho\left[\frac{\partial \mathbf{u}}{\partial t}+(\mathbf{u}.\nabla)\,\mathbf{u}+2\boldsymbol{\Omega}\times\mathbf{u}\right]=-\nabla p+\rho\nabla\Phi+\nu\rho\nabla^2\mathbf{u}, \tag{2·1}$$

where $\mathbf{u}$ is the velocity of the fluid at a point fixed in the rotating frame, and p is the pressure. Φ is the potential of external forces: in the case of a rotating system to ordinary gravity must be added centrifugal effects.

The continuity of matter requires that

$$\nabla.\mathbf{u}=0, \tag{2·2}$$

since we assume the fluid to be incompressible.

The important difference between equation (2·1) and the equation one normally has to deal with in the absence of rotation is the Coriolis term, $2\rho\boldsymbol{\Omega}\times\mathbf{u}$, which represents a force acting at right angles to $\mathbf{u}$ and which therefore does no work. However, when the Coriolis force is large in comparison with inertial ($\rho(\mathbf{u}.\nabla)\mathbf{u}$) and viscous ($\rho\nu\nabla^2\mathbf{u}$) forces the dynamical consequences are quite novel. It is instructive to discuss some of these consequences.

(*a*) *Slow, steady motions in an inviscid fluid*

By restricting ourselves to the study of slow, steady motion in a fluid of zero viscosity, we can ignore the first two terms on the left-hand side and the last term on the right-hand side of equation (2·1), which then becomes

$$2\rho\boldsymbol{\Omega}\times\mathbf{u}=-\nabla p+\rho\nabla\Phi. \tag{2·3}$$

It is convenient to introduce the hydrostatic pressure and density, p_0 and ρ_0 respectively, related by

$$\nabla p_0 = \rho_0 \nabla \Phi, \tag{2·4}$$

obtained by setting $\mathbf{u} = 0$ in equation (2·3). If $p = p_0 + p_1$ and $\rho = \rho_0 + \rho_1$ and it is assumed that $p_1 \ll p_0$ and $\rho_1 \ll \rho_0$ (a reasonable assumption here and in many other cases of practical interest, including the atmosphere), then to first order of small quantities, equations (2·3) and (2·4) lead to

$$2\rho_0 \boldsymbol{\Omega} \times \mathbf{u} = -\nabla p_1 + \rho_1 \nabla \Phi. \tag{2·5}$$

This is the so-called 'geostrophic' equation stating that that part of the impressed force field over and above the hydrostatic force is dynamically balanced against Coriolis forces. It is interesting to note, for example, that on horizontal surfaces (Φ constant) the flow is at right-angles to the horizontal pressure gradient. It is with the aid of Buys-Ballot's law—that if one faces the wind in the northern hemisphere the low pressure is on the right—that every schoolboy remembers the relationship between the directions of the vectors $\mathbf{u}$ and ∇p_1 in the last equation.

Let us eliminate p from equation (2·5) by operating with *curl*; thus, and with the aid of equation (2·2), we deduce that

$$2\rho_0 (\boldsymbol{\Omega} . \nabla)\mathbf{u} = \nabla \Phi \times \nabla \rho_1. \tag{2·6}$$

(*b*) *Homogeneous fluid: the Proudman–Taylor theorem*

Some time ago, Proudman and Taylor (Taylor 1921) deduced a theorem which states that slow, steady relative motions in an inviscid homogeneous fluid which otherwise rotates uniformly will be confined to planes perpendicular to the axis of rotation. Taylor (1921) subsequently verified the theorem by an elegant experiment.

This theorem follows from equation (2·6), which reduces to

$$2\rho_0 (\boldsymbol{\Omega} . \nabla)\mathbf{u} = 0 \tag{2·7}$$

when the fluid is homogeneous, because then $\nabla \rho_1 = 0$. If the z axis of a Cartesian co-ordinate system is taken to be parallel to $\boldsymbol{\Omega}$, equation (2·7) may be written

$$2\rho_0 \Omega (\partial \mathbf{u}/\partial z) = 0. \tag{2·8}$$

It is convenient to introduce the vector $\mathbf{u}_H$, defined as the component of $\mathbf{u}$ perpendicular to $\boldsymbol{\Omega}$, and u_z, the component of $\mathbf{u}$ parallel to $\boldsymbol{\Omega}$. Since ρ_0 and Ω do not vanish, by the last equation,

$$\frac{\partial \mathbf{u}_H}{\partial z} = 0; \quad \frac{\partial u_z}{\partial z} = 0. \tag{2·9 a, b}$$

Equation (2·9 b) states that u_z is independent of z, and therefore if u_z vanishes anywhere (as it would on a rigid surface normal to $\boldsymbol{\Omega}$) it vanishes everywhere. Proudman and Taylor gave a more rigorous proof of the so-called 'two-dimensional' theorem.

Equation (2·9 a) states that $\mathbf{u}_H$ is independent of z.

(*c*) *The 'thermal wind' equation*

Let us consider next an inhomogeneous fluid ($\nabla \rho_1 \neq 0$) which rotates about a vertical axis and for which gravity, acceleration $\mathbf{g} = (0, 0, -g)$, is so large that centrifugal effects may be

ignored. This is the case of most interest in connexion with the experiments described below. Equation (2·6) may now be written

$$2\rho_0(\boldsymbol{\Omega}\,.\,\nabla)\mathbf{u} = \mathbf{g}\times\nabla\rho_1, \tag{2·10}$$

which may be expanded to give two component equations,

$$2\rho_0\boldsymbol{\Omega}\times\partial\mathbf{u}_H/\partial z = g\nabla_H\rho_1 \tag{2·11}$$

and

$$\partial u_z/\partial z = 0. \tag{2·12}$$

In the last two equations, the positive z direction is the upward vertical and the symbol ∇_H is used to denote the vector operator $(\mathbf{i}\partial/\partial x+\mathbf{j}\partial/\partial y)$.

Equation (2·12) implies that even in an inhomogenous fluid, slow steady flow will be confined to planes perpendicular to the axis of rotation. It may be shown that in the more general case when the directions of $\boldsymbol{\Omega}$ and $\nabla\Phi$ are not parallel, equation (2·12) is still valid if the z axis is taken to be parallel to $\nabla\Phi$ (see Hide 1956). This result is not difficult to understand physically, if we remember that while the equation (2·3) contains no dynamical term representing a force which does any work, and no dissipative term, vertical motion in an inhomogeneous fluid always changes the potential energy of the system.

The existence of a non-uniform density field does, however, influence the horizontal motion. According to equation (2·11), there is a vertical shear of horizontal motion; this is the so-called 'thermal wind equation' which is familiar to meteorologists (Brunt 1939).

(*d*) *Dimensionless parameters*

Let U be a typical flow velocity and L a length characteristic of the scale of the system. The ratio of the magnitude of the inertial force, $\rho(\mathbf{u}\,.\,\nabla)\,\mathbf{u}$, to that of the viscous force, $\rho\nu\nabla^2\mathbf{u}$, in equation (2·1) is roughly

$$UL/\nu \equiv Re. \tag{2·13}$$

This is the Reynolds number, a dimensionless parameter known to characterize flow along a straight pipe, and to be important in many other hydrodynamical systems.

In a rotating system the Rossby number,

$$Ro \equiv U/L\Omega, \tag{2·14}$$

is an important parameter. Ro is a measure of the ratio of the inertial force to the Coriolis force. A further parameter, the significance of which has emerged in a number of investigations of rotating fluids, (see, for example, Chandrasekhar, 1953) is the Taylor number,

$$Ta \equiv \Omega^2L^4/\nu^2, \tag{2·15}$$

which is the square of the ratio of the magnitude of the Coriolis force to that of the viscous force. The Proudman–Taylor theorem (§2(*b*)) holds strictly only when Ro and Ta^{-1} are vanishingly small.

In a system characterized by vertical shear of the horizontal motion (thermal wind, see §2(*c*)) in the presence of a stable density gradient the Richardson number,

$$Ri \equiv \frac{g}{\rho_0}\left|\frac{\partial\rho_1}{\partial z}\right| \Big/ \left|\frac{\partial\mathbf{u}_H}{\partial z}\right|^2, \tag{2·16}$$

determines the properties of the flow, especially its stability (Eady 1949). In § 2(*e*) it is shown that the Rossby and Richardson numbers appropriate to an inhomogeneous cylindrical vortex are related to one another.

In free convection where both momentum and heat transfer occur, the velocity and temperature fields are closely related. When the flow is laminar, a parameter expected on general grounds to determine this relation is the Prandtl number

$$Pr \equiv \nu/\kappa \tag{2·17}$$

where κ is the coefficient of thermal diffusivity.

(*e*) *Geostrophic motion of an inhomogeneous cylindrical vortex*

Figure 1 illustrates the essential features of the apparatus described in § 3. The water is contained between rigid concentric cylinders, radii a and b. The bottom surface is rigid and the top surface is free. Near the boundaries of the fluid, viscous forces are expected to be important. However, in a fluid of moderate viscosity (more accurately, a system for which Ta^{-1} is small) viscous forces will only be significant within thin boundary layers. Outside these boundary layers the inviscid equations are expected to apply and if the motion is slow (*Ro* small) the flow will be geostrophic and governed by equation (2·11) if g is larger than centripetal acceleration.

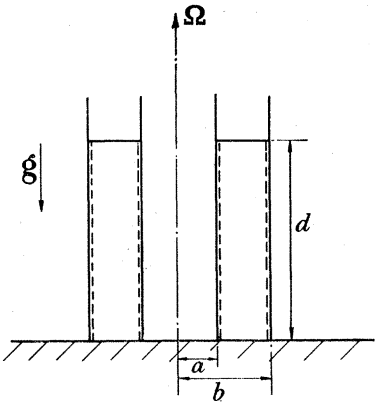

FIGURE 1

Let us assume that the density depends only on r, the distance from the axis, and z, the height above the bottom, and is independent of the azimuthal angular co-ordinate ϕ, that is to say, $\rho_1 = \rho_1(r, z)$. It will also be assumed that ρ_1 decreases upwards ($\partial\rho_1/\partial z < 0$), so that the vertical density gradient is stable. Equation (2·11) leads to a relation between ρ_1 and u_ϕ, the azimuthal or zonal velocity component, namely

$$2\rho_0\Omega\frac{\partial u_\phi}{\partial z} = -g\frac{\partial \rho_1}{\partial r}, \tag{2·18}$$

the sign being so chosen that u_ϕ is positive when the motion is cyclonic (i.e., from west to east).

Let $2\omega'$ be the mean relative vertical vorticity of the flow, related to the space average value of u_ϕ (denoted by $\overline{u_\phi}$) by the equation

$$\overline{u_\phi} = \omega' f_1(a, b), \tag{2·19}$$

where f_1 is a length of order $\frac{1}{2}(b+a)$.

Now introduce a quantity $\Delta_H \rho_1$, defined by the equation

$$\Delta_H \rho_1 = h_1(a, b)\, \overline{\partial \rho_1 / \partial r}, \tag{2·20}$$

where h_1 is a length. If $h_1 \sim (b-a)$, $\Delta_H \rho_1$ is the mean horizontal density contrast between the radial extremities of the fluid.

On averaging equation (2·18) over the whole fluid, and using equations (2·19) and (2·20) we find that

$$\frac{\omega'}{\Omega} = -\frac{g\, d \Delta_H \rho_1}{4 h_1 f_1 \Omega^2 \rho_0}. \tag{2·21}$$

Since ω'/Ω is the mean relative vorticity measured in terms of the vorticity of the basic rotation, this quantity estimates the relative dynamical importance of the inertial terms and the Coriolis terms in equation (2·1). Thus, it may be identified with the Rossby number appropriate to the problem in hand, namely

$$Ro \equiv \frac{\omega'}{\Omega} = -\frac{g\, d \Delta_H \rho_1}{4 h_1 f_1 \Omega^2 \rho_0}. \tag{2·22}$$

In order to construct a Richardson number we must find a measure of the stable vertical density gradient. Define the mean vertical density contrast, $\Delta_z \rho_1$, by the equation

$$\overline{\partial \rho_1 / \partial z} = -\Delta_z \rho_1 / d. \tag{2·23}$$

Now substitute u_ϕ for u_H in equation (2·16) and make use of equations (2·18), (2·19), (2·20) and (2·22), whence

$$Ri = \frac{4 \rho_0 h_1^2 \Delta_z \rho_1}{g d (\Delta_H \rho_1)^2}. \tag{2·24}$$

Finally, combine equations (2·22) and (2·24) and obtain a relation between Ri and Ro, namely

$$Ro\, Ri = \left(\frac{\Delta_z \rho_1}{\Delta_H \rho_1}\right)\left(\frac{h_1(a, b)}{f_1(a, b)}\right). \tag{2·25}$$

This relation does not tell us how intimately Ro and Ri are linked, since in general one would expect the density field outside boundary layers to depend on the impressed density field in a complicated way, perhaps involving Ro and Ri.

In the experiments described below, the two cylinders were held at different temperatures T_b and T_a, and the impressed vertical temperature gradient was zero (ignoring slight effects due to evaporation). We shall denote the corresponding impressed horizontal density contrast by $\Delta \rho_1$ where

$$\Delta \rho_1 \equiv \rho(T_b) - \rho(T_a). \tag{2·26}$$

The investigation of the temperature distribution described below in § 5 (g) revealed that the flow itself sets up a considerable stable vertical temperature gradient, and that outside the boundary layers the horizontal temperature fluctuations are a good deal less than $T_b - T_a$. This implies the existence of steep temperature gradients near the bounding cylinders.

As we shall see when the results of the investigation of the temperature field are discussed, the ratio $(\Delta_z \rho_1 / \Delta_H \rho_1)$ is apparently not very sensitive to the value of Ro over the limited range of experiments so far conducted. On general grounds one would expect this ratio to depend on Pr (see equation (2·17)), but because the range of Pr covered by the experiments was small, no direct evidence for this expectation was found. In the future, the possibility of such a dependence should be investigated by studying fluids other than water.

3. Apparatus and techniques

The peroration to James Thomson's Bakerian lecture on 'the grand currents of the atmospheric circulation', to the Royal Society in 1892 is particularly apposite here, because, although unknown to the present writer when his experiments were begun, Thomson's remarks bear on almost every aspect of the investigation.

> The apparatus would consist mainly of a horizontal circular tray kept revolving round a vertical axis through its centre. The tray would be filled to some suitable depth with water. Heat would be applied round its circumference at bottom, and cold would be applied, or cooling would be allowed to proceed at or near the surface. Under these circumstances I would expect that motions would institute themselves which would be closely allied to those of the great general currents supposed under the theory (that Thomson proposed in his lecture) to exist in either hemisphere of the earth's atmosphere. The motions of the water, I would propose should be rendered perceptible to the eye by dropping in small particles of aniline dye, and perhaps by other contrivances. Great variations would be available in respect to the velocity of rotation given to the tray and in respect to the depth of water used, and the intensity of heating and cooling influences applied. By various trials with variations in these respects I think it is likely that the phenomena expected could be made manifest.

Thomson died shortly after delivering his lecture and his suggestion was overlooked.

(*a*) *Basic requirements*

A cylindrical system was chosen for simplicity of shape and ease of construction. With water ($\nu \simeq 10^{-2}\,\mathrm{cm^2/s}$) and angular speeds of the order of 6 rad/s (see § 1 (*a*)), Ta is 10^5 when L is about 1 cm (see equation (2·15)). Hence, primary viscous effects were not expected under conditions readily attainable in the laboratory. Again for simplicity, it was decided to use an entirely radial impressed temperature field, although slight 'end effects' did arise (see § 5 (*g*)).

(*b*) *The convection chamber*

In figure 2 the essential parts of the apparatus are shown diagrammatically and a general view is given in figure 3, plate 5. Three cylinders, A, B, and C, each 13 cm long, were mounted concentrically on a Bakelite base plate L. The smallest cylinder A was a length of brass tubing $\frac{1}{16}$ in. thick, one end of which was sealed with a brass disk and located by a screw at the centre of L. This cylinder was filled with water maintained at T_i °C. Several cylinders A were employed during the course of the investigation, so that a could be varied from 1·06 to 3·54 cm.

The two larger cylinders, B and C, were about $\frac{1}{8}$ in. thick. They were located in slots cut in L and held firmly in position by means of a watertight gasket arrangement consisting of rubber rings G and brass rings R. The main convection chamber was between A and B, which was filled with water to a depth d, always less than 11 cm. The temperature of B was controlled by filling the space between B and C with water maintained at T_o °C. The inside diameter, $2b$, of B was always 9·7 cm.

In all experiments C was a length of ordinary Pyrex glass tubing. B was of the same material when visual observations through the side were made, although when certain other observations were made, a brass cylinder B was used.

The warm bath was heated electrically by an element of ordinary 18-gauge resistance wire (resistance about 0·2 Ω), the voltage supply to which could be varied from 0 to 15 V. The

maximum available electrical input power was about 1 kW, but in most of the experiments, only a small fraction of this was used.

Tap water circulated through the cool bath. It was introduced from a constant head through a copper tube and removed via a second such tube connected to a filter pump. The rate of flow, Q, was controlled by means of a throttle, and was usually about 10 ml/s. No flowmeter was incorporated but frequent checks on Q were made by measuring the time required to fill a known volume. Fluctuations of Q amounted to no more than a few parts per cent over several hours.

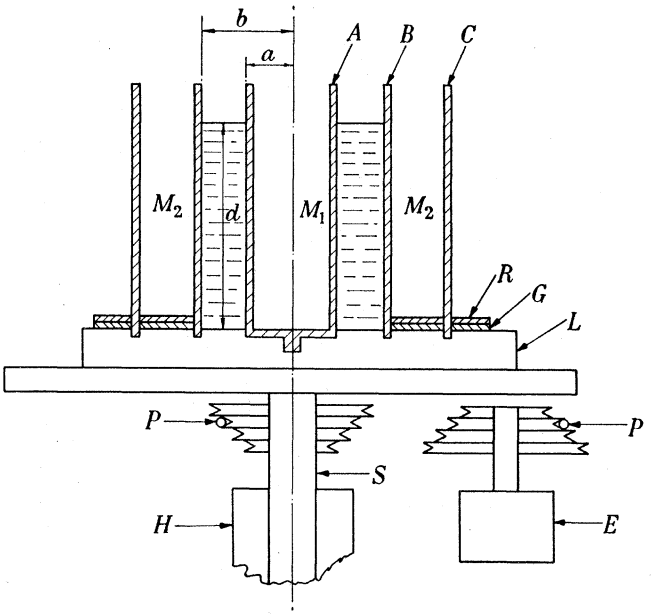

FIGURE 2. Section through apparatus illustrating the general features of its construction.

The temperature rise experienced by the cooling water was measured with a copper-constantan thermocouple. The signal from this thermocouple was led to an ordinary lamp-and-scale galvanometer whose reading gave an indication of how close the system was to thermal equilibrium. These temperature measurements, when combined with the value of Q, led to rough determinations of heat flow.

A better check on thermal equilibrium came from a knowledge of T_o and T_i, which were measured with ordinary mercury-in-glass thermometers.

When cylinder B was glass the convection chamber was provided with a shallow false bottom of wood to avoid thermal end effects. This precaution was unnecessary when B was brass. The top surface of the water in the temperature baths was always above the level in the convection chamber.

The bakelite base plate was mounted on a horizonal turn-table. The turn-table was a 1 ft diameter steel disk. It carried a 1 in. diameter shaft S, 1 ft. long, which passed through two plane bearings in the shaft housing H and terminated in a simple thrust bearing.

A fractional horse-power Klaxon synchronous motor E (see figure 2) provided the power for rotating the turn-table at constant speed through a belt and pulley drive, P. With a gear-box and several sets of pulleys eight values of Ω ranging from 0·86 to 8·23 rad/s were obtained.

The whole apparatus was mounted on a massive cast-iron plate which was alined by means of levelling screws.

(*c*) *Visual indicators of flow*

Although use was made of dye crystals such as malachite green, crystal violet and fluorescein (Fultz 1949), and of inks having approximately the same density as water, to give visual indications of the flow, such observations, though valuable, could only be made for limited periods before the dye was uniformly diffused throughout the liquid. This limitation is not suffered by the technique of introducing small wax pellets of density close to unity, but further complications due to buoyancy effects arise in a convecting system where density fluctuations are necessarily present.

The flow indicator most extensively employed was clean aluminium powder, which will remain in suspension in water for several hours. When the concentration of the powder was sufficiently high to give a good indication of the top-surface flow pattern, it was impossible to see beyond the top surface. However, at somewhat lower concentrations observations of the flow pattern at depth could be made.

(*d*) *The rotoscope*

It is possible to produce a stationary image of a rotating system by viewing it through a rotating mirror. This method has two drawbacks, however, namely that the field of view is small and varies as the mirror rotates. To overcome these, Thoma (see Fischer 1931) introduced the rotoscope, which is a Dove reversing prism rotating about an axis parallel to its base.

The rotoscope used in this investigation was mounted about 1 m above the convection chamber, and was turned by a belt directly coupling it to the turn-table.

A selection from the many photographs of the top-surface flow pattern, obtained by pointing a camera through the rotoscope, is reproduced in this paper.

(*e*) *Technique for investigating the temperature field*

The temperature fluctuations to be measured were of the order of several degrees Centigrade. A thermometer rotating with the apparatus had to respond in about 0·2 s and to minimize disturbances of the flow, it was essential that the thermometer should be small. To meet these requirements three thermocouples were made out of 38-gauge constantan and 33-gauge copper wire. Each had one common junction which was maintained at temperature T_o by soldering to cylinder B (see figure 2). Because these thermocouples rotated with the apparatus it was necessary to provide rotating electrical contacts. Concentric circular troughs of mercury mounted above the apparatus served this purpose. Contact with the mercury was made via thick copper leads. The signals from the thermocouples were led to three Tinsley taut-suspension galvanometers, the deflexions of which were recorded with a camera.

The apparatus was calibrated by comparison with the readings of a fourth thermocouple recording the difference $(T_o - T_i)$, and mercury-in-glass thermometers reading T_o and T_i separately.

Figure 4, plate 5, is a photograph of the convection chamber with the thermocouples in position.

4. The initial observations

In § 2 some of the experimental results were anticipated in order to give a physical interpretation of the parameter Θ (see equation (1·1)). To facilitate the description of the initial observations we shall employ in this section a quantity related to Θ, namely

$$X \equiv -d\Delta\rho/\rho_0 \Omega^2 \text{ cm s}^2, \tag{4·1}$$

where

$$\Delta\rho \equiv \rho(T_o) - \rho(T_i). \tag{4·2}$$

We note here that the temperatures T_b and T_a of the cylindrical surfaces in contact with the water were effectively equal to T_o and T_i the temperatures of the two water-baths, respectively, when metal cylinders were employed. However, when cylinder B (see figure 2) was glass a small but significant temperature drop, $T_o - T_b$, existed across it. $T_o - T_b$ could be estimated roughly from the measured heat flow. We shall use a prime on $\Delta\rho$ and X to signify when the glass cylinder was used. X is proportional to Θ and contains all the relevant variables when b and a are fixed.

In figure 5, plate 6, a series of photographs of the top surface flow pattern is presented. It illustrates the effect of varying X' through changes in Ω and $\Delta\rho'$ keeping b, a and d constant at 4·85, 1·92 and 10 cm, respectively. In each case $\Delta\rho' < 0$, the outer cylinder being at the higher temperature. Aluminium powder was used to indicate the flow pattern (see § 3 (*c*)). (The specks seen in these photographs are agglomerations of aluminium particles which failed to enter into suspension.) The range of X' covered by these observations is from 62×10^{-3} to $1{\cdot}9 \times 10^{-3}$ cm s^2, and to give an idea of the temperature differences involved, we note that $\rho(4\ ^\circ\text{C}) - \rho(100\ ^\circ\text{C}) = 42 \times 10^{-3}$ g/cm^3.

Let us start with figure 5*a*, which corresponds to a case of low rotation, for which $X' = 62 \times 10^{-3}$ cm s^2. The spiral pattern is clearly seen, the flow in which was eastward, (clockwise in the picture). For reasons that will be given below (§ 4 (*b*)) this régime of flow characterized by a top surface spiral will be termed 'supercritical'.

The effect of decreasing X' (in this case by decreasing $\Delta\rho'$ only) to 17×10^{-3} cm s^2 may be seen by passing to figure 5*b*. We now see a type of flow which is apparently fundamentally different from that of figure 5*a*, the pattern being a wave for which the wave number m is 2. On decreasing X' still further (see figures 5*c*, *d*, *e*), the wave pattern persists, with a tendency for m to increase. Flows characterized by a top surface wave pattern will be termed 'subcritical'.

(*a*) *General description of subcritical flow*

By far the most conspicuous feature is the thin 'jet' stream in which the relative flow velocity is much higher than that of the surrounding fluid. The sense of the motion in the 'jet' is westerly (eastward, or cyclonic) as can be judged from figure 6, plate 7. These two photographs were taken a short time after introducing a few crystals of malachite green dye at the top surface. Figure 6*a* shows the trail of ink left by the crystals when the stop-watch in the picture read 2 s, and figure 6*b* was taken 12 s later. (Since no precaution was ever taken to expose the film with the turn-table in any particular position, in these pictures, apparatus fixed in the laboratory, e.g. the stop-watch, which appeared to rotate when viewed through the rotoscope, will not always be in the same position relative to a point rotating with the convection chamber.)

The dye fell mainly outside the 'jet' stream in a position slightly anticlockwise of the arrowhead (to indicate the sense of the rotation) painted on cylinder B (at '9 o'clock' in figure 6). There is a dark streak indicating eastward motion from near the arrowhead, and in figure 6*b* we see that the streak has completed more than one full excursion around the annulus. By noting the movement of the original patch of crystals, we see that in contrast to the flow in the 'jet' stream, the motion in the region outside the 'jet' is quite slow.

Another important feature is apparent from these pictures, namely, that the wave pattern as a whole drifts eastward relative to the rotating apparatus. This can be ascertained by noting in these two pictures the positions of the wave crest adjacent to the patch of crystals relative to that of the arrowhead. The speed of the drift is an order of magnitude slower than that of the motion in the 'jet' stream.

Further examples to illustrate the drift motion are given in figures 7 and 8, plate 7, where the orientation of the wave pattern can be obtained by noting the position of the piece of wire attached to the rotating apparatus (at '12 o'clock' in figure 8*a*. In figure 7, for which $m = 4$ and $X' = 2{\cdot}8 \times 10^{-3}\,\mathrm{cm\,s^2}$ (cf. figure 5*d*) the eastward drift is clearly seen. In figure 8 for which $m = 3$ and $X' = -7{\cdot}4 \times 10^{-3}\,\mathrm{cm\,s^2}$ (cf. figure 5*c*), (the negative sign indicating that $T_i > T_0$), the drift is westward. The sense of the motion in the top surface 'jet' stream was also westward in this case, but this cannot be judged from figure 8.

More careful observations than those described above showed that when the wave pattern was not undergoing any general change of shape, the drift motion was quite uniform. The best evidence for this uniform drift came from the investigation of the temperature field described in § 5 (*g*).

We have seen that within a certain range of X', m increases as X' decreases. However, there is a certain value of X' at which any further decrease in X' no longer leads to a change in m. Thus, changing X' from $1{\cdot}9 \times 10^{-3}\,\mathrm{cm\,s^2}$ (see figure 5*e*) to $0{\cdot}68 \times 10^{-3}\,\mathrm{cm\,s^2}$ (see figure 9, plate 8) leads to no increase in m, which is 5 in both cases. However, in contrast to the flow in figure 5*e*, that in figure 9 was very unstable. The flow pattern changed rapidly and quite irregularly. The drift was spasmodic, but definitely eastward and there was a good deal of mixing between the highly distorted 'jet' stream and the other regions. Incipient waves often developed near the inner cylinder. However, in spite of these irregularities, vestiges of a wave pattern for which $m = 5$ are present. Never was $m = 5$ exceeded when a, the radius of the centre cylinder, was 1·92 cm, but, as we shall see in § 5 (*b*), values of m in excess of 5 may be obtained by decreasing $(b-a)$, the width of the annulus.

In the particular example chosen for figure 9 the low value of X' was attained by using the highest value of Ω available. Because unstable patterns were first observed at high rotation speeds it was suspected initially that the instability was a result of inevitable slight misalinements of the apparatus. However, careful readjustment of the apparatus in no way reduced the instability of the flow, but with the more accurately alined apparatus a type of flow was discovered which represents a transition between the highly unstable flow, arising at very low values of X, and the well-organized wave flow at higher values of X. Figure 10, plate 8, consists of two pictures of the top surface flow at $X' = 1{\cdot}3 \times 10^{-3}\,\mathrm{cm\,s^2}$ (cf. figures 9, 5*e*) taken at different instants. It is sufficient to note that these flow patterns differ from one another; they represent two phases of a regular fluctuation, or 'vacillation' as we shall term this phenomenon. 'Vacillation' is described in further detail in § 5 (*b*).

Let us now examine the differences between flow patterns with the same m value, obtained by keeping a, b and d constant and varying Ω and $\Delta\rho'$ in such a way as to keep X' roughly constant. Figures 5*d*, 7, 11, 12, 13 (plates 6 to 8) are all pictures of $m = 4$ patterns (although the flow of figure 13 was undergoing some change at the time the photograph was taken). The 'jet' stream width appears to decrease as Ω increases over the range to which this series of pictures corresponds, namely, from 6·28 rad/s (figures 11 and 12) to 2·07 rad/s (figure 13). Especially noticeable in figure 12 are the secondary eddies near the edge of the 'jet' stream. The high rate of shear which is probably responsible for these eddies is due to a combination of relatively high flow velocity required to give $m = 4$ at a relatively high value of Ω, and the small 'jet' stream width.

To illustrate the effect of varying d, figures 14 and 15, plate 8, are included here. Figure 14 ($X' = 2{\cdot}2 \times 10^{-3}\,\mathrm{cm\,s^2}$, $m = 5$) and figure 15 ($X' = 3{\cdot}4 \times 10^{-3}\,\mathrm{cm\,s^2}$, $m = 4$) for which $d = 3{\cdot}8$ cm should be compared with figure 5*e* ($X' = 1{\cdot}9 \times 10^{-3}\,\mathrm{cm\,s^2}$, $m = 5$) and figure 5*d* ($X' = 3{\cdot}4 \times 10^{-3}\,\mathrm{cm\,s^2}$, $m = 4$) for which $d = 10$ cm. (The tendency is marked in figures 14 and 15 for those particles of aluminium which had not been adequately degreased to remain on the top surface.) The asymmetry of the pattern shown in figure 15 should also be noted.

When d was less than about 3·5 cm, the flow pattern was very irregular. It is likely that this irregularity was due to the temperature gradient caused by evaporation from the top surface, a feature which emerged later in the investigation from a study of the temperature field (see § 5 (*g*)).

Having briefly described the phenomena arising with one particular geometry, namely, $a = 1{\cdot}92$ cm, $b = 4{\cdot}85$ cm, let us examine the effect of varying a. Figures 16 to 19, plate 9, illustrate typical flow patterns obtained when $a = 2{\cdot}85$ cm. It will be noted immediately that one result of decreasing the width of the annulus is to increase the maximum attainable value of m. Figures 17 and 18 are examples of the very regular and symmetrical patterns often, but not always, observed.

Although $m = 8$ was never exceeded when $a = 2{\cdot}85$ cm, by increasing a to 3·54 cm it was possible to produce patterns for which m was as high as 14. Figures 20 and 21, plate 9, are examples of $m = 9$ and $m = 13$ flow patterns at this value of a.

Transition from one value of the wave number to another

In the foregoing discussion we have seen that m is roughly determined by the value of X', and down to a certain value of X', m increases as X' decreases. Since X' can vary continuously, whereas m must be an integer, one expects that if (say) the conditions of figure 5*c* ($X' = 5{\cdot}8 \times 10^{-3}\,\mathrm{cm\,s^2}$) were slowly changed to those of figure 5*d* ($X' = 3{\cdot}4 \times 10^{-3}$) by allowing $-\Delta\rho'$ to fall, m should change from 3 to 4 at some stage of the experiment. Such transitions were observed, but the values of X' at which they occurred were not at all reproducible. When specific experiments are described in § 5, this point will be discussed quantitatively. It is intended here to describe briefly the manner in which such transitions occurred.

In some cases, the first phase was characterized by a rearrangement of the three waves, reducing their angular spacing from 120 to 90°, and thus leaving a gap into which a fourth wave could grow. The new wave would then develop from an incipient growth on the 'jet' stream. This incipient wave frequently arose quite close to the inner cylinder, when $T_o > T_i$. Figure 13 shows a typical half-developed wave.

Although a general rearrangement of the existing waves followed by the growth of an additional wave was the most frequently observed manner by which the wave-number increased by unity, on a few occasions another process occurred. In this, one of the existing waves split into two waves of full amplitude, which then readjusted their angular disposition.

The transition $m = 4$ to $m = 3$ occurred as follows: First the $m = 4$ pattern degenerated into a blunt square which in turn gave way to a rough triangle, in which the 'jet' stream was badly developed. The triangle then underwent changes which brought about an intensification of the 'jet' stream and the development of 3 waves. Typical stages of such a transition are depicted in figure 22, plate 10.

No attempt to study these readjustments of the flow in a systematic way has yet been made, and such an investigation should be made in the future. These transitional processes have been described here because occasionally they interfered with the measurements described in later parts of this paper. If, for example, an $m = 4$ flow which had been under observation for some time suddenly underwent a transition to $m = 5$ or $m = 3$, it was usually possible to recover $m = 4$ by repeating the process of stirring the water, thus destroying the wave flow, and allowing the wave flow to reform, a sufficient number of times for success to be achieved (see § 5 (*e*)).

The development of the flow after the water had been thoroughly stirred occurred as follows: It would take about a minute or so for viscosity to reduce the water to a state of solid body rotation, which was followed immediately by the development of zonal top-surface relative flow. Figure 23, plate 10, illustrates the development after the zonal flow stage. In figure 23 *a*, two incipient waves may be seen, one half-grown at '12 o'clock' and the other still quite small at '3 o'clock' and touching the centre cylinder. Nine seconds later (figure 23 *b*) a third wave had started to grow at '7 o'clock' and fifteen seconds later still the three waves (one of which unfortunately is obscured by the cooling water tubes) filled the annulus. No angular drift of this pattern occurred until the last stage had been completed. Occasionally the number of incipient waves exceeded the number which eventually became fully grown.

Flow at depth

When a very low concentration of aluminium powder was used for rendering the flow visible (see § 3 (*c*)), it was possible to see beyond the top surface and into the fluid. The impression gained was that the wave pattern extends throughout almost the entire depth of fluid, and this impression was strengthened by the existence of almost vertical dark streaks in the positions of the top-surface wave crests, which extended to within a few millimeters of the bottom. Attempts to record these observations photographically failed, and the efforts to photograph ink trails at depth were not too successful, although direct visual observations of the latter were instructive.

The shape of the trail behind a slowly falling crystal of malachite green indicated that the horizontal flow velocity varies with depth, the tendency being a decrease proceeding downward. A slight, though distinct tendency for radial motion to be associated with a slight vertical motion was observed; the vertical motion appeared to be upward for flow from the hot cylinder to the cold cylinder and downward for the reverse flow.

The pattern near the bottom of the convection chamber was shown very strikingly on one occasion when observations using wax pellets (see § 3 (*c*)) were being made. Many of the

pellets sank very slowly to the bottom and on settling they marked out a distinct wave pattern. Perhaps the most convincing indications of the form of the flow pattern at depth are contained in the results of the investigation of the temperature distribution which will be described in a later section (§ 5 (*g*)).

(*b*) *General description of supercritical flow*

In the introduction to this section it was stated that supercritical flow arises at high values of X', corresponding to low rates of rotation and rapid rates of heating. Consider an experiment in which X' is varied gradually with time from 17×10^{-3} to 62×10^{-3} cm s^2 (see figures 5*b*, *a*) by increasing $T_o - T_i$ very slowly. According to figure 5, a transition from $m = 2$ to a spiral flow pattern should occur. In contrast to the transitions from one value of m to another within the subcritical régime, conditions at which the transition to supercritical flow occurred were fairly accurately reproducible (see § 5 (*c*)).

A typical stage of the transition is depicted in figure 24, plate 10, for which $X' = 19 \times 10^{-3}$ cm s^2. Fluctuations between this pattern and that of figure 5*b* often occurred but a further slight increase of the heating rate sufficed to suppress such fluctuations, the top-surface flow pattern remaining spiral (see figure 5*a*). The value of m at which the transition to a spiral flow pattern occurs depends on the width of the annulus, $(b-a)$ (see § 5 (*c*)).

The flow in the top-surface spiral pattern (which is eastward and inward or westward and outward according as $T_o \gtrless T_i$) is inconsistent with ideas of continuity unless there is ascending flow near the hot cylinder and descending flow near the cool cylinder. Ink observations gave an indication of this vertical motion, and revealed the existence of a spiral flow near the bottom of the fluid. The obvious explanation of this flow is that it is similar to that in a Hadley cell, in which the basic circulation is a meridional vortex and the spiral is the result of the action of Coriolis forces on the radial flow in this vortex. However, the meridional circulation appeared to be restricted to a thin layer, about 2 mm wide, near the extremities of the liquid, and the main body of liquid appeared to be in zonal motion in the same sense as that of the flow in the top surface spiral.

Since the speed of vertical motion must be of the same order of magnitude as that of the radial flow, the 'tightness' of the spiral should increase with Ω. This feature is apparent in figures 5*a* and 25.

A further observation was that the direction of the flow near the walls departs systematically from the vertical, the streamlines being slightly 'bowed', the streamlines of sinking motion being convex towards the west and rising flow streamlines convex towards the east. Figure 26, plate 11, is a photograph of ink trails which show some of these features. In the case depicted here the outer cylinder was cooler than the inner, so that the rising motion occurred near the inner cylinder. The thin boundary layer in which the upward flow occurred is seen edge on (on the immediate left of the inner cylinder). The curvature of the streamlines cannot be judged from this streak, but slightly to the left is to be seen a curved streak near the outer cylinder. The sense of the convexity can be judged knowing that the rotation was from left to right, and that the streak in question was, at the instant of observation, behind the plane normal to the line of sight containing the axis of the cylinders. Another streamline, to be seen in the foreground and slightly to the right of the centre cylinder, is also curved in the same sense.

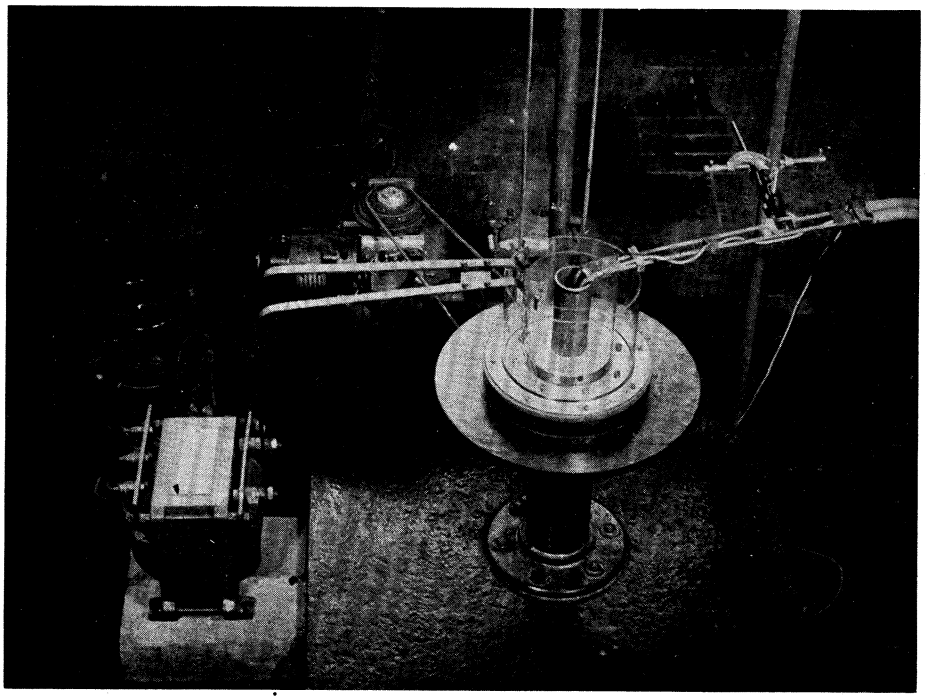

FIGURE 3. General view of the apparatus. Cooling water tubes are on the right. The transformer and Variac used to supply and vary the power to the heating element are on the left. The turn-table is mounted on a cast-iron plate. It was driven by the electric motor through a belt and pulley arrangement. The vertical post near the middle of the picture carries the rotoscope at the top (not seen in picture). Part of the belt drive to the rotoscope running parallel to the vertical post may be seen. To judge the scale, note that the transformer stands on two standard building bricks.

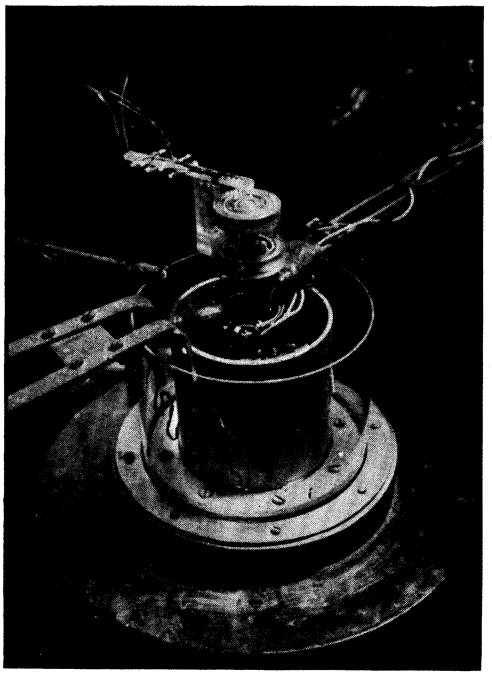

FIGURE 4. Convection chamber with thermocouples in position. The rotating mercury troughs are above the convection chamber. The Perspex bar carrying the non-rotating copper leads is rigidly attached to a ball-race arrangement directly underneath the mercury troughs. With this set-up, the troughs rotated accurately relative to the copper leads despite inevitable misalinement of the support carrying the troughs on the main turn-table.

(*Facing p.* 456)

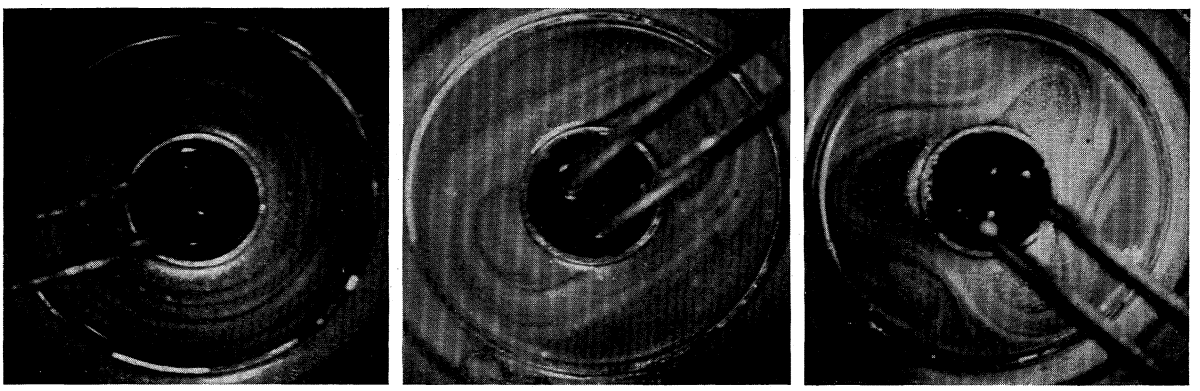

	(*a*)	(*b*)	(*c*)
Ω(rad/s)	1·56	1·56	3·48
$10^3\Delta\rho'/\rho_0$	−15·0	−4·2	−7·0
$X'(10^{-3}$ cm s$^2)$	62	17	5·8

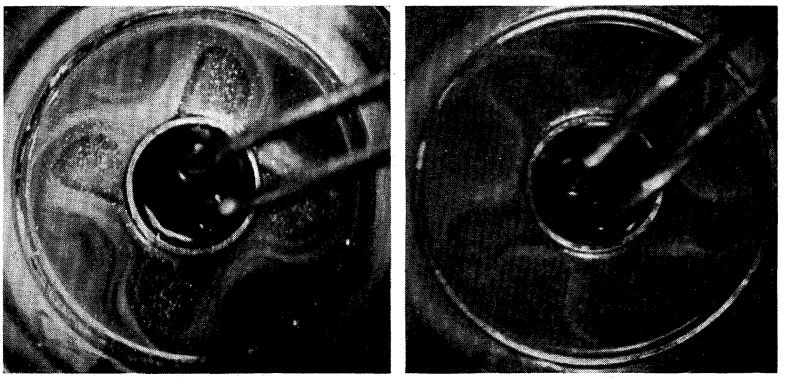

	(*d*)	(*e*)
Ω (rad/s)	3·48	4·71
$10^3\Delta\rho'/\rho_0$	−4·1	−4·3
$X'(10^{-3}$ cm s$^2)$	3·4	1·9

FIGURE 5. Top-surface flow patterns at different values of X'. Aluminium powder was used as an indicator. In each case, $a = 1{\cdot}92$ cm, $b = 4{\cdot}85$ cm, $d = 10{\cdot}0$ cm. The sense of rotation is clockwise. (*a*) corresponds to low rotation, in which case the top-surface flow pattern is a spiral. The four remaining pictures are typical examples of the wave-flow régime, with wave number m going from 2 to 5.

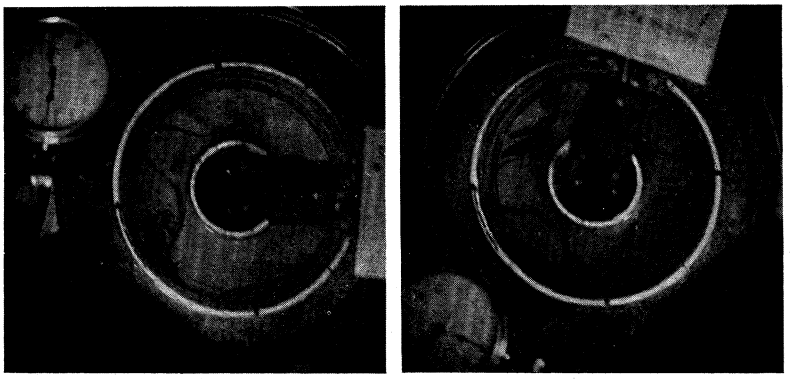

(*a*) (*b*)

FIGURE 6. Illustrating the angular drift motion of the wave-flow pattern. Experimental details: $a = 1{\cdot}92$ cm, $b = 4{\cdot}85$ cm, $d = 6{\cdot}7$ cm, $\Omega = 3{\cdot}48$ rad/s, $\Delta\rho'/\rho_0 = -9{\cdot}2 \times 10^{-3}$, $X' = 5{\cdot}1 \times 10^{-3}$ cm s^2, rotation clockwise. (*a*) was taken a few seconds after introducing a few crystals of malachite green dye at the top surface. (*b*) was taken 12 s later, and by comparing the dye streaks in the two pictures, the sense of motion in the 'jet' stream is seen to be eastward. Comparison of the positions of the whole pattern relative to the faint black arrowhead painted on the white rim of the middle cylinder, (at approximately '9 o'clock') shows that during the 12 s interval an eastward angular drift through 45° took place.

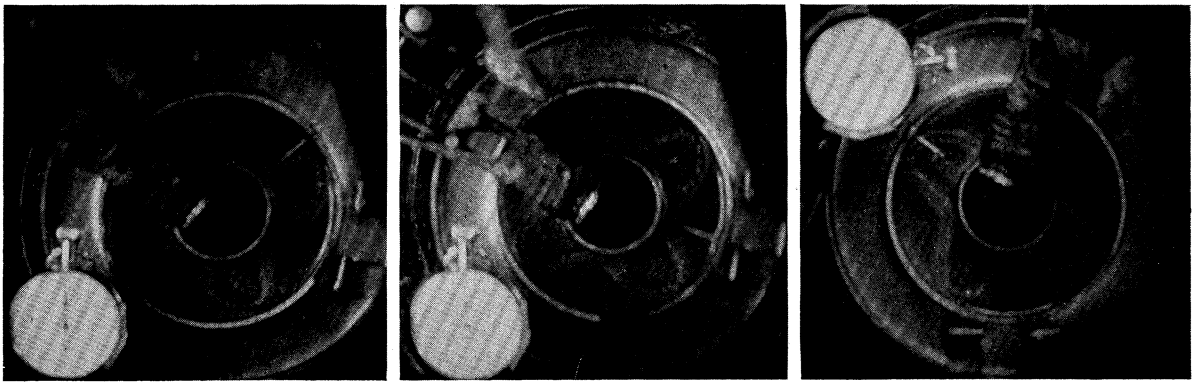

(*a*) $t = 0$ (*b*) $t = 10$ s (*c*) $t = 34$ s

FIGURE 7. Hot outer cylinder; angular drift eastward.

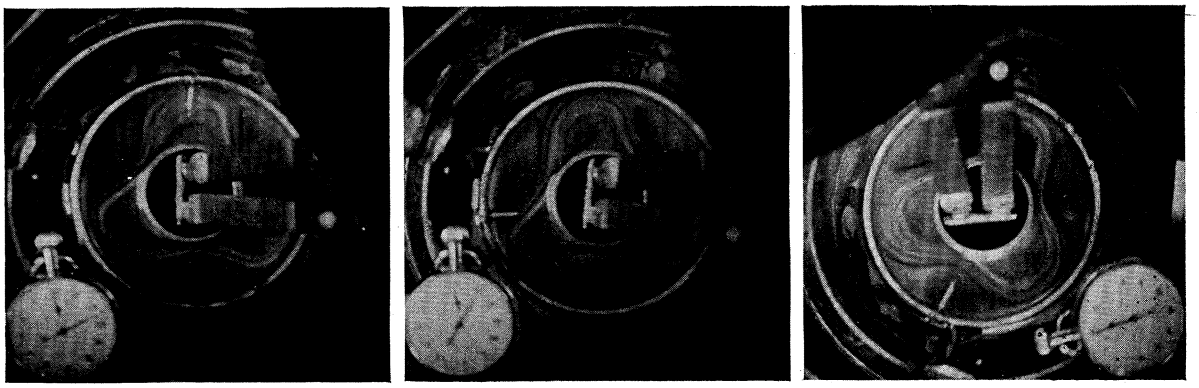

(*a*) $t = 48$ s (*b*) $t = 54$ s (*c*) $t = 61$ s

FIGURE 8. Hot inner cylinder; angular drift westward.

FIGURES 7 AND 8. Illustrating the dependence of the sense of the angular drift of the top-surface wave-flow pattern on the direction of the impressed temperature gradient. t is the stop-watch reading. The position of the pattern should be judged by noting the position of the wire attached to outer cylinder, at '12 o'clock' in figure 8(*a*). Experimental details:

	a (cm)	b (cm)	d (cm)	Ω (rad/s)	$\Delta\rho'/\rho_0$	X' (cm s^2)
figure 7	1·92	4·85	10·0	4·71	$-6{\cdot}2 \times 10^{-3}$	$+2{\cdot}8 \times 10^{-3}$
figure 8	1·92	4·85	10·0	3·48	$+8{\cdot}9 \times 10^{-3}$	$-7{\cdot}4 \times 10^{-3}$

Rotation clockwise; aluminium powder indicator.

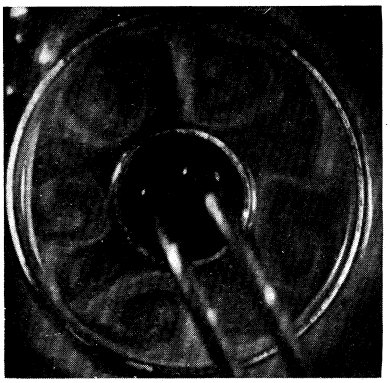

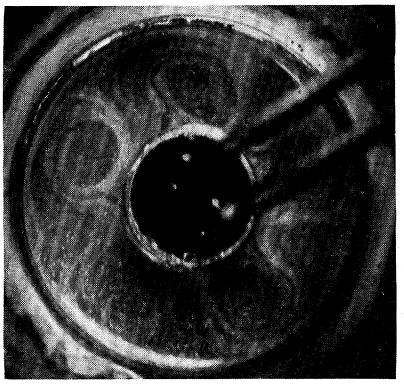

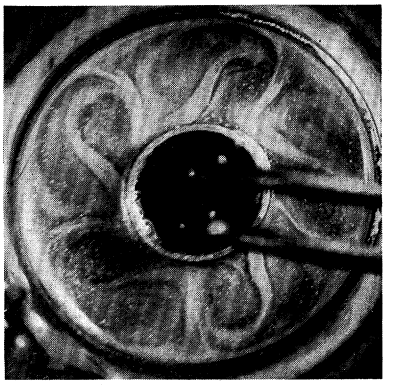

	FIGURE 9	FIGURE 10*a*	FIGURE 10*b*
Ω (rad/s)	8·23	8·23	
$10^3\Delta\rho'/\rho_0$	−4·5	−9·0	
$X'(10^{-3}$ cm s$^2)$	0·68	1·3	
d (cm)	10·0	10·0	

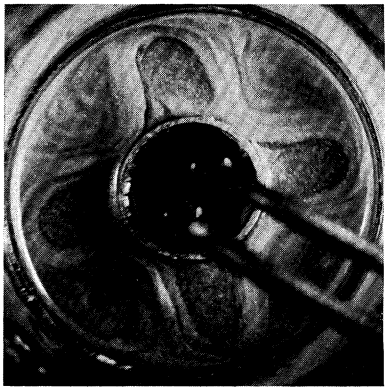

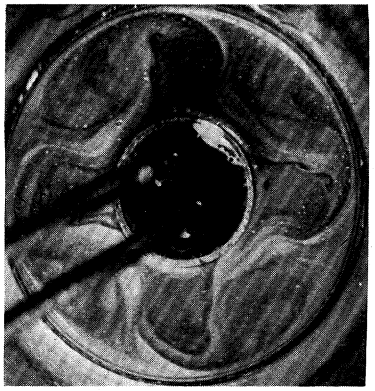

	FIGURE 11	FIGURE 12	FIGURE 13
Ω(rad/s)	6·28	6·28	2·07
$10^3\Delta\rho'/\rho_0$	−9·0	−10·4	−2·8
$X'(10^{-3}$ cm s$^2)$	2·3	2·6	6·5
d (cm)	10·0	10·0	10·0

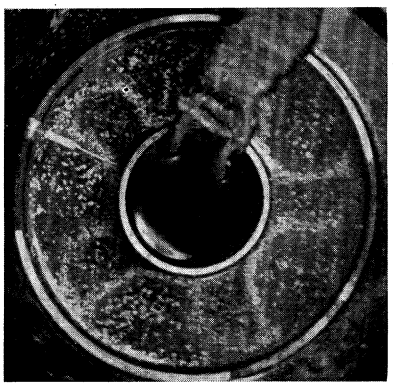

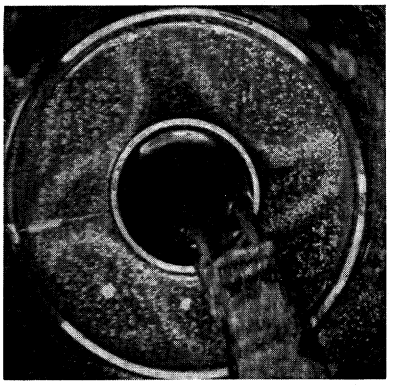

	FIGURE 14	FIGURE 15
Ω(rad/s)	3·48	3·48
$10^3\Delta\rho'/\rho_0$	−7·0	−11·0
$X'(10^{-3}$ cm s$^2)$	2·2	3·4
d (cm)	3·8	3·8

FIGURES 9 TO 15. Further examples of the top-surface flow patterns with the inner cylinder radius $a = 1{\cdot}92$ cm. Rotation clockwise; aluminium powder indicator.

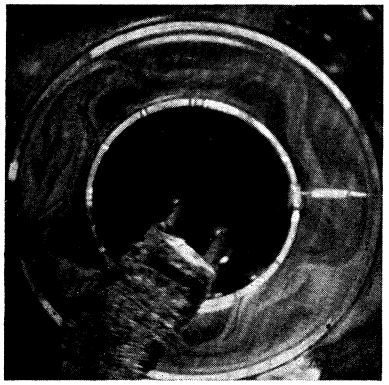

FIGURE 16

Ω (rad/s)	6·28
d (cm)	10·0
$10^3\Delta\rho'/\rho_0$	−13·0
$X'(10^{-3}$ cm s$^2)$	3·3

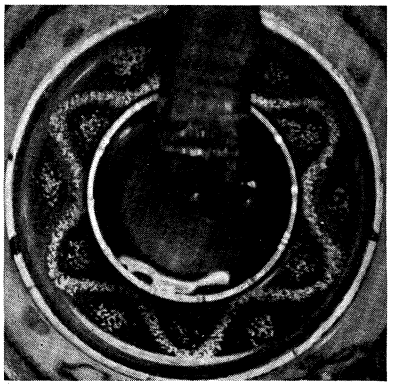

FIGURE 17

4·71
8·5
−5·6
2·1

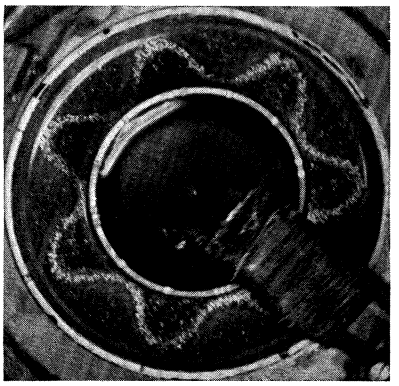

FIGURE 18

4·71
8·5
−4·7
1·8

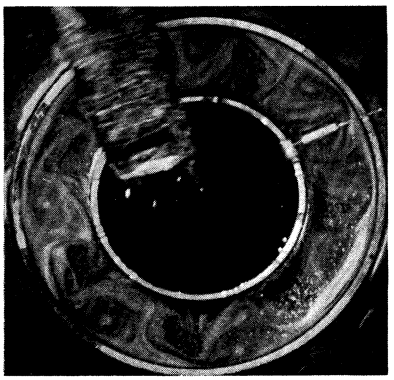

FIGURE 19

Ω (rad/s)	6·28
d (cm)	10·0
$10^3\Delta\rho'/\rho_0$	−4·0
$X'(10^{-3}$ cm s$^2)$	1·0

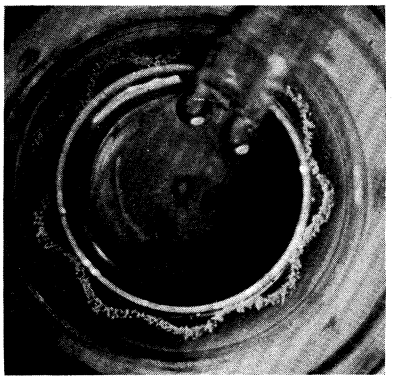

FIGURE 20

4·71
6·5
−1·7
0·5
$m = 9$

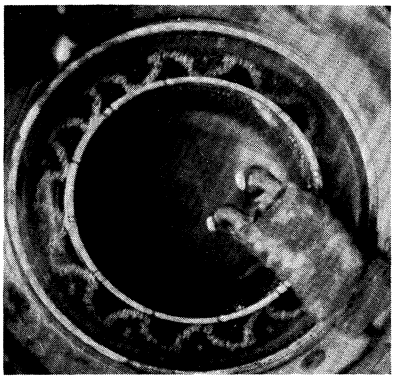

FIGURE 21

6·28
6·3
−1·4
0·23
$m = 13$

FIGURES 16 TO 19. Examples of top-surface flow patterns with the inner cylinder radius $a = 2{\cdot}85$ cm. In figures 17 and 18 agglomerations of aluminium particles which did not enter into suspension are clearly seen.

FIGURES 20 AND 21. Examples of top-surface flow patterns with the inner cylinder radius $a = 3{\cdot}54$ cm. Rotation clockwise; aluminium powder indicator.

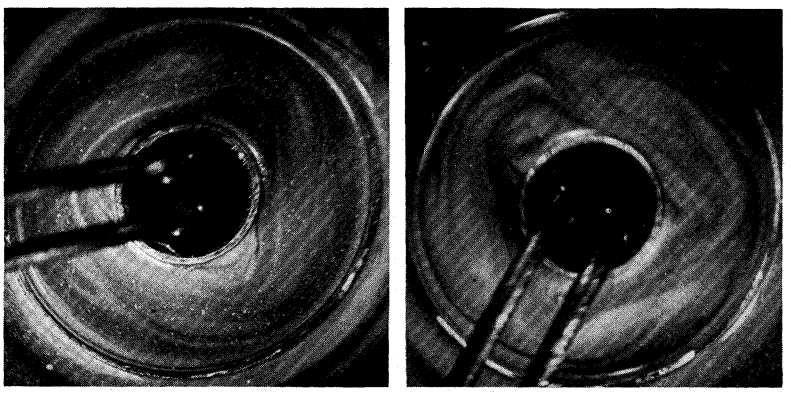

(*a*) (*b*)

FIGURE 22. Typical stages as wave flow changes its wave number from 4 to 3 (see § 4 (*a*)). Experimental details: $\Omega = 3{\cdot}48$ rad/s, $d = 10{\cdot}0$ cm, $a = 1{\cdot}92$ cm, $b = 4{\cdot}85$ cm, $\Delta\rho'/\rho_0 = -11{\cdot}5 \times 10^{-3}$, $X' = 9{\cdot}5 \times 10^{-3}$ cm s^2.

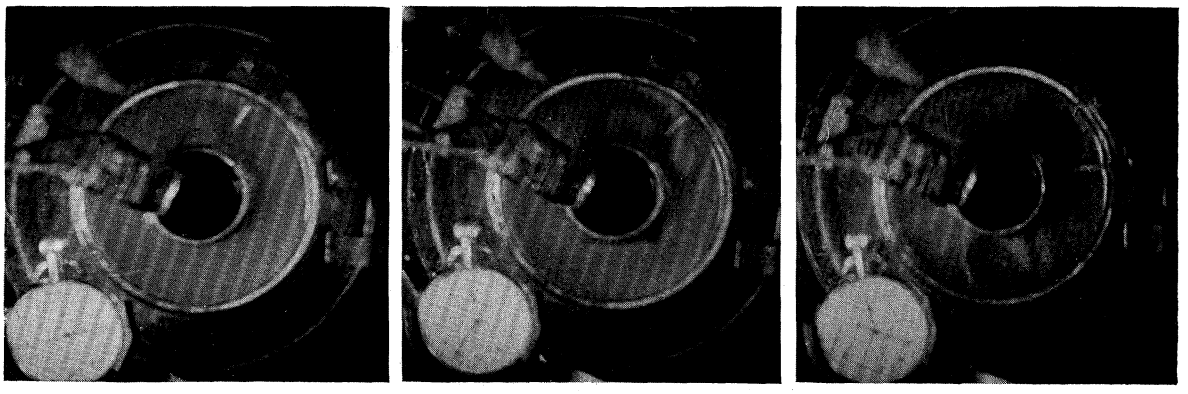

(*a*) $t = 16$ *s* (*b*) $t = 25$ *s* (*c*) $t = 40$ s

FIGURE 23. Illustrating the development of a typical wave-flow pattern (see § 4(*a*)). (*a*), (*b*) and (*c*) are photographs taken 16, 25 and 40 s, respectively, after the wave pattern had been destroyed by stirring.

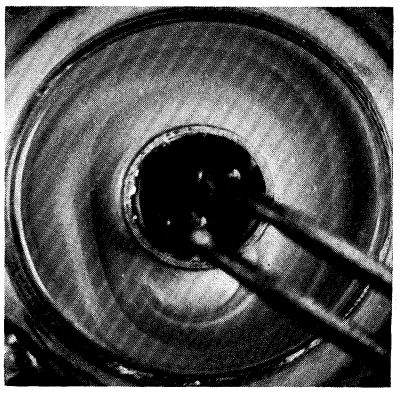

FIGURE 24

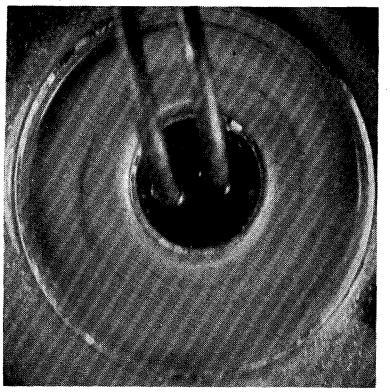

FIGURE 25

FIGURE 24. A typical observation when the transition from wave to spiral flow occurs (see § 4 (*b*)). Experimental details: $\Omega = 2{\cdot}07$ rad/s, $d = 10{\cdot}0$ cm, $\Delta\rho'/\rho_0 = -8{\cdot}3 \times 10^{-3}$, $X' = 19 \times 10^{-3}$ cm/s^2, $a = 1{\cdot}92$ cm, $b = 4{\cdot}85$ cm, rotation clockwise.

FIGURE 25. To be compared with figure 5 (*a*) in order to illustrate the dependence of the 'tightness' of the spiral on X'. Experimental details: $\Omega = 0{\cdot}86$ rad/s, $d = 10{\cdot}0$ cm, $\Delta\rho'/\rho_0 = -9{\cdot}2 \times 10^{-3}$, $X' = 120 \times 10^{-3}$ cm/s^2, $a = 1{\cdot}92$ cm, $b = 4{\cdot}85$ cm, rotation clockwise.

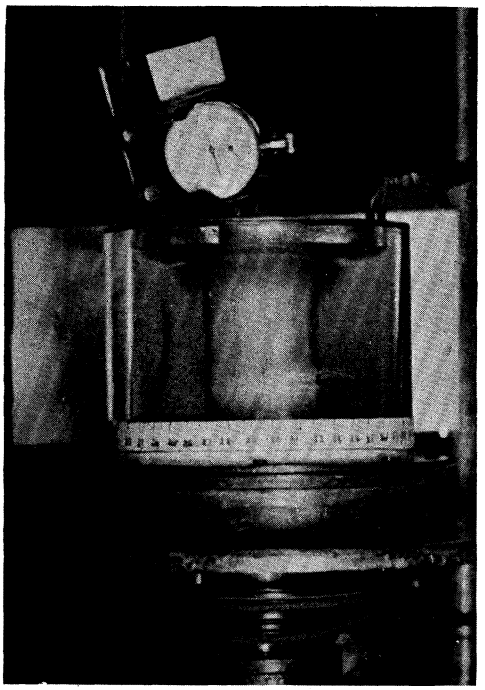

FIGURE 26. Some ink observations of the spiral flow régime through the side of the apparatus. For detailed description see the text (§ 4 (*b*)).

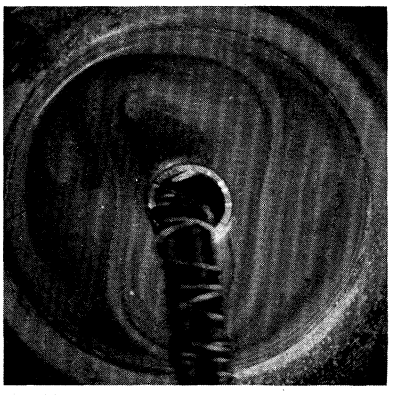

	FIGURE 27	FIGURE 28
Ω(rad/s)	2·07	3·48
$10^3\Delta\rho'/\rho_0$	−8·6	−8·6
$X'(10^{-3}$ cm s$^2)$	20	7·1
d(cm)	10·0	10·0

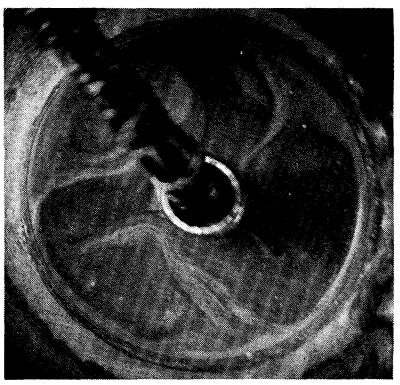

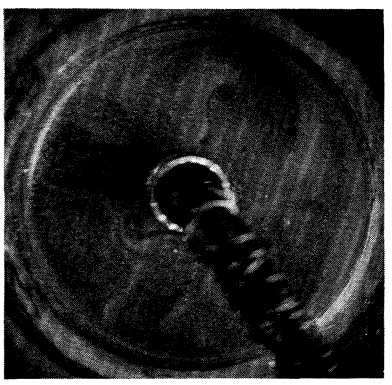

	FIGURE 29	FIGURE 30
Ω(rad/s)	6·28	6·28
$10^3\ \Delta\rho'/\rho_0$	−12	−4·7
$X'(10^{-3}$ cm s$^2)$	3·1	1·2
d (cm)	10·0	10·0

FIGURES 27 TO 30. Examples of the top-surface wave-flow pattern when the smallest ($a = 1{\cdot}06$ cm) inner cylinder was used.

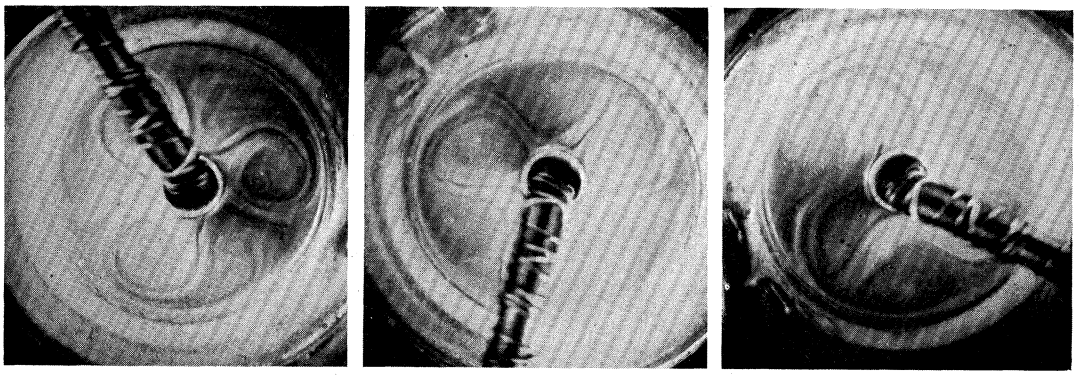

(*a*) $t = 0$ (*b*) $t = 6$ s (*c*) $t = 12$ s

(*d*) $t = 18$ *s* (*e*) $t = 24$ s (*f*) $t = 28$ *s*

FIGURE 31. 'Vacillation' cycle. Experimental details: $\Omega = 4{\cdot}71$ rad/s, $a = 1{\cdot}06$ cm, $b = 4{\cdot}85$ cm, $d = 10{\cdot}0$ cm, $\Delta\rho'/\rho_0 = -11{\cdot}8 \times 10^{-3}$, $X' = 5{\cdot}3 \times 10^{-3}$ cm s^2, rotation clockwise. For full description see text (§ 5 (*b*)).

Having made these initial observations, which were necessarily conducted in a more or less haphazard manner, specific investigations of the three régimes of flow were carried out.

5. Some specific investigations

(*a*) *Summary*

Measurements made more or less incidentally during the preliminary stages described in § 4, suggested, on subsequent analysis, the lines along which more specific investigations should proceed. Before describing these investigations in detail, the principal results will be summarized.

In § 5 (*b*) an empirical relation between the maximum wave number, $m_{\max.}$ and the geometry of the system is deduced. m appears never to exceed that value for which the wave-amplitude is equal to about two-thirds of the wavelength. In the same section 'vacillation' is described in further detail. § 5 (*c*) deals with the transition between 'wave' and 'spiral' flow. The results indicate that when ω, the drift angular velocity of the 'wave' flow pattern, reaches a certain value, which is proportional to Ω and depends on a, but is independent of d, the transition to 'spiral' flow occurs. The values of m at which this transition was observed ($m_{\min.}$, say) are also given, from which an empirical relationship between $m_{\min.}$ and b and a is deduced.

In § 5 (*d*) an account is given of experiments which set out to find the dependence of ω, the drift angular velocity, on the impressed conditions. ω appears not to depend directly on m (except insomuch as m is related to X'). ω is tentatively identified with ω', the mean zonal angular velocity introduced in § 2 (*e*).

From some of the earlier observations it was possible to deduce an essentially statistical relation between m and ω/Ω. This relation was subsequently investigated outside the range for which it was first established (see § 5 (*e*)).

The heat flow data are given in § 5 (*f*). Although they probably contain systematic errors, these data suggest that the rate at which heat is transported by the convecting system does not depend very strongly on Ω. In § 5 (*g*) an investigation is described of the temperature distribution associated with a typical wave flow.

In all the quantitative work the outer cylinder was warmer than the inner cylinder and b was always 4·85 cm. In cases where accurate determinations of $T_b - T_a$ were needed (e.g. § 5 (*d*)) the brass cylinder B (figure 2) was employed (see § 3(*b*)).

Although the results are presented with some discussion in this section, it is only when they are considered as a whole in § 6 that the full relevance of the theoretical comments of § 2 (*b*) emerges.

(*b*) *Vacillation and* $m_{\max.}$

Table 1 contains a list of the values of $m_{\max.}$, the highest values of m observed at each value of a. In the third column the quantity $\Sigma_{\max.}$, the value of Σ corresponding to $m = m_{\max.}$, is given for each value of a, where

$$\Sigma \equiv \frac{m}{\pi}\left(\frac{b-a}{b+a}\right) \tag{5·1}$$

is the ratio of the wave amplitude, $(b-a)$, to the wavelength, $\pi(b+a)/m$. It appears that

$$\Sigma_{\max.} \simeq 0{\cdot}67. \tag{5·2}$$

'Vacillation' sets in when X' has been reduced to a sufficiently low value. When $a = 1{\cdot}92$ cm, it was fairly difficult to produce a 'vacillating' flow ($m = 5$) in which the waves 'vacillated' in unison with one another. This led to an attempt to reduce $m_{\max.}$ and it was found that with $a = 1{\cdot}06$ cm, $m_{\max.} = 3$ (see table 1). Figures 27 to 30, plate 11, are presented to show the effect of decreasing X' from 20×10^{-3} cm s^2 to $1{\cdot}2 \times 10^{-3}$ cm s^2. (Spiral flow occurred in this case at $X' = 25 \times 10^{-3}$ cm s^2.) Figures 27 and 28 are pictures of well-organized wave patterns with $m = 2$ and $m = 3$ respectively. The effect of decreasing X' from $7{\cdot}1 \times 10^{-3}$ to $3{\cdot}1 \times 10^{-3}$ cm s^2 is to destroy the regularity of the wave flow, although a wave number of 3 is still recognizable (figure 29). Finally, figure 30 shows the even more unstable flow resulting from a further reduction of X' to $1{\cdot}2 \times 10^{-3}$ cm s^2.

TABLE 1. THE MAXIMUM WAVE NUMBER ($m_{\max.}$)

radius of inner cylinder a (cm)	maximum wave number $m_{\max.}$	corresponding ratio of wave amplitude to wavelength, $\Sigma_{\max.}$
3·54	14	0·69
2·85	8	0·67
2·35	6	0·66
1·92	5	0·68
1·44	4	0·69
1·06	3	0·64

'Vacillation' is a transitional phenomenon which occurs at some stage between flows of the types shown in figures 28 and 29. Figure 31, plate 12, for which $X' = 5{\cdot}3 \times 10^{-3}$ cm s^2, is composed of six photographs taken at different instants, which depict typical stages of the 'vacillation' cycle; the 'vacillation' period for the case illustrated is 28 s. Because only a plate camera was available when this experiment was performed it was not possible to obtain six pictures of the same cycle. The times in seconds given in the legend are the intervals based on an arbitrary $t = 0$ for different cycles.

At $t = 0$ there are three intense cyclones and the 'jet' stream is completely interrupted. Six seconds later the cyclones have decayed, and the 'jet' stream has been re-established. There is a slight westward tilt of the wave crests. At $t = 12$ s this tilt is more pronounced and the width of each wave is now less than before. During the interval $t = 12$ to 18 s the wave crests began to come forward towards the symmetrical disposition in which they are found at $t = 18$ s. Although the waves pass through the symmetrical position, before they can develop an appreciable eastward tilt the whole pattern begins to 'roll up' into three intense cyclones ($t = 24$ s) and finally, at $t = 28$ s the cycle is complete.

Perhaps it is noteworthy that 'vacillation' is associated with a period of the same order as the 'zonal index cycle' of the atmospheric circulation, namely, about that taken for thirty revolutions of the system (approximately a month in the atmospheric case). For details of the zonal index cycle, see Rossby & Willett (1948). This atmospheric phenomenon is characterized by a fluctuation between mainly zonal flow at one extreme and cellular flow with strong north-south components at the other.

The drift rate, ω, was observed to vary during 'vacillation'; it was slower at $t = 0$ than at those times when the 'jet' stream was well developed. The mean value of ω did not, however, change significantly from one cycle to the next. In the case shown in figure 31, $\omega = 0{\cdot}050$ rad/s,

corresponding to a period $\tau_0 = 2\pi/(m\omega) = 42$ s. This should be compared with $\tau = 28$ s, the 'vacillation' period. It is perhaps fortuitous that in this case $\tau:\tau_0 = 2:3$, but this result did suggest that a direct comparison of τ and τ_0, over that range of X' for which 'vacillation' could be produced, might lead to interesting results.

To eliminate errors which would arise through estimating τ and τ_0 separately, a direct comparison was made with the the aid of a three-pen chronograph. Often it was possible to follow several cycles before some temporary change in the flow pattern made it profitless to continue that particular 'run'. Four such experiments in which any confidence can be placed were performed. Ω and d were kept constant at 4·71 rad/s and 10 cm, respectively, and X' was varied from $4{\cdot}2 \times 10^{-3}$ to $5{\cdot}8 \times 10^{-3}$ cm s^2 by changing $\Delta\rho'$.

The results are given in table 2. N and N_0 are the number of events ('vacillation' cycles

TABLE 2. 'VACILLATION' PERIOD AGAINST WAVE PERIOD

($\Omega = 4{\cdot}71$ rad/s, $d = 10$ cm, $m = 3$.)

$10^3 X'$ (cm s^2)	N	N_0	$\tau:\tau_0$
4·2	24	17	3:4
4·7	32	24	3:4
5·3	—	—	2:3
5·5	30	20	2:3
5·8	38	25	2:3

and passages of a wave crest past a fixed point, respectively) recorded on the chronograph. We can expect errors of unity in N and N_0. The final column of table 2 gives the nearest simple integer ratios to $\tau_0:\tau$. These results suggest that τ and τ_0 are simply related, but that their ratio changes from 3:4 to 2:3 when X' lies somewhere between $4{\cdot}7 \times 10^{-3}$ and $5{\cdot}3 \times 10^{-3}$ cm s^2. It may be that 'vacillation' is simply a more developed form of a slight wavering motion occasionally observed at higher values of X'. If this be the case then wavering is not a spurious phenomenon, and in view of the apparently simple relation between τ and τ_0 wavering may be the result of interference between a predominant mode, wave number m, other modes which are being excited at the same time.

(*c*) *The transition between 'wave' flow and 'spiral' flow*

The very first observations were made under conditions at which 'wave' flow occurred. At that time, no attempt was made to obtain accurate measurements (indeed it was not too clear what to measure); the objective was to gain an overall picture of the phenomena under investigation. The outer cylinder was glass and T_o and T_i were not always recorded separately; only their difference, $T_o - T_i = \Delta T$, was measured, with a thermocouple.

During an experiment with $a = 1{\cdot}92$ cm, $\Omega = 2{\cdot}07$ rad/s and $d = 10$ cm, in which ΔT was increased in steps and rough ω determinations made by timing the drift through a known angular distance (see § 5 (*d*)), the transition to 'spiral' flow was first observed. At $\Delta T = 32$ °C a 'wave' flow ($m = 2$) pattern occurred. On increasing ΔT to about 35° C, the 'wave' pattern suddenly disappeared, giving way to a spiral. This experiment was then repeated at a lower rotation rate, $\Omega = 1{\cdot}18$ rad/s. The transition then occurred at a much lower value of ΔT than in the previous case. The transition had not been observed during earlier experiments at $\Omega = 3{\cdot}48$ rad/s, presumably because a sufficiently high value of ΔT had not been attained.

To investigate the transition more fully the same general procedure as in the first experiments was adopted, but rather more accurate measurements of ω were obtained. Six determinations of the time taken for the pattern to drift through a right angle were made at each value of ΔT. The individual measurements usually agreed with one another to within 20%. Although ΔT was not constant during the course of making these measurements, it never changed by more than 5% during the few minutes normally taken. ΔT was read before and after the timing measurements were made and the mean value taken.

On reaching a value of ΔT very close to the transition point fluctuations of the kind described above in § 4 (*b*) occurred. The transition point was recognized when, as ΔT was increased slowly, these fluctuations ceased and 'spiral' flow was firmly established. The power supply to the hot bath was then adjusted to prevent ΔT from rising still further. After disturbing the 'spiral' flow by stirring fairly vigorously, it would reappear after a few minutes.

TABLE 3. THE DRIFT ANGULAR VELOCITY AT THE ONSET OF SPIRAL FLOW

($a = 1{\cdot}92$ cm, $d = 10$ cm, $m_{\text{min.}} = 2$ in each case.)

Ω (rad/s)	$\omega_{\text{crit.}}$ (rad/s) $10^{-2}\times$	$\omega_{\text{crit.}}/\Omega$ $10^{-2}\times$	no. of determinations
2·07	$8{\cdot}7 \pm 1{\cdot}0$	$4{\cdot}2 \pm 0{\cdot}5$	3
1·56	$6{\cdot}0 \pm 1{\cdot}0$	$3{\cdot}8 \pm 0{\cdot}6$	2
1·18	$4{\cdot}0 \pm 0{\cdot}6$	$3{\cdot}4 \pm 0{\cdot}5$	3
0·86	$2{\cdot}9 \pm 0{\cdot}3$	$3{\cdot}5 \pm 0{\cdot}4$	3
	(mean with standard error)	$3{\cdot}7 \pm 0{\cdot}2$	

$\Delta T_{\text{crit.}}$, the transition value of ΔT, was reproducible to within about 10%. It was found at four different values of Ω. $\omega_{\text{crit.}}$, the corresponding value of ω, was obtained by extrapolating the ω versus ΔT data, judgement being mainly by eye. The results are given in table 3. The error quoted in $\omega_{\text{crit.}}$ is guessed; it is the uncertainty in ω read at the mean $\Delta T_{\text{crit.}}$ point. Because this error is small a guess is sufficiently accurate.

The interesting result revealed by these data is that to within the errors involved, $\omega_{\text{crit.}}/\Omega$ is constant. The next question to arise was whether $\omega_{\text{crit.}}/\Omega$ depends on d and a. To examine this question, further observations were made, the results of which are given in table 4. In the last column of this table the value of m occurring just before 'spiral' flow set in is tabulated. This quantity has been termed $m_{\text{min.}}$. For a given geometry, $m_{\text{min.}}$ was usually, but not always the same. The number of observations is included in parenthesis in the $m_{\text{min.}}$ column. For example, when $a = 3{\cdot}54$ cm and $\Omega = 2{\cdot}07$ rad/s four determinations of $\omega_{\text{crit.}}$ were made. Twice was the transition observed at $m = 5$ and twice at $m = 6$.

The following conclusions have been drawn from the results listed in table 4. First, according to the measurements at $a = 2{\cdot}85$ cm there is no significant dependence of $\omega_{\text{crit.}}/\Omega$ on d. Secondly, there seems to be no systematic dependence of

$$\frac{\omega_{\text{crit.}}}{\Omega}\frac{1}{2}\frac{b+a}{b-a} = 0{\cdot}046 \pm 0{\cdot}001 \quad \text{(standard error)} \tag{5·3}$$

on a (see column 5 of table 4).

In table 5, values of $\Sigma_{\text{min.}}$ (see equation (5·1)) are listed alongside the values of $m_{\text{min.}}$ given in table 4. Those figures in parentheses correspond to the less frequently observed values of $m_{\text{min.}}$. If we ignore the $a = 1{\cdot}06$ cm result, $m_{\text{min.}}$ is roughly constant.

It must be recorded that there were a few unsuccessful attempts to estimate $\omega_{\text{crit.}}$. The difficulty then was to produce sufficiently well organized flow for reasonably accurate velocity determinations to be made, and always arose when d was less than about 3·5 cm.

TABLE 4. ALL THE $(\omega_{\text{crit.}}/\Omega)$ DETERMINATIONS

(Number of measurements in parenthesis in $m_{\text{min.}}$ column.)

a (cm)	$\frac{2(b-a)}{b+a}$	d (cm)	Ω (rad/s)	$\frac{10^2(\omega_{\text{crit.}}/\Omega)}{2(b-a)/(b+a)}$	$m_{\text{min.}}$
1·06	1·29	10·0	2·07	4·1 ± 0·3	2 (2)
		10·0	1·18	4·5 ± 0·3	2 (2)
1·92	0·86	10·0	2·07	4·9 ± 0·5	2 (3)
		10·0	1·56	4·4 ± 0·4	2 (2)
		10·0	1·18	4·0 ± 0·7	2 (3)
		10·0	0·86	4·1 ± 0·4	2 (3)
2·07	0·80	10·0	2·07	4·0 ± 0·5	2 (2)
		10·0	1·56	4·6 ± 0·5	2 (2)
		10·0	1·18	4·5 ± 0·5	2 (2)
		10·0	0·86	4·5 ± 0·5	2 (3)
2·35	0·69	10·0	3·48	4·2 ± 0·4	2 (1), 3 (1)
		10·0	1·18	5·2 ± 0·5	3 (2)
2·56	0·61	10·0	4·71	4·8 ± 0·4	3 (2)
		10·0	3·48	4·5 ± 0·4	2 (2)
		10·0	2·07	4·9 ± 0·4	3 (2)
		10·0	1·56	5·6 ± 0·5	3 (1)
2·85	0·52	10·0	3·48	4·2 ± 0·4	4 (2)
		8·9	3·48	3·9 ± 0·6	4 (2)
		7·0	1·18	5·8 ± 0·8	4 (1)
		6·2	1·56	3·9 ± 0·6	4 (2)
		4·9	2·07	4·8 ± 0·8	4 (4)
		3·5	0·86	3·5 ± 0·6	4 (4)
3·54	0·31	10·0	4·71	4·8 ± 0·8	6 (3)
		5·2	2·07	4·2 ± 0·6	5 (2), 6 (2)
		7·6	1·18	5·8 ± 0·7	6 (4)
		(mean value with standard error)		4·6 ± 0·1	

TABLE 5. THE WAVE NUMBER IMMEDIATELY BEFORE THE ONSET OF SPIRAL FLOW $(m_{\text{min.}})$

radius of inner cylinder a (cm)	$m_{\text{min.}}$	corresponding ratio of wave amplitude to wavelength $\Sigma_{\text{min.}}$
3·54	6 (5)	0·30 (0·25)
2·85	4	0·33
2·56	3 (2)	0·29 (0·20)
2·35	3 (2)	0·33 (0·22)
2·07	2	0·25
1·92	2	0·27
1·06	2	0·41

(Where more than one value of $m_{\text{min.}}$ was observed, that which occurred the less frequently is given in parenthesis.)

Although this behaviour was entirely mysterious when it was first observed, a plausible explanation presented itself when the temperature measurements described below had been made (see § 5 (*g*)).

It was only when the criterion given by equation (5·3) had been obtained that it was realized that ω/Ω is a significant parameter, and this led to experiments which set out to investigate the dependence of ω on the impressed conditions.

(d) Some measurements of ω, the drift angular velocity

ω was estimated from several (usually about six) measurements of the time taken for the wave pattern to drift through an angle of 90°. Individual determinations of this time interval, which was of the order of tens of seconds (§ 4 (*a*)), agreed to within from 10 to 30 %. Greater reproducibility was obtained in the absence of the wavering motion described in § 4 (*a*), and when some of the more violent instabilities described in that section occurred, it was not possible to make any reliable measurement at all. (A systematic study of these instabilities, especially one which concentrates on finding the conditions under which they arise, would be of importance. The results so far throw little light on this question.)

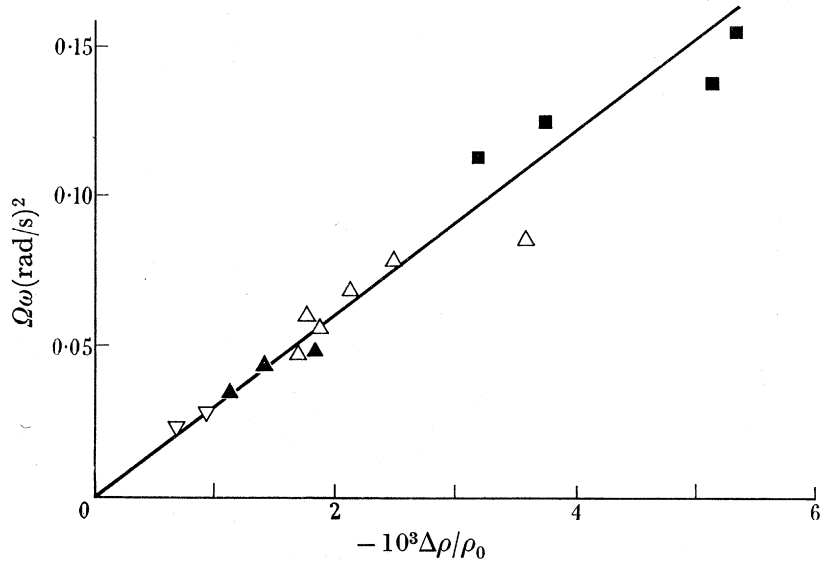

FIGURE 32. Drift angular velocity measurements, $m = 2$. Experimental details: $a = 1{\cdot}92$ cm, $b = 4{\cdot}85$ cm, $d = 10{\cdot}0$ cm. Ω(rad/s): ■, 2·07; △, 1·56; ▲, 1·18; ▽, 0·86. Slope of best straight line through origin, $30{\cdot}5 \pm 0{\cdot}8$ (rad/s)^2 (standard error).

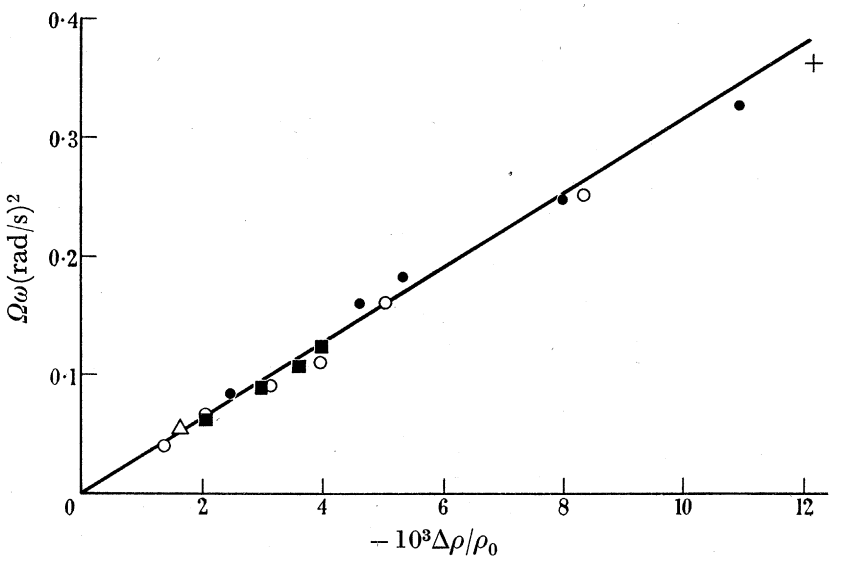

FIGURE 33. Drift angular velocity measurements, $m = 3$. Experimental details: $a = 1{\cdot}92$ cm, $b = 4{\cdot}85$ cm, $d = 10{\cdot}0$ cm. Ω (rad/s): +, 6·28; ●, 4·71; ○, 3·48; ■, 2·07; △, 1·56. Slope of best straight line through origin, $31{\cdot}2 \pm 0{\cdot}6$ (rad/s)^2 (standard error).

Very rough determinations of ω_j, the mean angular speed of flow in the top surface 'jet' stream, were obtained. Each was made by timing the motion of a suitable particle of aluminium powder over an angular distance of two right angles. Individual measurements

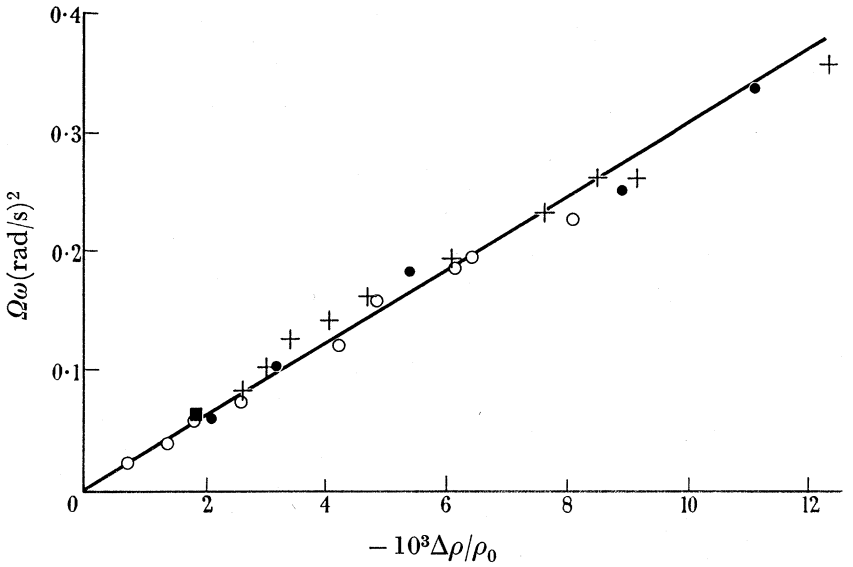

FIGURE 34. Drift angular velocity measurements, $m = 4$. Experimental details: $a = 1{\cdot}92$ cm, $b = 4{\cdot}85$ cm, $d = 10{\cdot}0$ cm. Ω (rad/s): +, 6·28; ●, 4·71; ○, 3·48; ■, 2·07. Slope of best straight line through origin, $30{\cdot}7 \pm 0{\cdot}06$(rad/s)^2 (standard error).

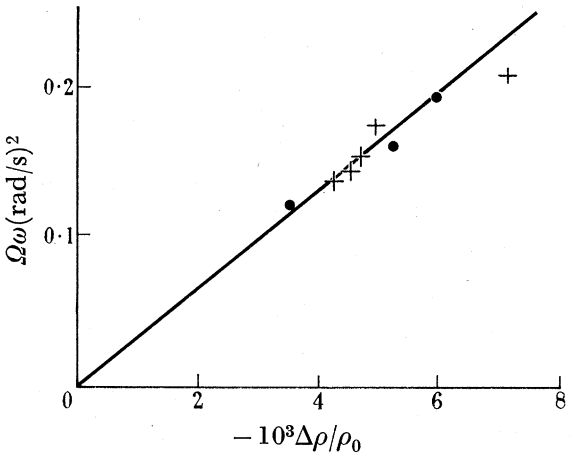

FIGURE 35. Drift angular velocity measurements, $m = 5$. Experimental details: $a = 1{\cdot}92$ cm, $b = 4{\cdot}85$ cm, $d = 10{\cdot}0$ cm. Ω (rad/s): +, 6·28; ●, 4·71. Slope of best straight line through origin, $32{\cdot}3 \pm 0{\cdot}7$ (rad/s)^2 (standard error).

of ω_j agreed with one another to within about 20% when the flow was as regular as, e.g. that of figure 5*d*. On the other hand, a particle would remain in the 'jet' stream for only a very short period when the flow was not so regular (e.g. figure 12), and for this reason ω_j could not then be estimated.

In these experiments the brass cylinder B (see figure 2) was used, and T_o and T_i were carefully measured with mercury-in-glass thermometers. $\Delta\rho$ was computed from these temperature measurements (see equation (4·2)).

The most detailed investigation was conducted with $a = 1{\cdot}92\,\text{cm}$, and the results are presented in figures 32 to 36. In the first four of these five diagrams, $\Omega\omega$ is plotted against $(\Delta\rho/\rho_0)$ for $m = 2, 3, 4$, and 5, respectively, these results having been obtained at $d = 10\,\text{cm}$. The points lie roughly on straight lines, the slopes of which are not significantly different from one another.

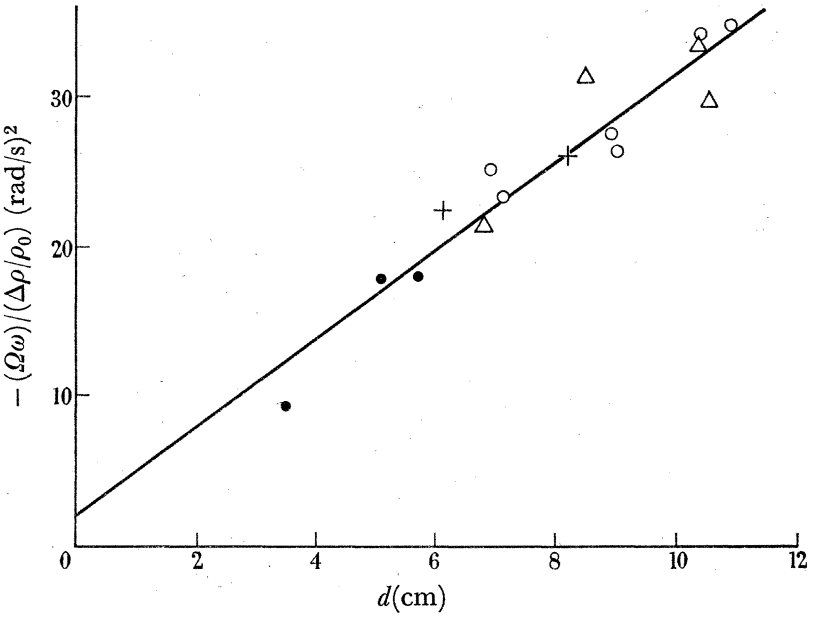

FIGURE 36. Dependence of drift angular velocity on depth. Experimental details: $a = 1{\cdot}92$ cm, $b = 4{\cdot}85$ cm.

	+	△	●	○
Ω(rad/s)	6·28	6·28	3·48	3·48
m	5	4	4	3
$10^3(\Delta\rho/\rho_0)$	8·65	8·65	6·65	6·65

equation of line $-\Omega\omega/(\Delta\rho/\rho_0) = (2{\cdot}92 \pm 0{\cdot}09)\,[d + 0{\cdot}7 \pm 0{\cdot}1]$ (standard errors).

In figure 36, $-\Omega\omega/(\Delta\rho/\rho_0)$ is plotted against d. These results are from two experiments in which $-(\Delta\rho/\rho_0)$ was $8{\cdot}65 \times 10^{-3}$ and $6{\cdot}65 \times 10^{-3}$ respectively. (It was not possible to investigate values of d less than 3·5 cm for reasons already given in § 5 (*c*).) These points lie fairly close to a straight line, the intercept on the d axis of which is at a small, but significant distance away from the origin. Let us assume that since this intercept is small, we can ignore it (see below, § 5 (*g*)) and express the foregoing results by the empirical formula

$$\frac{\omega}{\Omega} = -(3{\cdot}12 \pm 0{\cdot}03)\frac{d}{\Omega^2}\frac{\Delta\rho}{\rho_0} \quad \text{(standard error)} \tag{5·4}$$

when $a = 1{\cdot}92$ cm and $b = 4{\cdot}85$ cm.

During subsequent investigations (see § 5 (*e*)) a few ω determinations at further values of a were made more or less incidentally; in no case was d less than 6 cm. These results are summarized in table 6. The data given in the last column suggests that

$$-\left(\frac{b^2 - a^2}{2d}\right)\Omega\omega \Big/ \frac{\Delta\rho}{\rho_0} = 28{\cdot}5 \pm 0{\cdot}8\,\text{cm/s}^2 \quad \text{(standard error)}, \tag{5·5}$$

although further measurements will have to be made to establish whether the apparently significant deviations from this mean value are due to errors of interpretation, or to systematic errors caused, perhaps, by evaporative cooling (see § 5(*g*)). This result leads to the physical ideas put forward in § 6.

TABLE 6. SUMMARY OF THE DRIFT ANGULAR VELOCITY MEASUREMENTS

a (cm)	$b-a$ (cm)	$\frac{1}{2}(b+a)$ (cm)	$-\frac{(b^2-a^2)}{2d}\Omega\omega\Big/\frac{\Delta\rho}{\rho_0}$ (cm/s^2)
3·54	1·31	4·20	$25\pm1·1$
2·85	2·00	3·85	$26\pm1·4$
2·35	2·50	3·60	$29\pm1·8$
2·07	2·78	3·46	$32\pm2·0$
1·92	2·93	3·39	$30·5\pm0·3$
1·44	3·41	3·15	$29\pm1·0$
1·06	3·79	2·95	$28\pm1·0$

The only point of interest that emerges from the ω_j measurements is that ω_j is about an order of magnitude larger than ω. Within the large errors involved (ω_j/ω) shows no dependence on a, Ω and d. However, in the case studied most closely ($a = 1·92$ cm) the following results were found:

$$m = \quad 2 \qquad 3 \qquad 4 \qquad 5$$
$$\omega_j/\omega = 7·2\pm0·6, \quad 8·5\pm0·6, \quad 8·4\pm0·5, \quad 9·3\pm0·8.$$

(*e*) *The dependence of m on* (ω/Ω)

When the data presented in figures 32 to 36 had been obtained, an attempt was made to analyze them, and earlier data, to discover what factors determine m. Although it was evident that m decreases as (ω/Ω) increases there was no consistency between the values of (ω/Ω) at which m had been seen to change. Thus, it was necessary to seek an essentially statistical relation. In table 7, the results for $a = 1·92$ cm are summarized. The central or median values, $\overline{(\Omega/\omega)}$, obtained from these histograms are listed in table 8. In the same table the '25% points' of the histograms, $(\Omega/\omega)_-$ and $(\Omega/\omega)_+$, are also listed.

TABLE 7. FREQUENCY DISTRIBUTION: m AGAINST Ω/ω

($a = 1·92$ cm.)

m \ Ω/ω	<50	51 to 100	101 to 150	151 to 200	201 to 250	251 to 300	301 to 350	351 to 400	401 to 450	451 to 500	total no. of observations
2	40	2	0	0	0	0	0	0	0	0	42
3	12	26	14	3	1	1	0	0	0	0	52
4	0	17	23	15	8	7	2	2	1	0	75
5	0	0	4	6	6	4	0	0	0	0	20

The data given in table 8 appear to fit the formula

$$(\overline{\Omega/\omega})^{\frac{1}{2}} = (3·0\pm0·2)\,[m+(0·04\pm0·3)] \quad \text{(standard errors)}, \tag{5·6}$$

the meaning of which is presumably the following: Although there is no unique dependence of m on (Ω/ω), for a given value of the latter quantity the most likely value of m is the nearest integer to that obtained by inserting the value of $(\Omega/\omega)^{\frac{1}{2}}$ in the left-hand side. The last result suggested how a specific investigation of the dependence of m on a should be performed. At each particular set of conditions chosen, the most frequently occurring

value of m was found by repeating the procedure of destroying the flow pattern and noting the value of m after the wave flow had been allowed to reform.

TABLE 8. COMPARISON OF OBSERVATIONS WITH BEST LINEAR RELATION BETWEEN m AND $\overline{(\Omega/\omega)}^{\frac{1}{2}}$

($a = 1{\cdot}92$ cm.)

m	$(\Omega/\omega)_-$	$\overline{(\Omega/\omega)}$	$(\Omega/\omega)_+$	$\overline{(\Omega/\omega)}^{\frac{1}{2}}$ (calc.)	δ	total no. of observations
2	22	30	42	4·8	−0·3	42
3	60	82	115	8·7	+0·4	57
4	100	143	200	11·7	+0·4	75
5	150	207	260	14·7	−0·3	20

$\overline{(\Omega/\omega)}^{\frac{1}{2}}$ (calc.) given by equation (5·6); δ is the difference between the calculated and observed values of $\overline{(\Omega/\omega)}^{\frac{1}{2}}$.

The most probable value of m was found in this way at many values of X (see equation (4·1)), the procedure being as follows. A preliminary investigation was made to discover the range of X to be covered, from which suitable intervals of X could be decided. This was followed by a few careful determinations of ω (see table 6). To vary X, changes in Ω, $\Delta\rho$ and d were made, but in no case was d less than 6 cm. The investigation covered values of $a = 2{\cdot}35$, 2·85 and 3·54 cm, and the results are given in tables 9 to 14.

TABLE 9. FREQUENCY DISTRIBUTION: m AGAINST Ω/ω

($a = 2{\cdot}35$ cm)

m \ Ω/ω	25	30	35	40	45	50	75	100	125	150	175	200	225	250	275	300	325
spiral flow	20	18	2	0	0	0	0	0	0	0	0	0	0	0	0	0	0
2	0	1	0	1	0	0	0	0	0	0	0	0	0	0	0	0	0
3	0	1	17	18	16	6	0	0	0	0	0	0	0	0	0	0	0
4	0	0	1	1	4	14	12	11	2	1	1	0	0	0	0	0	0
5	0	0	0	0	0	0	8	9	18	13	8	9	6	4	2	0	0
6	0	0	0	0	0	0	0	0	11	16	11	11	14	16	18	20	20

TABLE 10. COMPARISON OF OBSERVATIONS WITH BEST LINEAR RELATION BETWEEN m AND $\overline{(\Omega/\omega)}^{\frac{1}{2}}$

($a = 2{\cdot}35$ cm, $\overline{(\Omega/\omega)}^{\frac{1}{2}} = (3{\cdot}2 \pm 0{\cdot}2)\ [m - (1{\cdot}2 \pm 0{\cdot}4)]$ (standard errors))

m	$(\Omega/\omega)_-$	$\overline{(\Omega/\omega)}$	$(\Omega/\omega)_+$	$\overline{(\Omega/w)}^{\frac{1}{2}}_{(\text{calc.})}$	δ	total no. of observations
3	37	40	45	6·3	+0·4	58
4	53	76	100	8·7	−0·4	47
5	115	146	198	12·1	−0·2	77
6	200	250	—	15·9	+0·4	—

The results of the $a = 2{\cdot}35$ cm experiment are given in table 9. In this case $(\omega_{\text{crit.}}/\Omega)^{-1} = 31$ (see § 5 (c)). Only on two occasions was $m = 2$ observed, a result in accord with the data of table 4. Since $m_{\text{max.}} = 6$, only one side of the $m = 6$ histogram could be obtained. The values of $\overline{(\Omega/\omega)}$ for $m = 3$, 4 and 5 were obtained by interpolation and these values, together with that guessed for $m = 6$, are listed in table 10. These results appear to fit the relation

$$\overline{(\Omega/\omega)}^{\frac{1}{2}} = A(m - m') \quad \text{for} \quad m_{\text{max.}} > m \geqslant m_{\text{min.}}, \tag{5·7}$$

(see equation (5·6)) if $A = 3{\cdot}2 \pm 0{\cdot}2$ and $m' = 1{\cdot}2 \pm 0{\cdot}4$ (standard errors).

In tables 11 to 14, the results for $a = 2{\cdot}85$ cm and $3{\cdot}54$ cm are given and treated in the same way as those for $a = 2{\cdot}35$ cm. Again the relation given by equation (5·7) appears to hold, and the corresponding values of A and m' are listed in table 15. Consider the results given in this table. There seems to be no systematic variation of A with a; the mean value of A is $3{\cdot}1 \pm 0{\cdot}1$ (standard error). However m' increases with a, and three of the four values of m' listed are not significantly different from integers, although the fourth value,

TABLE 11. FREQUENCY DISTRIBUTION: m AGAINST Ω/ω

($a = 2{\cdot}85$ cm.)

m \ Ω/ω	30	40	50	60	70	105	140	175	210	245	280	315	350	385	420	455	490
spiral flow	24	10	0	0	0	0	0	0	0	0	0	0	0	0	0	0	0
4	0	14	23	20	7	0	0	0	0	0	0	0	0	0	0	0	0
5	0	0	1	2	11	13	6	3	2	0	0	0	0	0	0	0	0
6	0	0	0	2	4	10	14	13	12	6	2	0	0	0	0	0	0
7	0	0	0	0	2	0	4	6	10	17	9	7	7	2	1	0	0
8	0	0	0	0	0	0	0	0	0	1	13	17	17	22	23	24	24

TABLE 12. COMPARISON OF OBSERVATIONS WITH BEST LINEAR RELATION BETWEEN m AND $\overline{\Omega/\omega}^{\frac{1}{2}}$

($a = 2{\cdot}85$ cm, $(\overline{\Omega/\omega})^{\frac{1}{2}} = (2{\cdot}9 \pm 0{\cdot}2)\ [m - (1{\cdot}5 \pm 0{\cdot}2)]$ (standard errors))

m	$(\Omega/\omega)_-$	$(\overline{\Omega/\omega})$	$(\Omega/\omega)_+$	$(\overline{\Omega/\omega})^{\frac{1}{2}}_{\text{(calc.)}}$	δ	total no. of observations
4	—	50	—	7·2	−0·1	64
5	73	101	132	10·0	+0·1	38
6	122	161	205	12·9	−0·2	63
7	207	250	320	15·7	+0·1	66
8	315	350	—	18·5	+0·2	—

TABLE 13. FREQUENCY DISTRIBUTION: m AGAINST Ω/ω

($a = 3{\cdot}54$ cm.)

m \ Ω/ω	110	210	310	410	510	610	710	810	910	1010	1110	1210	1310	1410	1510	1610	1710	1810
6	30	10	0	0	0	0	0	0	0	0	0	0	0	0	0	0	0	0
7	0	15	3	2	0	0	0	0	0	0	0	0	0	0	0	0	0	0
8	0	5	18	15	2	1	0	0	0	0	0	0	0	0	0	0	0	0
9	0	0	6	10	4	5	0	0	0	0	0	0	0	0	0	0	0	0
10	0	0	4	2	23	22	8	3	3	0	0	0	0	0	0	0	0	0
11	0	0	0	2	3	2	19	20	10	3	0	0	0	0	0	0	0	0
12	0	0	0	0	0	0	3	7	16	21	10	6	6	0	1	0	0	0
13	0	0	0	0	0	0	0	0	1	6	15	18	16	16	12	12	5	0
14	0	0	0	0	0	0	0	0	0	0	5	6	8	4	17	18	25	30

TABLE 14. COMPARISON OF OBSERVATIONS WITH BEST LINEAR RELATION BETWEEN m AND $(\overline{\Omega/\omega})^{\frac{1}{2}}$

($a = 3{\cdot}54$ cm, $(\overline{\Omega/\omega})^{\frac{1}{2}} = (3{\cdot}4 \pm 0{\cdot}2)\ [m - (2{\cdot}7 \pm 0{\cdot}5)]$ (standard errors))

m	$(\Omega/\omega)_-$	$(\overline{\Omega/\omega})$	$(\Omega/\omega)_+$	$(\overline{\Omega/\omega})^{\frac{1}{2}}_{\text{(calc.)}}$	δ	total no. of observations
7	196	228	261	14·8	+0·3	20
8	253	352	417	18·1	+1·0	41
9	361	425	535	21·5	−0·8	25
10	490	575	650	25·0	−0·9	65
11	738	776	850	28·0	0	59
12	910	1030	1110	32·0	−0·2	70
13	1180	1320	1500	35·3	+1·2	101

$m' = 1{\cdot}5 \pm 0{\cdot}2$ (at $a = 2{\cdot}85$ cm) differs by more than twice its standard error from both 1 and 2. If we assume that the true values of m' are 0, 1, 2 and 3, respectively, the mean of the residuals of the measured values is $0{\cdot}04 \pm 0{\cdot}35$; hence, the results are not inconsistent with this assumption.

If we compare m' and $m_{\text{min.}}$ (see table 5), the first three values listed in table 15 suggest that $m_{\text{min.}} - m' = 2$, although the last value (for $a = 3{\cdot}54$ cm) is apparently inconsistent with this suggestion. If we make the hypothesis that m' is an integer differing by 2 from $m_{\text{min.}}$, then the mean of the residuals amounts to $1{\cdot}04 \pm 0{\cdot}35$, which is not insignificant.

TABLE 15. SUMMARY OF THE m AGAINST $(\overline{\Omega/\omega})^{\frac{1}{2}}$ RESULTS

		defined by equation (5·7)			
a (cm)	$2(b-a)/(b+a)$	A	m'	$m_{\text{max.}}$	$m_{\text{min.}}$
1·92	0·86	$3{\cdot}0 \pm 0{\cdot}2$	$-0{\cdot}04 \pm 0{\cdot}3$	5	2
2·35	0·69	$3{\cdot}2 \pm 0{\cdot}2$	$1{\cdot}2 \pm 0{\cdot}4$	6	3 (2)
2·85	0·52	$2{\cdot}9 \pm 0{\cdot}2$	$1{\cdot}5 \pm 0{\cdot}2$	8	4
3·54	0·31	$3{\cdot}4 \pm 0{\cdot}2$	$2{\cdot}7 \pm 0{\cdot}2$	14	6 (5)

(*f*) *Heat-flow measurements*

It is usual to present heat-flow data in terms of the Nusselt number, Nu, a dimensionless parameter which is the actual heat flow H measured in terms of the heat flow by conduction if convection did not occur. Thus, assuming no heat loss at the top and bottom surfaces and ignoring any other end effects

$$Nu \equiv \frac{H \ln (b/a)}{2\pi\chi d(T_b - T_a)}, \tag{5·8}$$

where χ, the thermal conductivity, is $1{\cdot}4 \times 10^{-3}$ cal/cm s °C for water at 15 °C and depends so slightly on temperature that this variation may safely be ignored.

H was estimated from the known rate Q at which water circulated through the cool bath (see § 3 (*b*)) and the rise in temperature ΔT_c, using the relation

$$H = \rho c Q \Delta T_c, \tag{5·9}$$

where both ρ and c, the density and specific heat, respectively, may be taken as unity.

During many of the early experiments not designed specifically to investigate heat flow, measurements were made from which only inaccurate determinations of H, or Nu, could be obtained. The errors were due to two main causes. First, no null experiments were made to determine the heat flow in the absence of water in the convection chamber, and second, Q was at first subject to erratic fluctuations due to the sucking action of the filter pump.

In obtaining the heat flow data given here, null experiments were performed and the rate at which water flowed through the cool bath was maintained constant by means of a syphon arrangement. A few estimates of Nu were obtained in the 'wave' flow régime to discover the dependence of the heat flow on d, $\Delta\rho$ and Ω. The only careful measurements were made with $a = 1{\cdot}92$ cm. The electrical energy input was also measured, and thus found to be about 10% greater than H, showing that most of the input heat reached the cool bath.

The results are given in figures 37 and 38. They indicate that although Nu increases slowly with $\Delta\rho$, within the experimental errors involved, over the limited range studied Nu does not depend greatly on Ω and d.

Fishenden & Saunders (1950) have described the dependence of *Nu* on other parameters for a non-rotating fluid. *Nu* is a function of two parameters, the Prandtl number (see equation (2·17)) and the Grashof number which in our case should be written

$$Gr \equiv \frac{g(b-a)^3}{\nu^2}\frac{\Delta\rho}{\rho_0}. \tag{5·10}$$

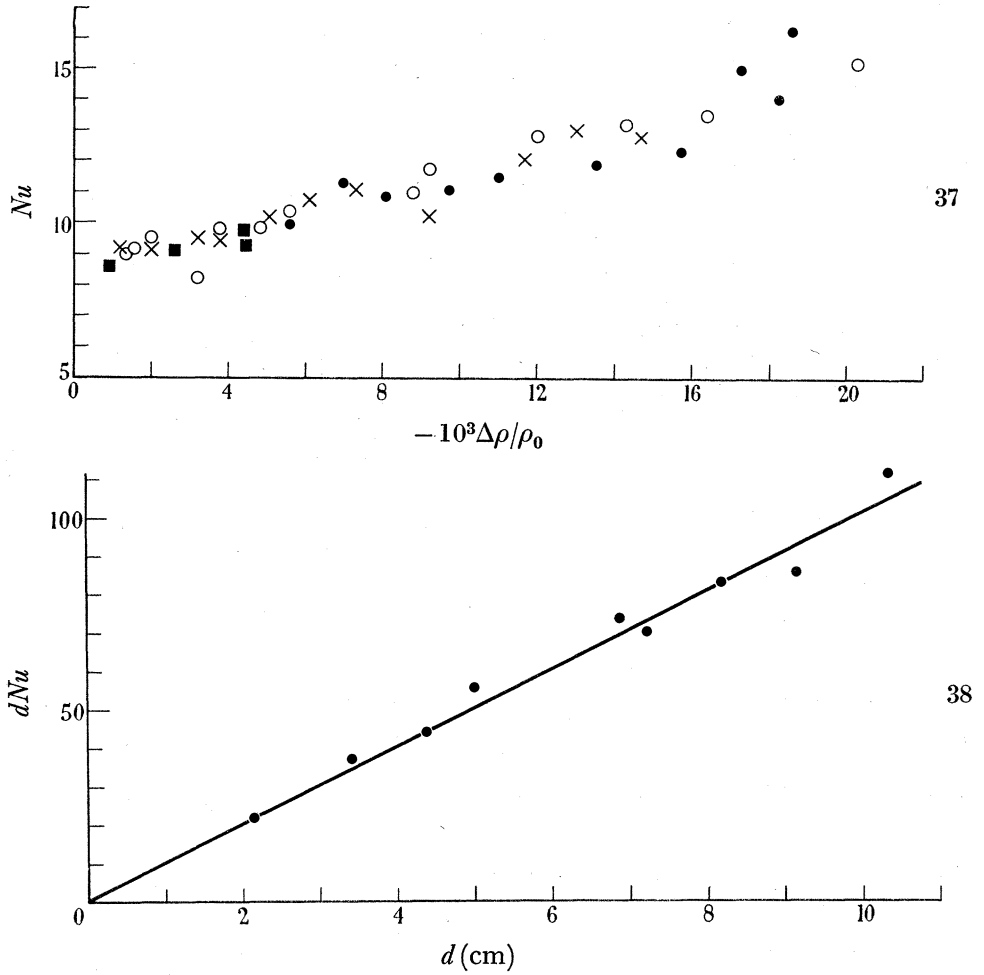

FIGURES 37 AND 38. Heat flow results. In figure 37 the Nusselt number is plotted against the fractional density contrast for $a = 1{\cdot}92$ cm, $b = 4{\cdot}85$ cm, $d = 10{\cdot}0$ cm. Ω(rad/s): ●, 6·28; ○, 4·71; ×, 3·48; ■, 2·07. In figure 38, the results of an experiment to determine the dependence of *Nu* on *d* are plotted. Experimental details: $a = 1{\cdot}92$ cm, $b = 4{\cdot}85$ cm, $\Omega = 3{\cdot}48$ rad/s, $-\Delta\rho/\rho_0 = 3{\cdot}4 \times 10^{-3}$.

On inserting values of *Gr* and *Pr* typical of these experiments into Fishenden & Saunders's results for a non-rotating liquid, one finds a range of *Nu* from 15 to 40. In view of the probable errors both of interpretation and of measurement involved, it cannot be judged whether this is significantly different from the measured range, namely 9 to 16 (see figure 37).

(*g*) *An investigation of the temperature distribution*

A description of the apparatus employed in this investigation is given in § 3(*e*). This section is an account of the few measurements which were made with it by the present writer.

Two sets of conditions were studied. In the first, for which $a = 1{\cdot}92$ cm, $d = 10{\cdot}2$ cm, $b = 4{\cdot}85$ cm, $T_a = 9$ °C, $T_b = 32$ °C and $\Omega = 4{\cdot}71$ rad/s, the flow was subcritical, wave number $m = 4$. The second set of conditions were the same as the first, with the one exception that $\Omega = 1{\cdot}18$ rad/s; then the flow was supercritical. The junctions of the thermocouples were located at various heights z above the bottom of the convection chamber, on an imaginary cylinder $r = \frac{1}{2}(b+a)$.

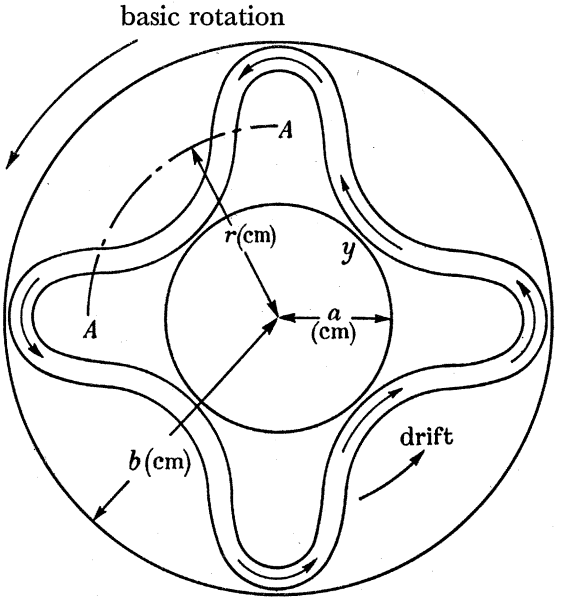

FIGURE 39. Schematic diagram of top-surface flow pattern. Arrows indicate the direction of flow. AA is section along which the temperature profiles of figures 40 and 41 were obtained. Experimental details: $a = 1{\cdot}92$ cm, $b = 4{\cdot}85$ cm, $d = 10{\cdot}2$ cm, $r = 3{\cdot}4$ cm, $\Omega = 4{\cdot}71$ rad/s, $T_a = 9{\cdot}0$ °C, $T_b = 32{\cdot}0$ °C, $\rho(T_a) - \rho(T_b) = -\Delta\rho = 4{\cdot}76 \times 10^{-3}$ g/cm^3.

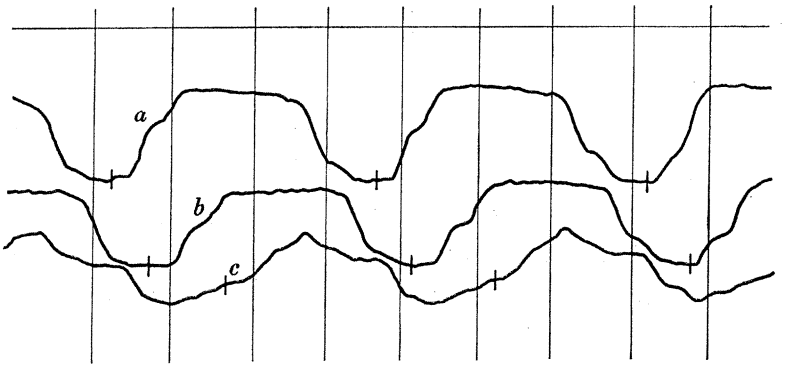

FIGURE 40. Typical temperature record. The three traces are the recorded temperatures at (*a*) $z = 8{\cdot}8$ cm, (*b*) $z = 7{\cdot}5$ cm, (*c*) $= 4{\cdot}0$ cm, under experimental conditions similar to those described with figure 39. The long vertical lines are timing marks, and the short vertical lines indicate point A (see figure 39).

Figure 39 is a schematic drawing of the top surface pattern for which $m = 4$. The drift of this pattern past the thermocouples at ω rad/s resulted in temperature profiles of the form illustrated in figure 40.

In figure 41 the profiles across AA at various positions z are given. They were obtained from the photographic records of the readings of the thermocouples by averaging over several 'cycles' so that the slight non-repeating features are absent. Further slight correc-

tions were made to allow for the fact that T_a and T_b differed slightly from their nominal values of 9 and 32 °C respectively.

The most conspicuous feature is the sharp temperature gradient in the regions vertically beneath the top surface 'jet' stream. The kink on the steep parts of the temperature profiles at and above $z/d = 0{\cdot}56$ always appeared, but it was not always to be found in the same position. It may, however, be important, and it has therefore been represented

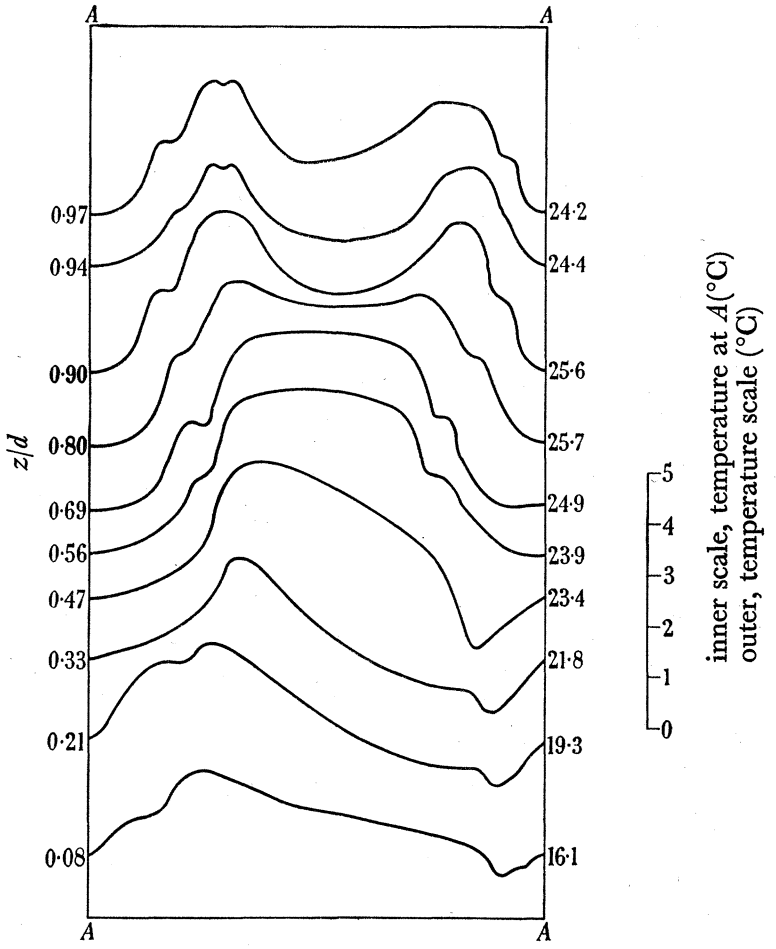

FIGURE 41. Temperature profiles along AA at different levels at height z above the bottom surface (see figure 39). The temperature scale is given on the right of the main diagram.

on these curves. The roughly 'square wave' profiles at $z/d = 0{\cdot}80$, $0{\cdot}69$ and $0{\cdot}56$ show that at these levels, the temperature in the regions directly under the top surface stagnant areas is nearly constant. There is a slight sag in the middle of the profile for $z/d = 0{\cdot}80$ and this sag is more pronounced at higher levels.

At $z/d = 0{\cdot}47$ the temperature profile has a distinct tilt and at lower levels, this tilt is even more pronounced. These profiles show that the inward flowing liquid is hotter than the outward flowing liquid.

The magnitude of the density fluctuations was estimated from these temperature data. In figure 42 a normalized density function $[\rho(T_b) - \rho(T)]/\Delta\rho$ is plotted as a function of $\sin(\pi z/2d)$, the length of the vertical lines indicating the amplitude of the density fluctuations.

The points were computed from the data of the second experiment—on 'spiral' flow—in which the only recorded temperature fluctuations were small and random. The amplitude at $z = 0$ was measured with a thermocouple which gave a direct reading (see § 3 (*e*)) but, owing to a galvanometer misalinement, no photographic record was obtained. We conclude from figure 42 that the mean density around a circle in the 'wave' flow régime and the constant density in the 'spiral' régime under otherwise similar conditions were about

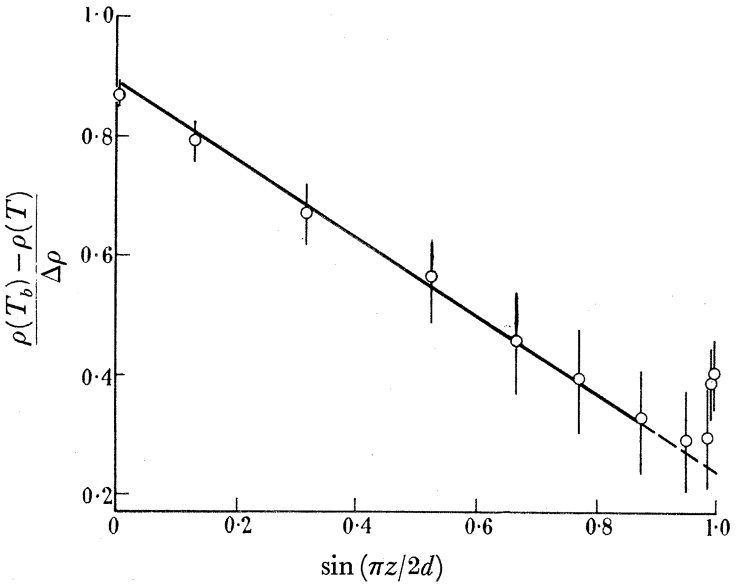

FIGURE 42. Analysis of temperature measurements. The ordinate is a normalized measure of the density $\rho(T)$ obtained from the temperature distribution data. The points correspond to the spiral flow régime, for which the experimental details are the same as those listed in figure 39, with the difference that $\Omega = 1{\cdot}18$ rad/s. The length of the vertical line at each point is equal to the amplitude of the density fluctuation in the wave-flow régime (see figure 39). The abscissa suggested itself through the apparently good linear relation between all those points for which $z/d < 0{\cdot}8$. The significance of this result is not understood.

equal. Furthermore, from $z = 0$ to $0{\cdot}69d$ the mean density varies linearly with sin $(\pi z/2d)$, the gradient being stable (see § 2(*d*)). However, within the upper reaches the density gradient was unstable, an effect which may well have been due to evaporative cooling from the top surface. In future work this 'end effect' region should be eliminated by taking suitable measures to prevent evaporation. It may be noteworthy that the sag in the temperature profiles, to which attention has already been directed, (figure 41) only occurred in the 'end effect' region.

It is likely that the difficulty in producing stable wave-flow patterns when d was less than about 3·5 cm was caused by evaporation and this may also have been responsible for systematic errors in measurements described in § 5(*d*).

In figure 43 the amplitude of the density fluctuations is plotted as a function of z/d. The maximum relative amplitude is 0·19, at $z/d = 0{\cdot}7$. Whether the decrease with z at $z/d > 0{\cdot}7$ is due to the 'end effect' cannot be judged from the present data.

In § 2 (*e*) two hypothetical quantities $\Delta_z \rho_1$ and $\Delta_H \rho_1$, were introduced in the discussion of a cylindrical vortex. The results given in figure 42 suggest that

$$\Delta_z \rho_1 \simeq 0{\cdot}6 \Delta\rho. \tag{5·11}$$

Furthermore, it seems reasonable to suppose that the density fluctuations around a circle at $r = \frac{1}{2}(b+a)$ should be approximately equal to the radial density contrast outside any boundary layers. Since the amplitude of this fluctuation is a function of z/d (see figure 43), ranging from $0{\cdot}03\,\Delta\rho$, at $z/d = 0$, to $0{\cdot}19\,\Delta\rho$, at $z/d = 0{\cdot}7$, it is suggested that

$$\Delta_H \rho_1 \simeq 0{\cdot}11 \Delta\rho, \tag{5·12}$$

0·11 being the arithmetic mean of the maximum and minimum values.

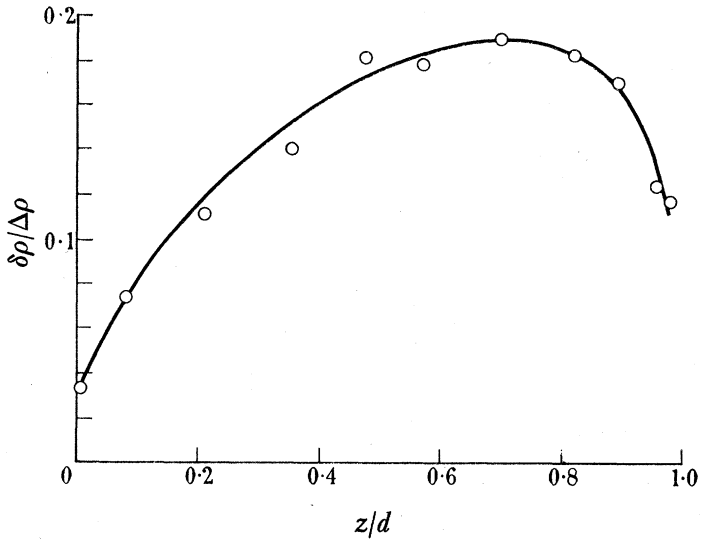

FIGURE 43. Amplitude of density fluctuations in the wave-flow régime. The ordinate is the length of the vertical line at each point of figure 42.

We tentatively conclude from these results that although the impressed density contrast $\Delta\rho$ was entirely horizontal (apart from slight 'end effects') only about 11% of the impressed contrast appeared across the main body of the fluid. The remainder must have appeared across the boundary layers near the two cylinders. The motion itself set up a very considerable stable density contrast in the vertical, amounting to 60% of $\Delta\rho$ (equation (5·11)).

6. Discussion of the experimental results

(a) *Dependence of* (ω/Ω) *on the impressed conditions*

If we take the empirical relation given by equation (5·5) and divide by the acceleration of gravity, g, on rearranging we obtain the dimensionless formula

$$\frac{\omega}{\Omega} = -10^{-2} \times (2{\cdot}91 \pm 0{\cdot}08) \frac{gd}{\frac{1}{2}\Omega^2(b^2-a^2)} \frac{\Delta\rho}{\rho_0}. \tag{6·1}$$

On combining this result with equation (5·3) and ignoring the negative sign in what follows, an alternative expression for the criterion for 'wave' or 'spiral' flow to occur is obtained, namely, that if

$$\Theta \equiv \frac{gd}{(b-a)^2\Omega^2} \frac{\Delta\rho}{\rho_0}, \tag{6·2}$$

we have 'wave' or 'spiral' flow according as

$$\Theta \lesseqgtr \Theta_{\text{crit.}} = 1{\cdot}58 \pm 0{\cdot}05. \tag{6·3}$$

The form of equation (6·1) is so chosen because $gd/\frac{1}{2}\Omega^2(b^2-a^2)$ is the ratio between the gravitational potential difference between the levels $z = 0$ and $z = d$ and the centrifugal potential change in going from $r = a$ to $r = b$.

Now compare equation (2·22) with equation (6·1). If we make the assumption that $\omega = \omega'$, that is to say, that twice the drift angular velocity of the waves is equal to the mean relative vorticity, then these two equations lead to the result that

$$\Delta_H \rho_1 = 4 \times 10^{-2}(2{\cdot}91 \pm 0{\cdot}08)\, h_1(a,b)\, f_1(a,b)\, \Delta\rho/(b^2-a^2). \tag{6·4}$$

Since h_1 and f_1 are functions of a and b only, if the assumption that ω and ω' are the same is correct, $\Delta_H \rho_1$ is probably independent of Ω.

The argument may be pursued a little further if we assume that

(i) $h_1(a,b) = (b-a)$ (see equation 2·19), and

(ii) $f_1(a,b) = \frac{1}{2}(b+a)$ (see equation (2·20)),

because then, according to equation (6·4)

$$\Delta_H \rho_1 = (0{\cdot}116 \pm 0{\cdot}003)\, \Delta\rho. \tag{6·5}$$

On considering this prediction in the light of the arguments leading to equation (5·12), the tentative conclusion may be drawn that the assumptions upon which equation (6·5) is based are probably correct, at least over the range covered by the present experiments. It will be possible to make direct tests of these assumptions when the temperature distribution has been studied in further detail.

Let us now try to understand the criterion for the onset of 'spiral' flow (see equation (6·3)). If we accept the foregoing assumptions as to the form of h_1 and f_1, it follows from equations (6·2) and (2·24) that Θ^{-1} has the character of a Richardson number.

In a recent paper, Kuo (1953) has discussed the theory of the onset of symmetrical flow in a rotating fluid contained in a cylinder of radius R filled to a depth d, with an impressed horizontal density contrast $\Delta\rho$ between the centre and the outside. Two parameters enter his analysis, one which might be termed the Kuo number Ku, where

$$Ku \equiv \frac{g\Delta\rho d^5}{\Omega^2 R^2 \kappa \nu \rho_0}, \tag{6·6}$$

and the other is a Taylor number appropriate to the problem (see equation (2·15)) namely

$$Ta = \Omega^2 d^4/\nu^2. \tag{6·7}$$

Two cases are discussed, corresponding to $d/R \ll 1$ and $d/R = 1$. Treating the problem as that of the stability against a symmetrical (meridional) perturbation of a fluid rotating initially as a solid body, Kuo finds that the situation is marginally stable when

$$Ku = Ku_{\text{crit.}}\,(Ta). \tag{6·8}$$

When $Ku < Ku_{\text{crit.}}$ perturbations of the form considered decay with time.

At high values of Ta, greater than about 10^3, Kuo's criterion is particularly simple, namely

$$Ku_{\text{crit.}} = 10{\cdot}6Ta, \tag{6·9}$$

or, on substituting for Ku and Ta from equations (6·6) and (6·7),

$$\left[\frac{gd\Delta\rho}{R^2\Omega^2\rho_0}\right]_{\text{crit.}} = 10{\cdot}6\frac{\kappa}{\nu}. \tag{6·10}$$

For water, the right-hand side of equation (6·10) is about 1·4, taking the average conditions of the experiments ($\nu = 10^{-2}\,\text{cm}^2/\text{s}$). If we compare equation (6·10) with equations (6·2) and (6·3), and write $R = b - a$, the agreement between the theory and experiment is remarkably good. Perhaps it is too good, in fact, to be too significant, when we consider the limitations of Kuo's analysis to relatively shallow systems. This result does suggest, however, that the temperature field may depend on the Prandtl number (see equation (2·17)), thus emphasizing the need for experiments on liquids other than water. Such experiments are in hand at present at Cambridge (see unpublished thesis by A. R. Smith).

A theoretical problem relating to the 'subcritical' flow has been studied quite recently by Davies (1956). Davies finds that

$$\frac{\omega}{\Omega} = -\frac{0{\cdot}45\,gd\Delta_H\rho_1}{b^2\Omega^2\rho_0} \tag{6·11}$$

($a = 0$ in his analysis, see his equation (6·1)). If we combine the experimental results given by equations (6·1) and (5·12), on setting $a = 0$ we find that not only is (ω/Ω) of the same form as that given by Davies's equation, but that the coefficient, 0·53, is not widely different from the theoretical value. Davies himself concluded that there was a large discrepancy between these coefficients, but this was due to a slight misinterpretation of the experimental data.

Davies was also able to discuss the dependence of the wave number m on the parameters of the problem, and found a measure of agreement between this part of his theory and some of Fultz's more recent measurements. However, the form of the theory is such that a profitable comparison with the results of § 5 (*e*) cannot be made at present.

(*b*) *The 'jet' stream*

The principal features of the 'jet' stream are its relatively small width and the strong temperature gradient across it, associated with relatively rapid flow within it. A necessarily rough application of the thermal wind equation (2·11) shows that the motion in the 'jet' stream is approximately geostrophic.

The essence of thermal convection is the transport of heat from the source to the sink. In our case the source and sink are the two bounding cylinders. Although convection can transport heat from one part of the fluid to another, heat can only enter and leave the system by conduction. If we make the assumption that heat enters and leaves the system only at points where the 'jet' stream touches the bounding cylinders (see figure 39), then the direction of conductive heat transport there agrees with the sense of the thermal gradient predicted by the thermal wind equation, namely, from right to left for an observer looking downstream.

Consider the heat flow in a hypothetical system of separate eddies, each of which extends across the annular space. If the flow satisfied the thermal wind equations, cyclonic eddies

would extract heat from the sink, and anticyclonic eddies would deliver heat to the source, which is an impossible state of affairs. Thus, we can see in a crude way how the 'wave flow' can perform its primary function of transporting heat, and why another very simple hypothetical type of flow could not.

The 'jet' stream is a phenomenon of which only a detailed dynamical theory will provide a satisfactory explanation. However, it is of some interest to attempt to account for its width. Consider the thermal history of a fluid particle within the 'jet' stream. Such a particle, when in the vicinity of the warm cylinder, receives heat from it by conduction. On leaving the vicinity of the warm cylinder, heat is transmitted by conduction to other parts of the fluid and on reaching the cold cylinder, conduction carries heat from the particle into the sink.

The equation of heat transport in a fluid is

$$\rho c\left\{\frac{\partial T}{\partial t}+(\mathbf{u}.\nabla)\ T\right\}=\chi\nabla^2 T. \tag{6·12}$$

Let δ_T be the order of magnitude of the thickness of those regions across which thermal conduction contributes significantly to the heat flow. If $\Delta T'$ is the order of magnitude of the temperature fluctuations associated with the flow, then the heat conduction term on the right-hand side of the last equation is of order $\chi\Delta T'/\delta_T^2$. The heat flow by convection in the main body of the fluid is given by the second term on the left-hand side of equation (6·12), which, by the arguments as to the nature of the Rossby number (see § 2 (*d*)), is of the order $(\rho_0 c\Delta T'\Omega Ro)$. Since the heat flow by conduction at those points where the 'jet' stream receives heat from the source must be the same as that carried off by convection,

$$\chi\Delta T'/\delta_T^2\approx\rho_0 c\Omega Ro\Delta T', \tag{6·13 a}$$

whence

$$\delta_T\sim(\kappa/Ro\Omega)^{\frac{1}{2}}. \tag{6·13 b}$$

On inserting representative values, namely, $\kappa=10^{-3}\,\mathrm{cm^2/s}$, $Ro=10^{-2}$ and $\Omega=5\,\mathrm{rad/s}$, in the last equation, we find that $\delta_T\sim10^{-1}\,\mathrm{cm}$, and of the same order of magnitude as the 'jet' stream width.

An interesting fact about rotating fluids might be pointed out here. Consider the thickness δ_V of a velocity boundary layer, which may be obtained by equating the magnitudes of the dynamical pressure forces outside the boundary layer to those inside. Since the former are balanced by Coriolis forces, and the latter by viscosity, it follows that

$$\delta_V\sim(\nu/\Omega)^{\frac{1}{2}}, \tag{6·14}$$

which in our case is of the order $10^{-2}\,\mathrm{cm}$. On combining this result with equation (6·13), we find that

$$\delta_V/\delta_T\sim(Pr.Ro)^{\frac{1}{2}}, \tag{6·15}$$

where Pr is the Prandtl number (see equation (2·17)). In non-rotating fluids, this ratio is simply $Pr^{\frac{1}{2}}$. It will be noted that from the arguments of § 2 (*d*) and § 2 (*e*), Kuo's criterion (equation (6·9)) may be re-stated in terms of the product $(Pr.Ro)$, and the foregoing arguments leading to equation (6·15) may have some bearing on the physical interpretation

of the factors influencing the transition between the principal types of flow described in this paper.

During that phase of the 'vacillation' cycle when the 'jet' stream is interrupted, separate eddies occur (see § 5 (*b*)). If our argument is correct about the impossibility of separate eddies existing indefinitely, then we have a lead towards a physical explanation of 'vacillation'. Presumably the heat flow should vary during the 'vacillation' cycle, and an investigation of this point should prove rewarding.

7. Conclusion

When the experiments here described were begun it was not possible to guess how close a bearing they would have on core hydrodynamics and geomagnetism. Now it is clear that extensions in several directions, especially into hydromagnetics, will have to be made if results of any geomagnetic interest are to be obtained. However, the unexpected similarity between the phenomena here described and some of the major features of the general atmospheric circulation makes the understanding of these phenomena a problem of meteorological importance. Valuable experimental work has been carried out already by Fultz and his collaborators but much remains to be done. 'Vacillation' is not understood and a theory of the 'jet' stream is still awaited.

Suggestions for future experiments have already been made in the appropriate context. Broadly, more detailed studies are required of cases already investigated in outline, and experiments using liquids other than water should be carried out. Such investigations can be guided by the theories of Davies, Kuo, and of others not explicitly referred to in the text.

Professor S. K. Runcorn's association with this work has been mentioned in the text. It remains to thank him and many others, especially Dr E. T. Eady, Mr T. V. Davies, and Dr D. Fultz for the benefit of their interest in the experiments. The technical skill of Mr L. H. Flavill of the Department of Geodesy and Geophysics, Cambridge, and of his assistants, deserves an especial mention, and finally, the author wishes to record his gratitude to the Department of Scientific and Industrial research for the award of a maintenance grant during the tenure of which this work was performed.

References

Brunt, D. 1939 *Physical and dynamical meteorology*. Cambridge: University Press.
Chandrasekhar, S. 1953 *Proc. Roy. Soc.* A, **217**, 306.
Davies, T. V. 1956 *Phil. Trans.* A, **249**, 27.
Eady, E. T. 1949 *Tellus*, **1**, 33.
Elsasser, W. M. 1956 *Rev. Mod. Phys.* **28**, 135.
Fischer, K. 1931 *Mitt. hydraul. Inst. Münch.* **4**, 7.
Fishenden, M. & Saunders, O. A. 1950 *An introduction to heat transfer*. Oxford: University Press.
Fultz, D. 1949 *J. Met.* **6**, 17.
Fultz, D. 1951 *a* *Compendium of meteorology*, p. 1235. American Meteorological Society.
Fultz, D. 1951 *b* *J. Met.* **8**, 262.
Fultz, D. 1953 *Proceedings of the first symposium on the use of models in geophysical fluid dynamics* (editor, R. R. Long).
Fultz, D. 1956 *Rep. Hydrodynam. Lab.* (*Univ. Chicago*), no. AFCRC–TR 56–259.

Hide, R. 1953*a* *Quart. J.R. Met. Soc.* **79**, 161.
Hide, R. 1953*b* *Proceedings of the first symposium on the use of models in geophysical fluid dynamics* (editor, R. R. Long).
Hide, R. 1956 *Progress in physics and chemistry of the earth* 1 (editors, Ahrens, Ramkana, Runcorn). London: Pergamon Press.
Inglis, D. R. 1955 *Rev. Mod. Phys.* **27**, 212.
Kuo, H. L. 1953 *Proceedings of the first symposium on the use of models in geophysical fluids dynamics* (editor, R. R. Long).
Long, R. R. 1952 *J. Met.* **9**, 187.
Rossby, C. G. & Willett, H. C. 1948 *Science*, **108**, 643.
Runcorn, S. K. 1954 *Trans. Amer. Geophys. Un.* **35**, 48.
Taylor, G. I. 1921 *Proc. Roy. Soc.* A, **100**, 114.
Thomson, J. 1892 *Phil. Trans.* A, **183**, 653.

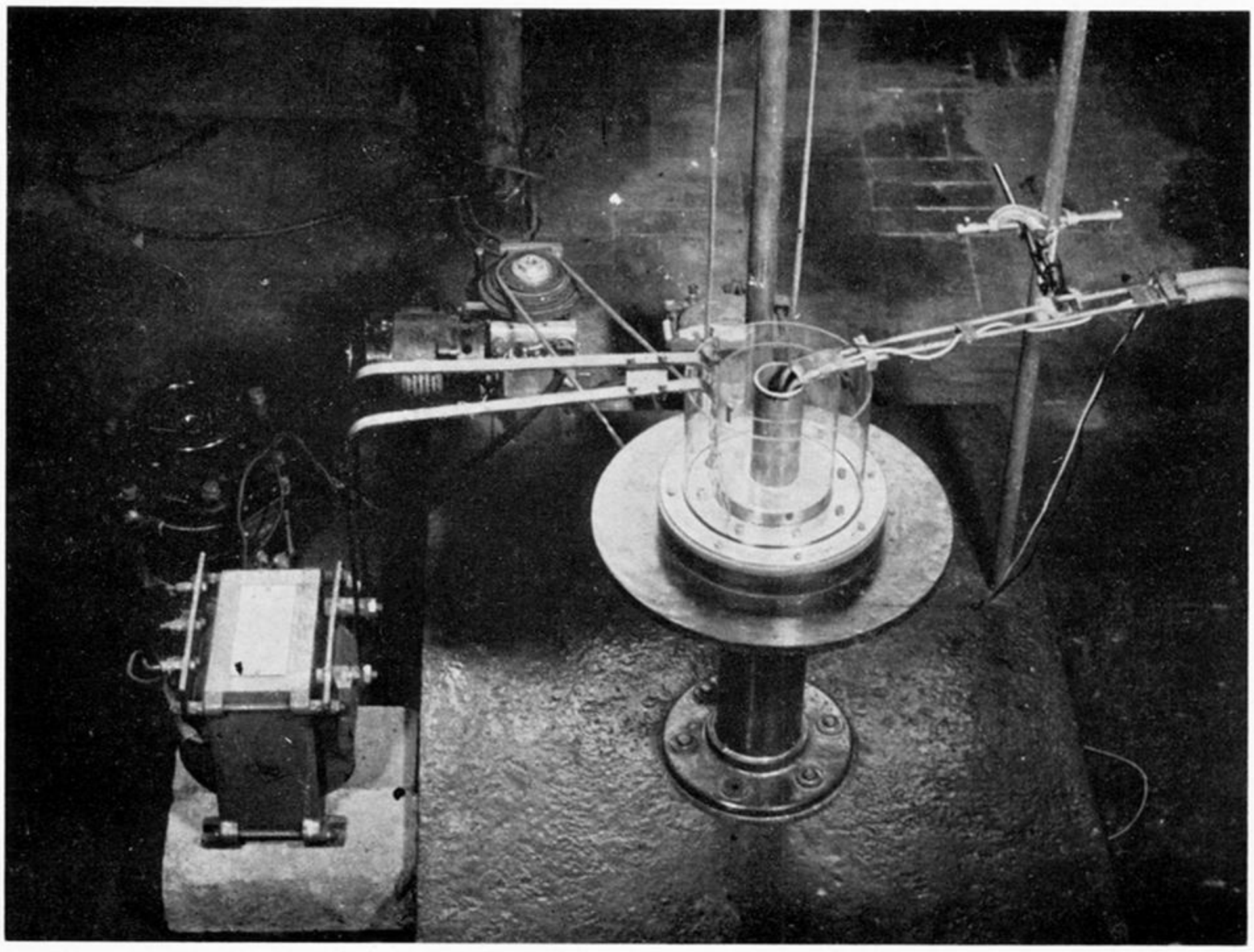

FIGURE 3. General view of the apparatus. Cooling water tubes are on the right. The transformer and Variac used to supply and vary the power to the heating element are on the left. The turn-table is mounted on a cast-iron plate. It was driven by the electric motor through a belt and pulley arrangement. The vertical post near the middle of the picture carries the rotoscope at the top (not seen in picture). Part of the belt drive to the rotoscope running parallel to the vertical post may be seen. To judge the scale, note that the transformer stands on two standard building bricks.

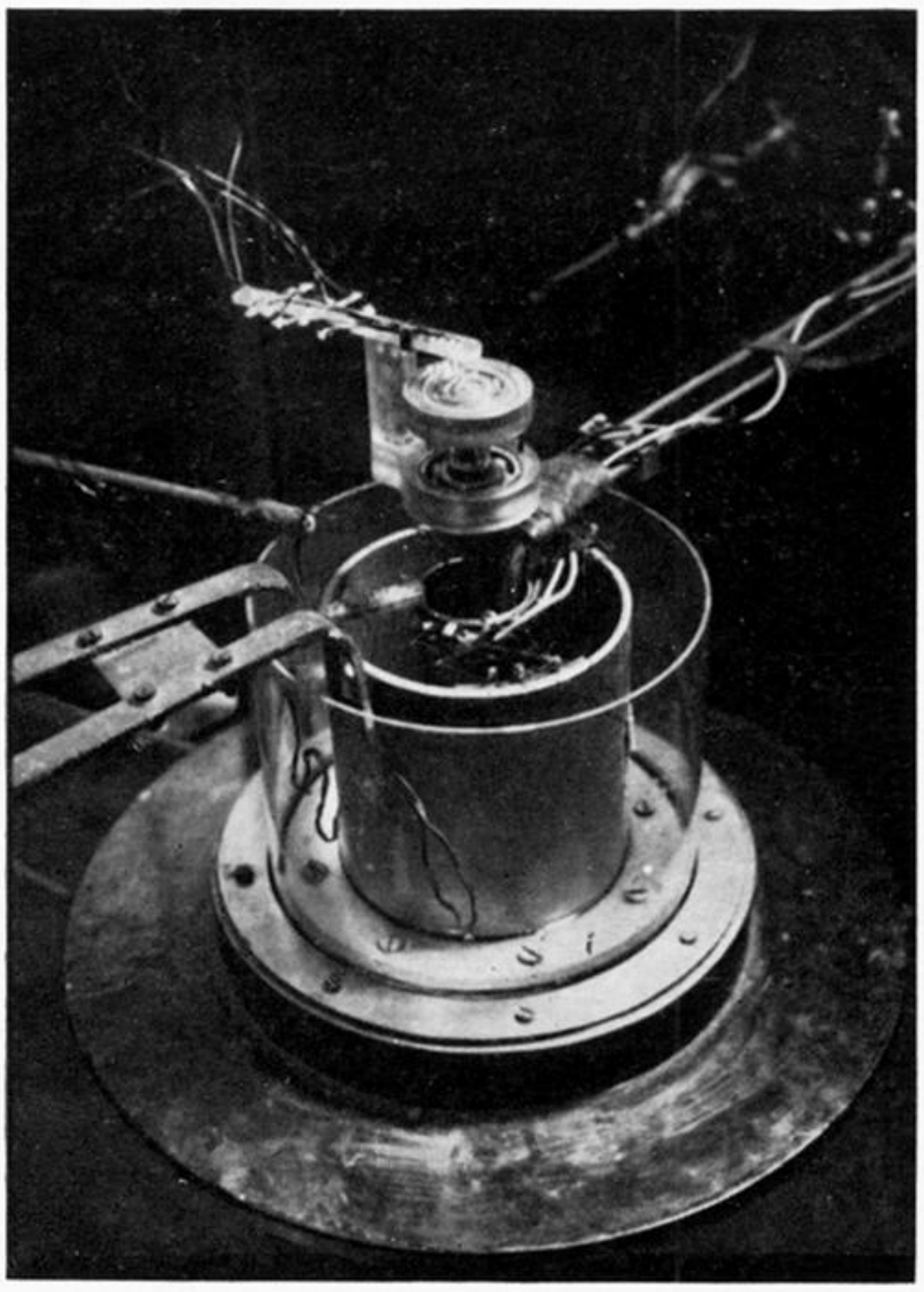

FIGURE 4. Convection chamber with thermocouples in position. The rotating mercury troughs are above the convection chamber. The Perspex bar carrying the non-rotating copper leads is rigidly attached to a ball-race arrangement directly underneath the mercury troughs. With this set-up, the troughs rotated accurately relative to the copper leads despite inevitable misalinement of the support carrying the troughs on the main turn-table.

(*Facing p.* 456)

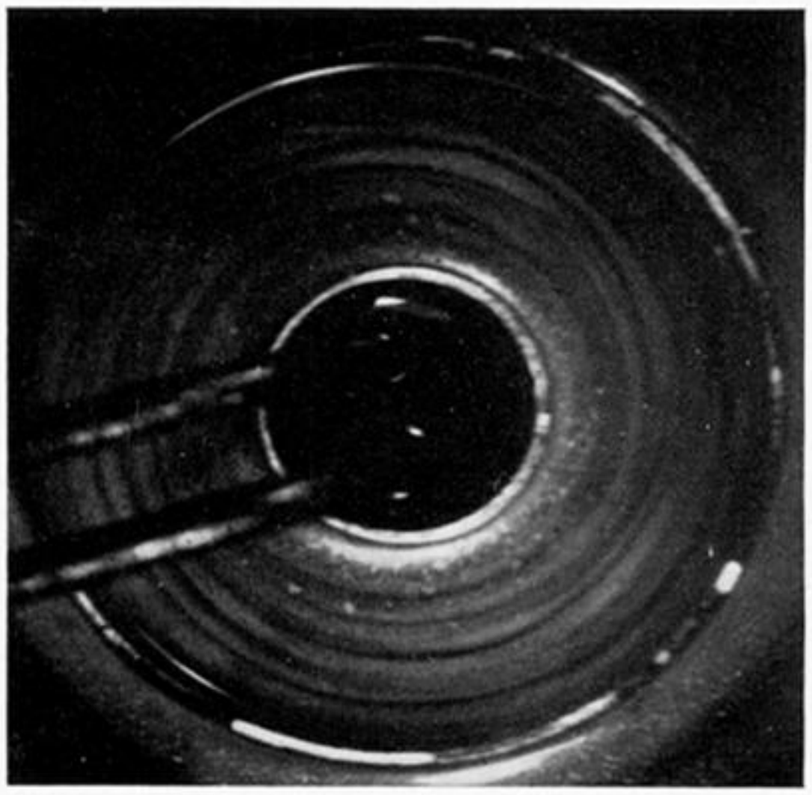

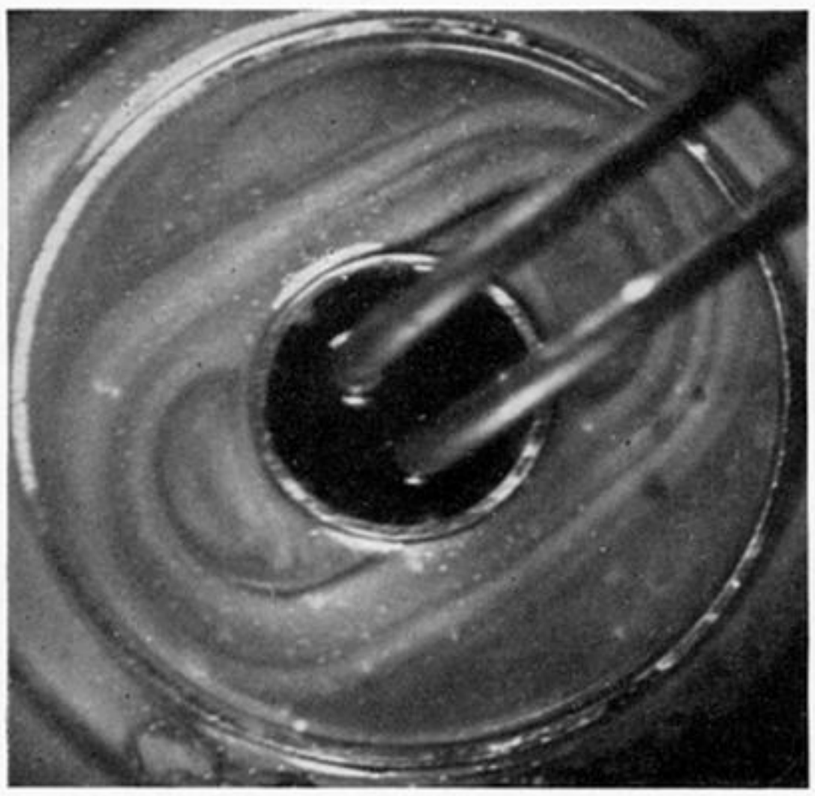

	(*a*)	(*b*)	(*c*)
Ω(rad/s)	1·56	1·56	3·48
$10^3\Delta\rho'/\rho_0$	−15·0	−4·2	−7·0
$X'(10^{-3}\ \mathrm{cm\ s^2})$	62	17	5·8

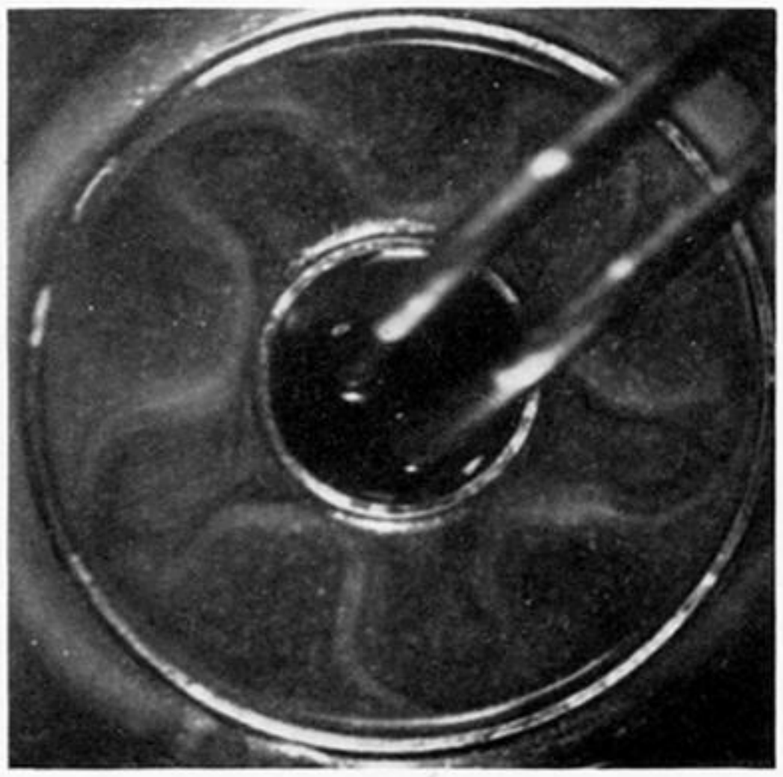

	(*d*)	(*e*)
Ω (rad/s)	3·48	4·71
$10^3\Delta\rho'/\rho_0$	−4·1	−4·3
$X'(10^{-3}\ \mathrm{cm\ s^2})$	3·4	1·9

FIGURE 5. Top-surface flow patterns at different values of X'. Aluminium powder was used as an indicator. In each case, $a = 1{\cdot}92$ cm, $b = 4{\cdot}85$ cm, $d = 10{\cdot}0$ cm. The sense of rotation is clockwise. (*a*) corresponds to low rotation, in which case the top-surface flow pattern is a spiral. The four remaining pictures are typical examples of the wave-flow régime, with wave number m going from 2 to 5.

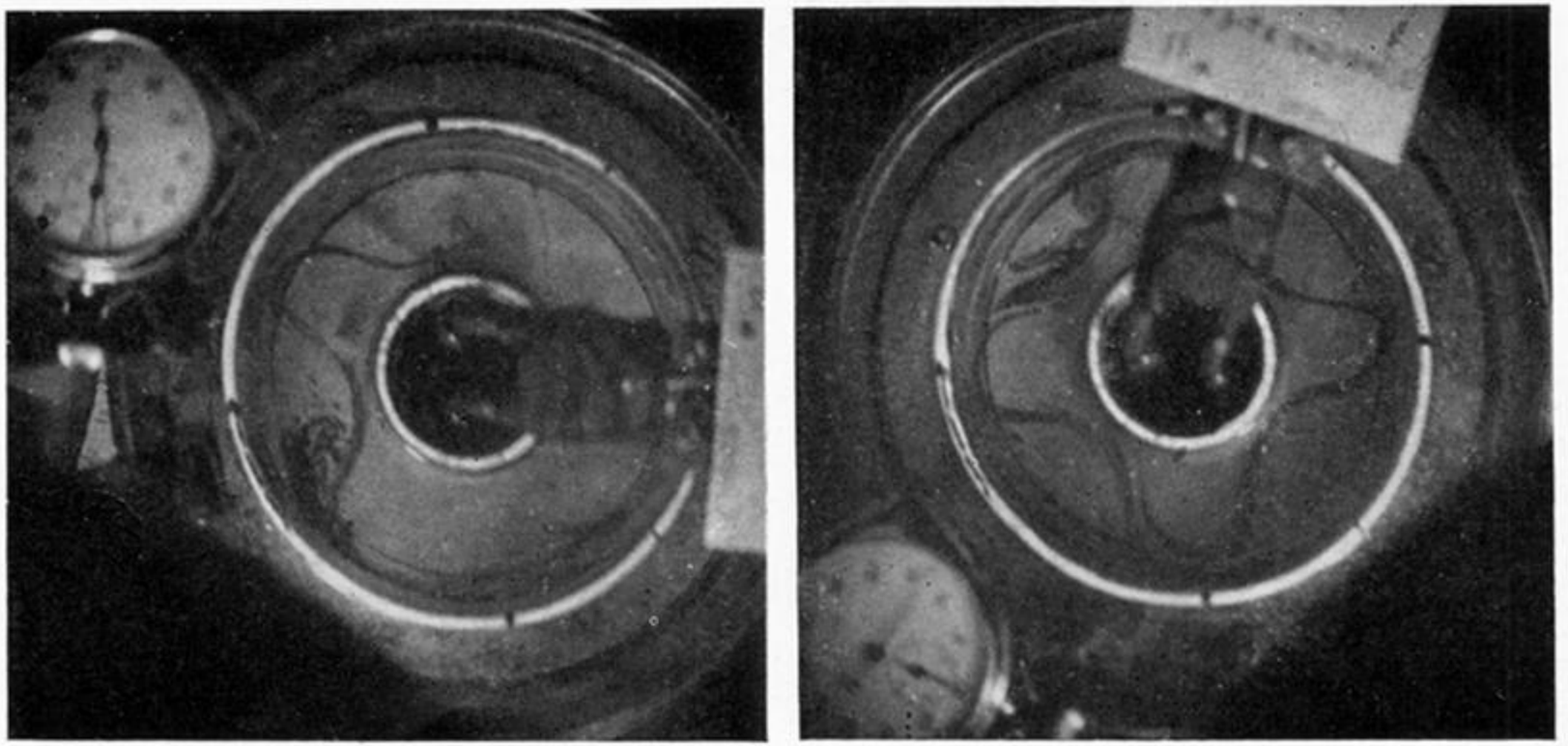

(*a*) (*b*)

FIGURE 6. Illustrating the angular drift motion of the wave-flow pattern. Experimental details: $a = 1{\cdot}92$ cm, $b = 4{\cdot}85$ cm, $d = 6{\cdot}7$ cm, $\Omega = 3{\cdot}48$ rad/s, $\Delta\rho'/\rho_0 = -9{\cdot}2 \times 10^{-3}$, $X' = 5{\cdot}1 \times 10^{-3}$ cm s^2, rotation clockwise. (*a*) was taken a few seconds after introducing a few crystals of malachite green dye at the top surface. (*b*) was taken 12 s later, and by comparing the dye streaks in the two pictures, the sense of motion in the 'jet' stream is seen to be eastward. Comparison of the positions of the whole pattern relative to the faint black arrowhead painted on the white rim of the middle cylinder, (at approximately '9 o'clock') shows that during the 12 s interval an eastward angular drift through 45° took place.

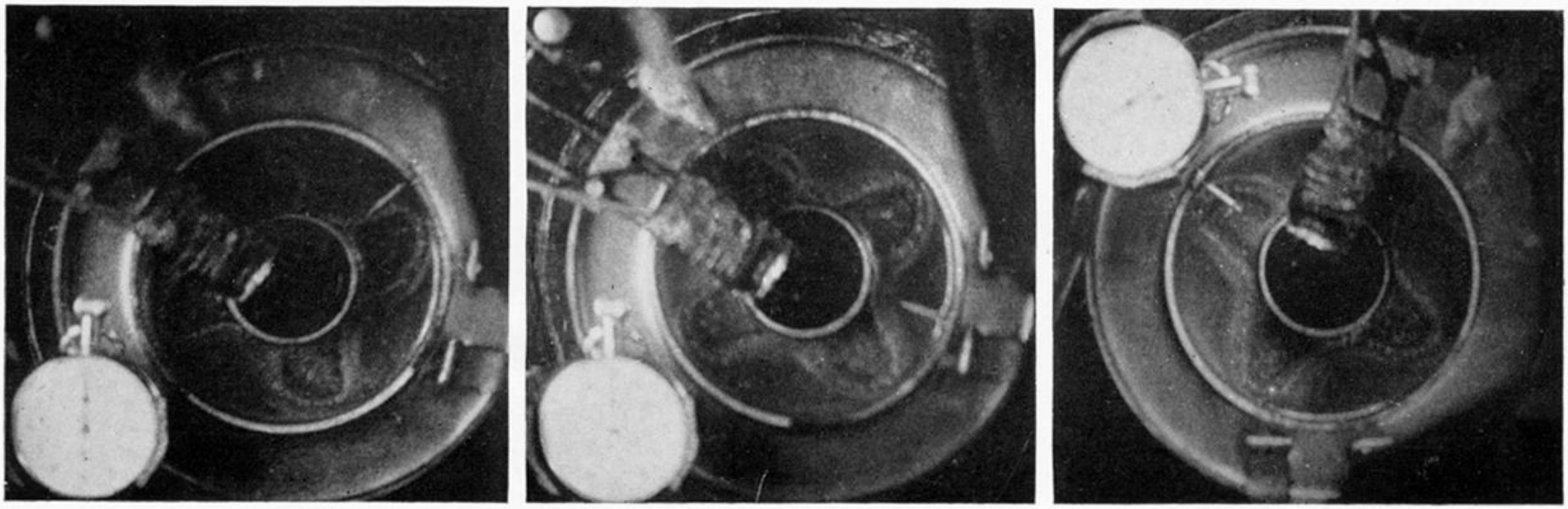

(*a*) $t = 0$ (*b*) $t = 10$ s (*c*) $t = 34$ s

FIGURE 7. Hot outer cylinder; angular drift eastward.

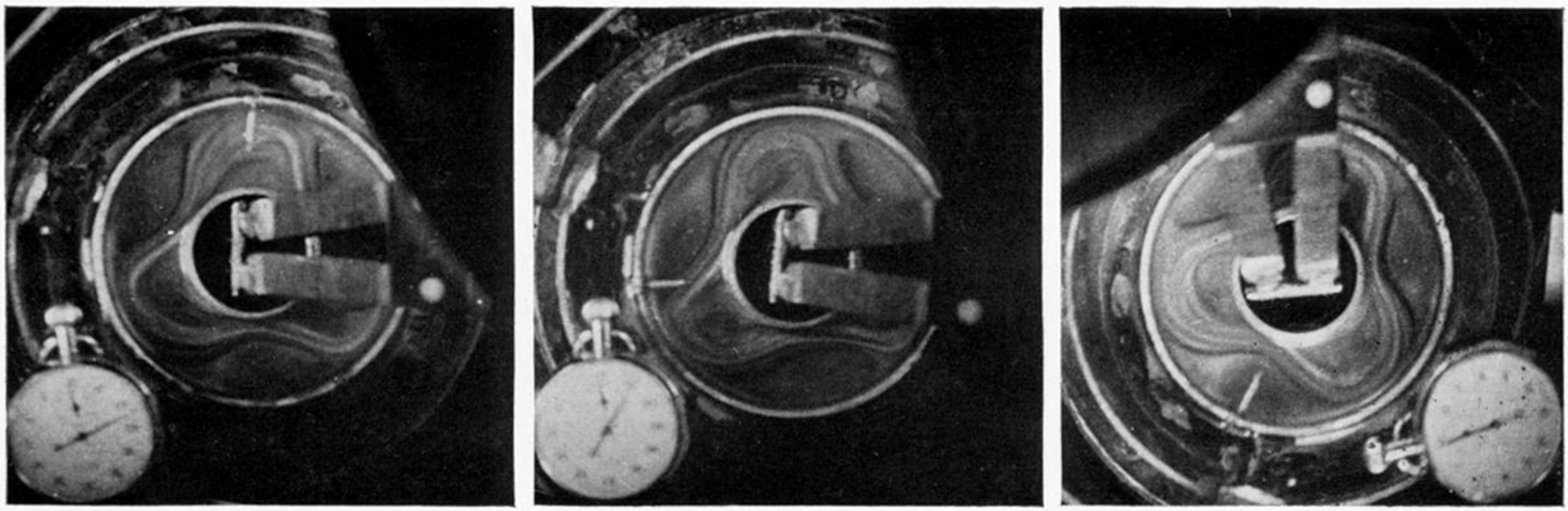

(*a*) $t = 48$ s (*b*) $t = 54$ s (*c*) $t = 61$ s

FIGURE 8. Hot inner cylinder; angular drift westward.

FIGURES 7 AND 8. Illustrating the dependence of the sense of the angular drift of the top-surface wave-flow pattern on the direction of the impressed temperature gradient. t is the stop-watch reading. The position of the pattern should be judged by noting the position of the wire attached to outer cylinder, at '12 o'clock' in figure 8(*a*). Experimental details:

	a (cm)	b (cm)	d (cm)	Ω (rad/s)	$\Delta\rho'/\rho_0$	X' (cm s^2)
figure 7	1·92	4·85	10·0	4·71	$-6{\cdot}2\times10^{-3}$	$+2{\cdot}8\times10^{-3}$
figure 8	1·92	4·85	10·0	3·48	$+8{\cdot}9\times10^{-3}$	$-7{\cdot}4\times10^{-3}$

Rotation clockwise; aluminium powder indicator.

FIGURE 9

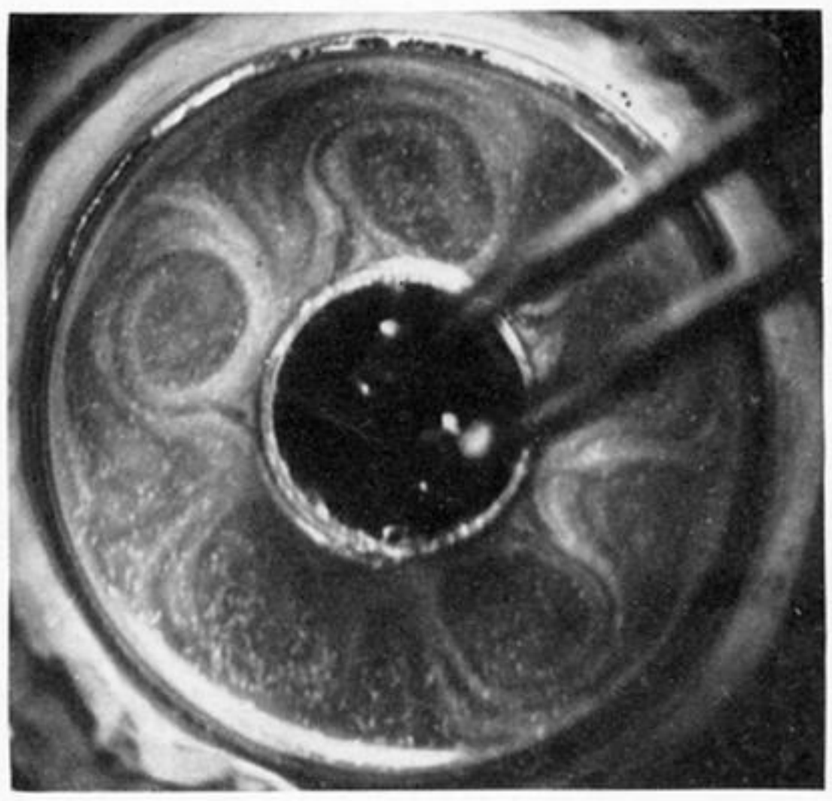

FIGURE 10*a*

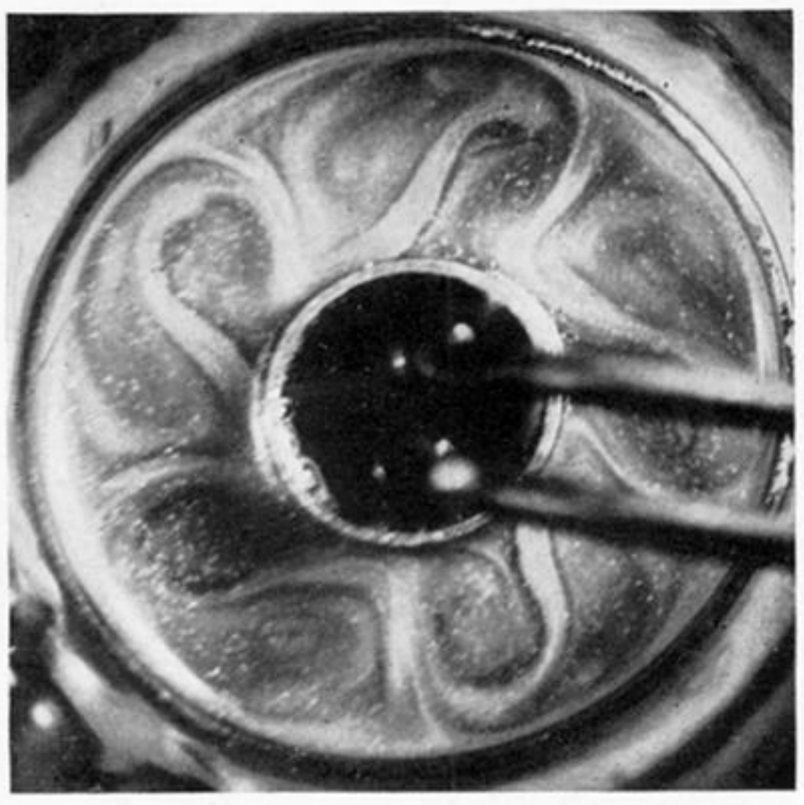

FIGURE 10*b*

Ω (rad/s)	8·23	8·23
$10^3\Delta\rho'/\rho_0$	−4·5	−9·0
$X'(10^{-3}$ cm s$^2)$	0·68	1·3
d (cm)	10·0	10·0

FIGURE 11

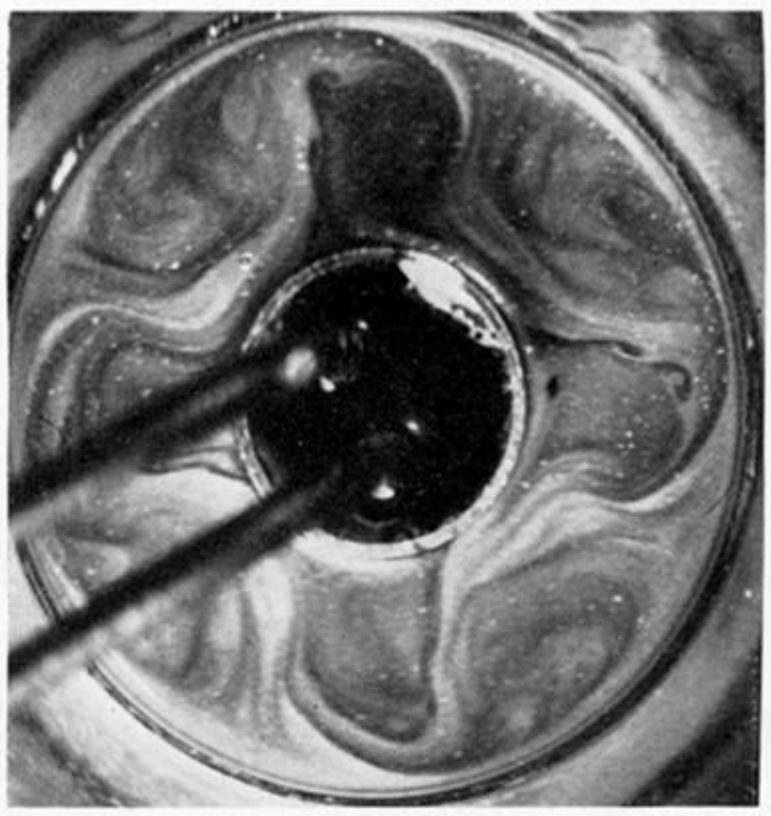

FIGURE 12

FIGURE 13

Ω(rad/s)	6·28	6·28	2·07
$10^3\Delta\rho'/\rho_0$	−9·0	−10·4	−2·8
$X'(10^{-3}$ cm s$^2)$	2·3	2·6	6·5
d (cm)	10·0	10·0	10·0

FIGURE 14

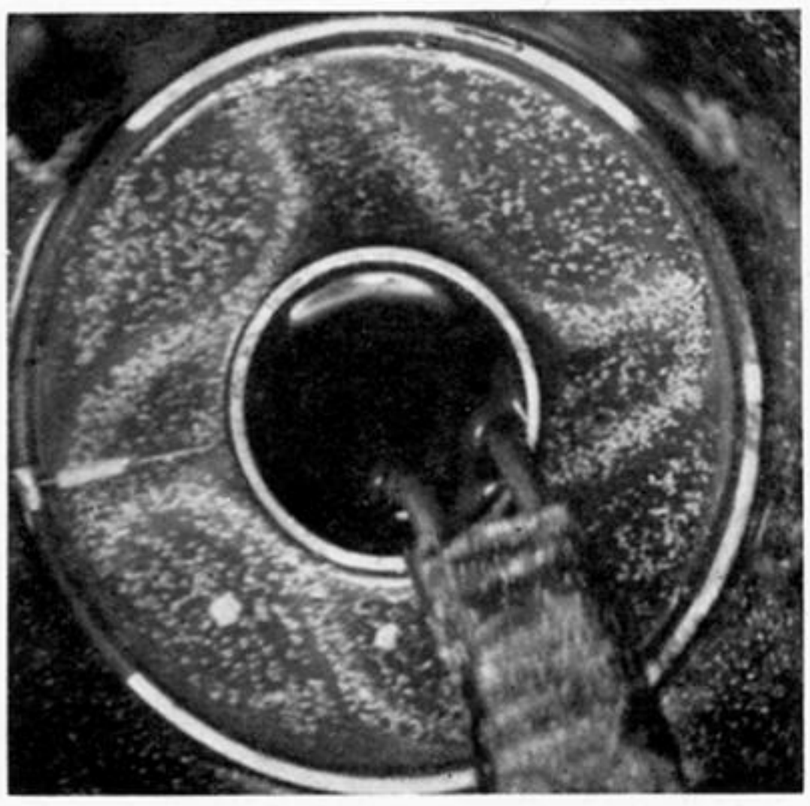

FIGURE 15

Ω(rad/s)	3·48	3·48
$10^3\Delta\rho'/\rho_0$	−7·0	−11·0
$X'(10^{-3}$ cm s$^2)$	2·2	3·4
d (cm)	3·8	3·8

FIGURES 9 TO 15. Further examples of the top-surface flow patterns with the inner cylinder radius $a = 1{\cdot}92$ cm. Rotation clockwise; aluminium powder indicator.

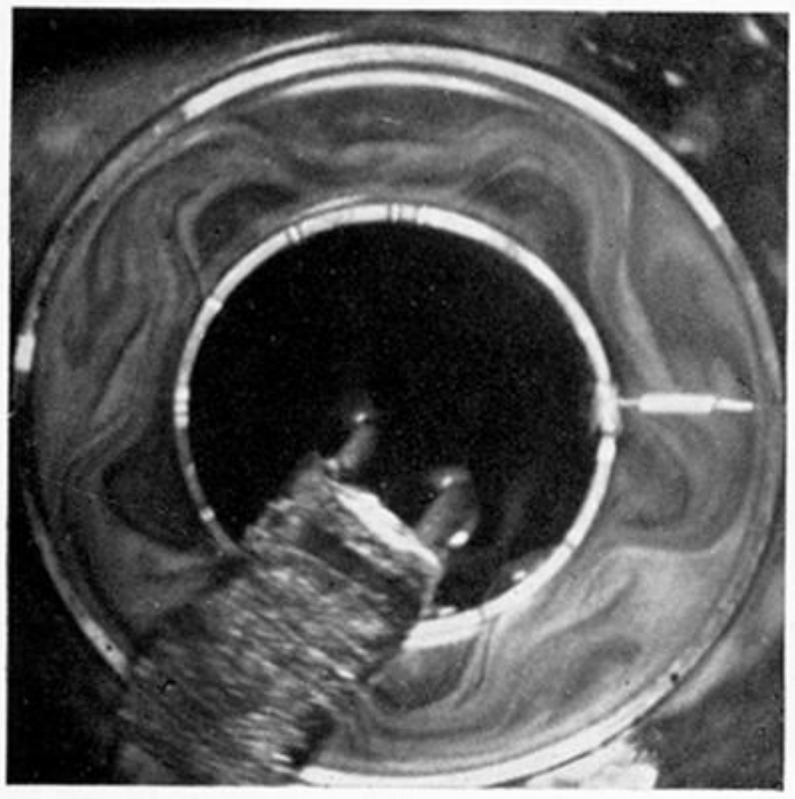

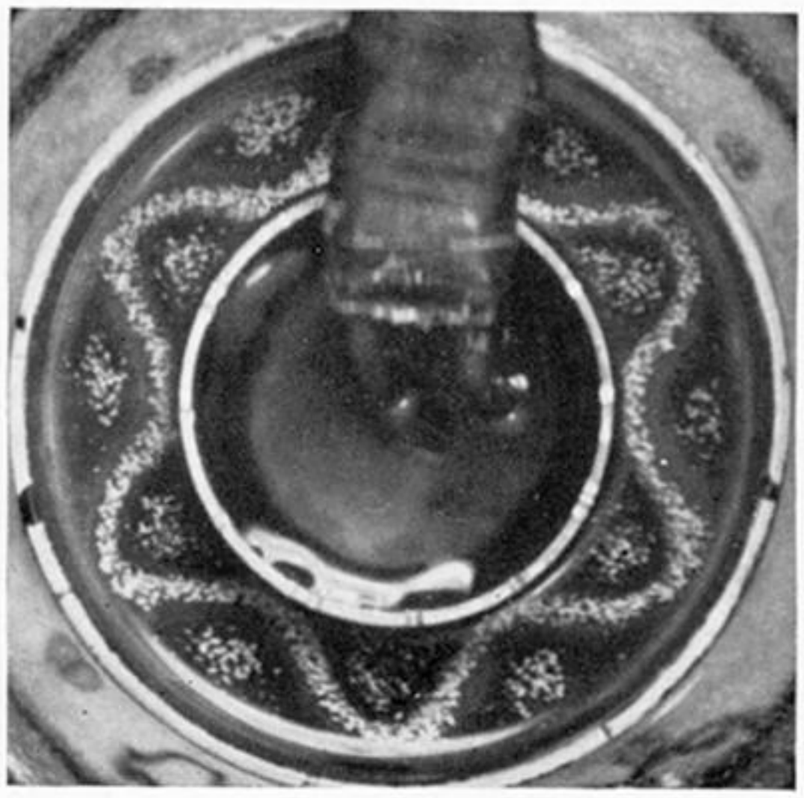

	FIGURE 16	FIGURE 17	FIGURE 18
Ω (rad/s)	6·28	4·71	4·71
d (cm)	10·0	8·5	8·5
$10^3\Delta\rho'/\rho_0$	−13·0	−5·6	−4·7
$X'(10^{-3}$ cm s$^2)$	3·3	2·1	1·8

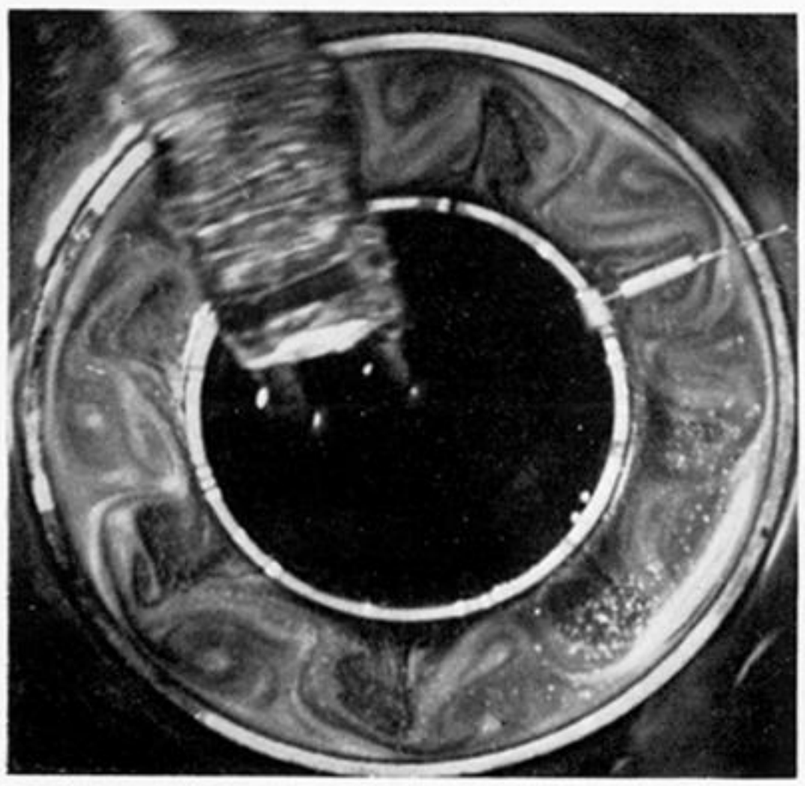

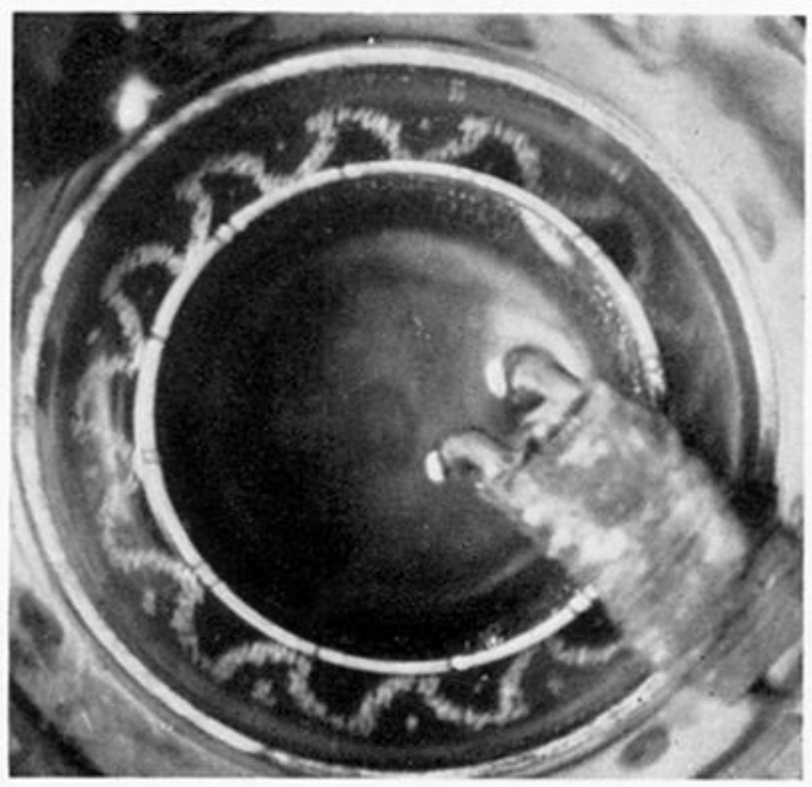

	FIGURE 19	FIGURE 20	FIGURE 21
Ω (rad/s)	6·28	4·71	6·28
d (cm)	10·0	6·5	6·3
$10^3\Delta\rho'/\rho_0$	−4·0	−1·7	−1·4
$X'(10^{-3}$ cm s$^2)$	1·0	0·5	0·23
		$m = 9$	$m = 13$

FIGURES 16 TO 19. Examples of top-surface flow patterns with the inner cylinder radius $a = 2{\cdot}85$ cm. In figures 17 and 18 agglomerations of aluminium particles which did not enter into suspension are clearly seen.

FIGURES 20 AND 21. Examples of top-surface flow patterns with the inner cylinder radius $a = 3{\cdot}54$ cm. Rotation clockwise; aluminium powder indicator.

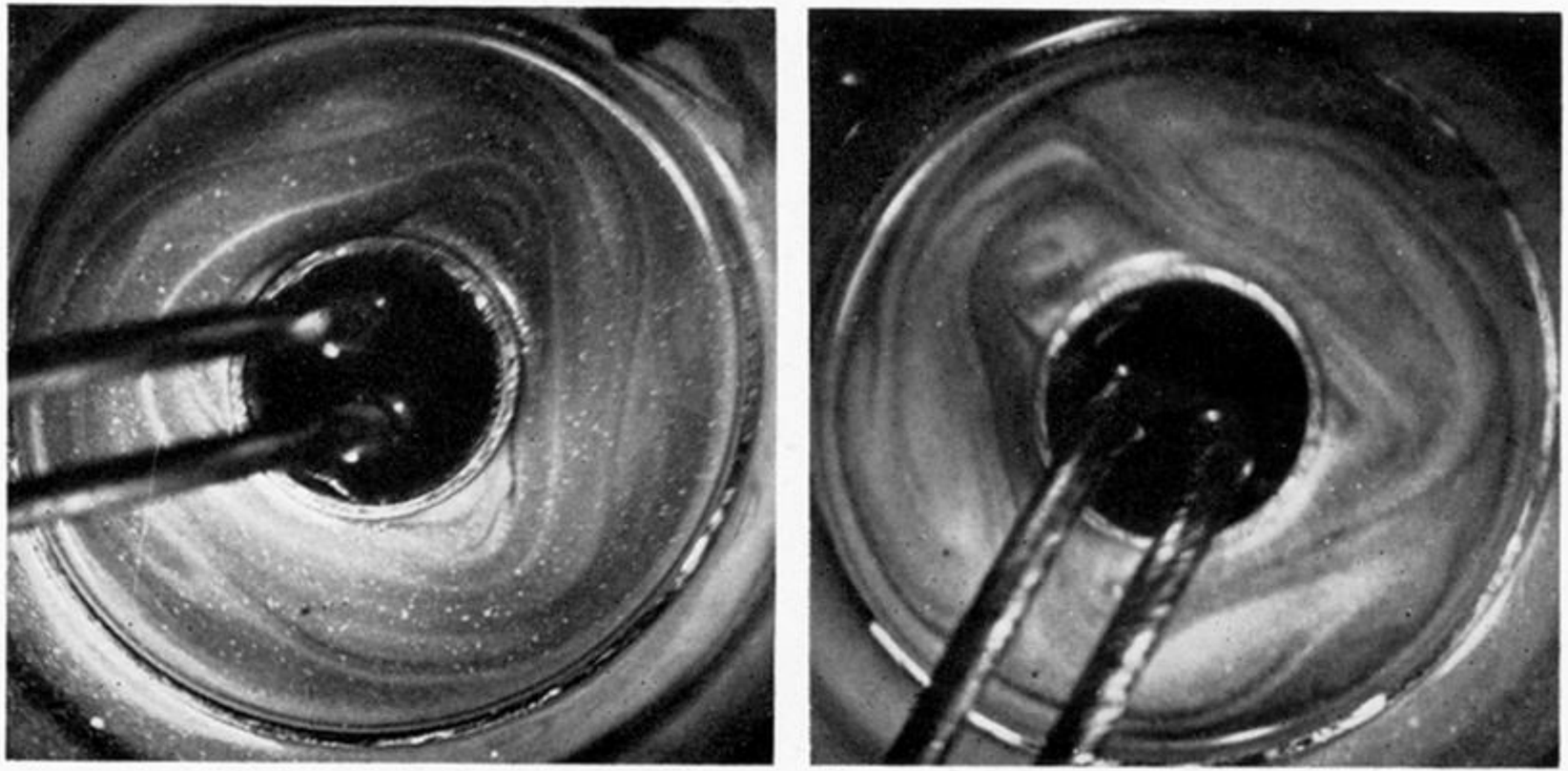

(*a*) (*b*)

FIGURE 22. Typical stages as wave flow changes its wave number from 4 to 3 (see § 4 (*a*)). Experimental details: $\Omega = 3{\cdot}48$ rad/s, $d = 10{\cdot}0$ cm, $a = 1{\cdot}92$ cm, $b = 4{\cdot}85$ cm, $\Delta\rho'/\rho_0 = -11{\cdot}5 \times 10^{-3}$, $X' = 9{\cdot}5 \times 10^{-3}$ cm s^2.

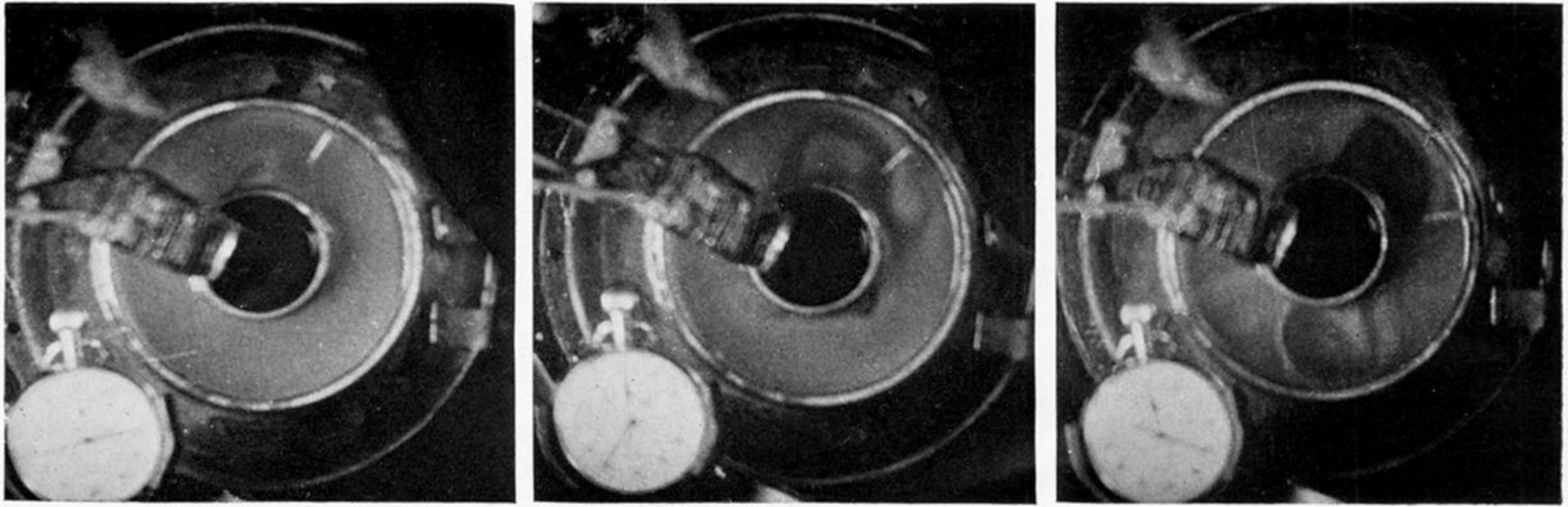

(*a*) $t = 16\ s$ (*b*) $t = 25\ s$ (*c*) $t = 40$ s

FIGURE 23. Illustrating the development of a typical wave-flow pattern (see § 4(*a*)). (*a*), (*b*) and (*c*) are photographs taken 16, 25 and 40 s, respectively, after the wave pattern had been destroyed by stirring.

FIGURE 24

FIGURE 25

FIGURE 24. A typical observation when the transition from wave to spiral flow occurs (see § 4 (*b*)). Experimental details: $\Omega = 2{\cdot}07$ rad/s, $d = 10{\cdot}0$ cm, $\Delta\rho'/\rho_0 = -8{\cdot}3 \times 10^{-3}$, $X' = 19 \times 10^{-3}$ cm/s^2, $a = 1{\cdot}92$ cm, $b = 4{\cdot}85$ cm, rotation clockwise.

FIGURE 25. To be compared with figure 5 (*a*) in order to illustrate the dependence of the 'tightness' of the spiral on X'. Experimental details: $\Omega = 0{\cdot}86$ rad/s, $d = 10{\cdot}0$ cm, $\Delta\rho'/\rho_0 = -9{\cdot}2 \times 10^{-3}$, $X' = 120 \times 10^{-3}$ cm/s^2, $a = 1{\cdot}92$ cm, $b = 4{\cdot}85$ cm, rotation clockwise.

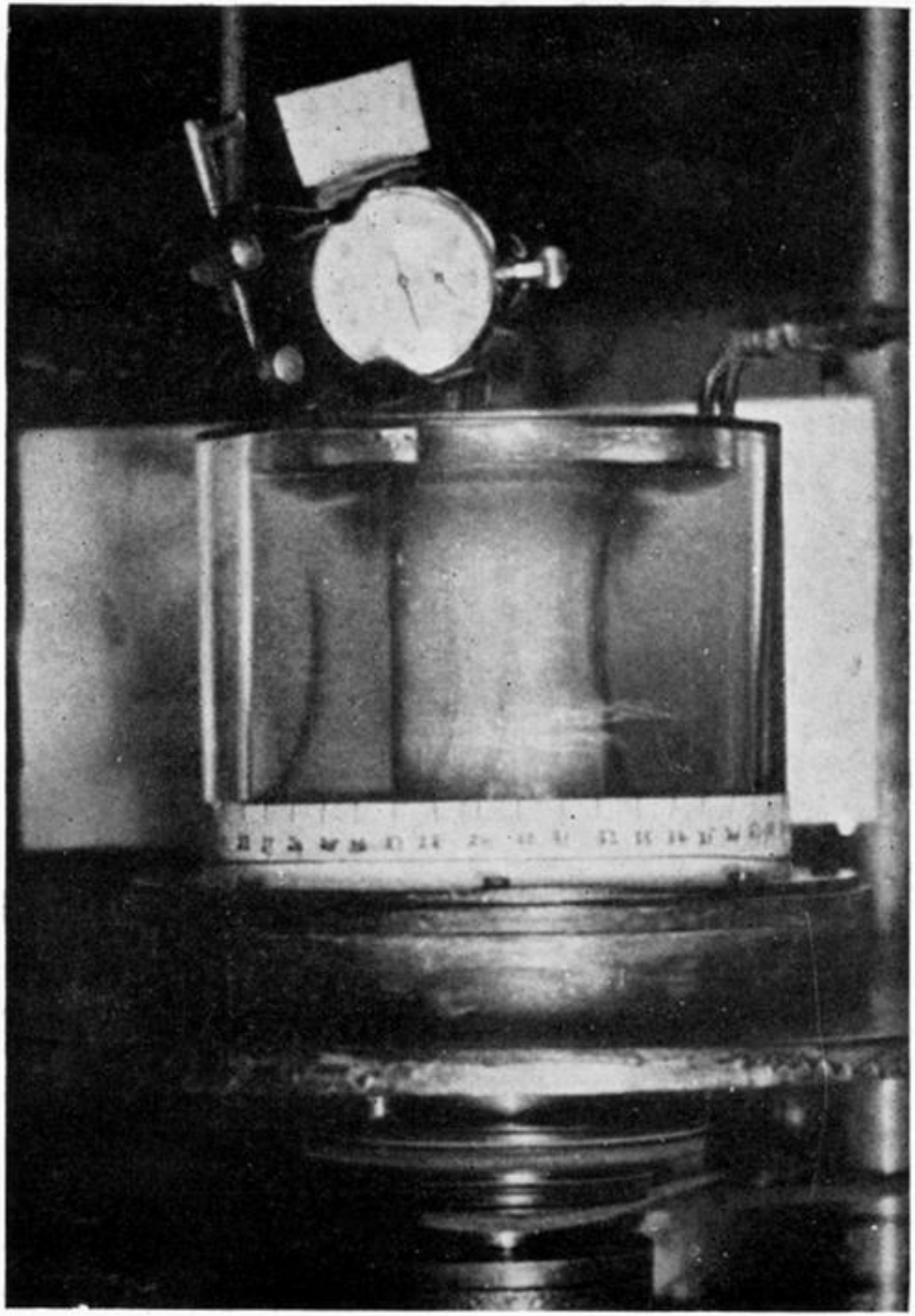

FIGURE 26. Some ink observations of the spiral flow régime through the side of the apparatus. For detailed description see the text (§ 4 (*b*)).

FIGURE 27

FIGURE 28

	Figure 27	Figure 28
Ω(rad/s)	2·07	3·48
$10^3\Delta\rho'/\rho_0$	−8·6	−8·6
$X'(10^{-3}$ cm s$^2)$	20	7·1
d(cm)	10·0	10·0

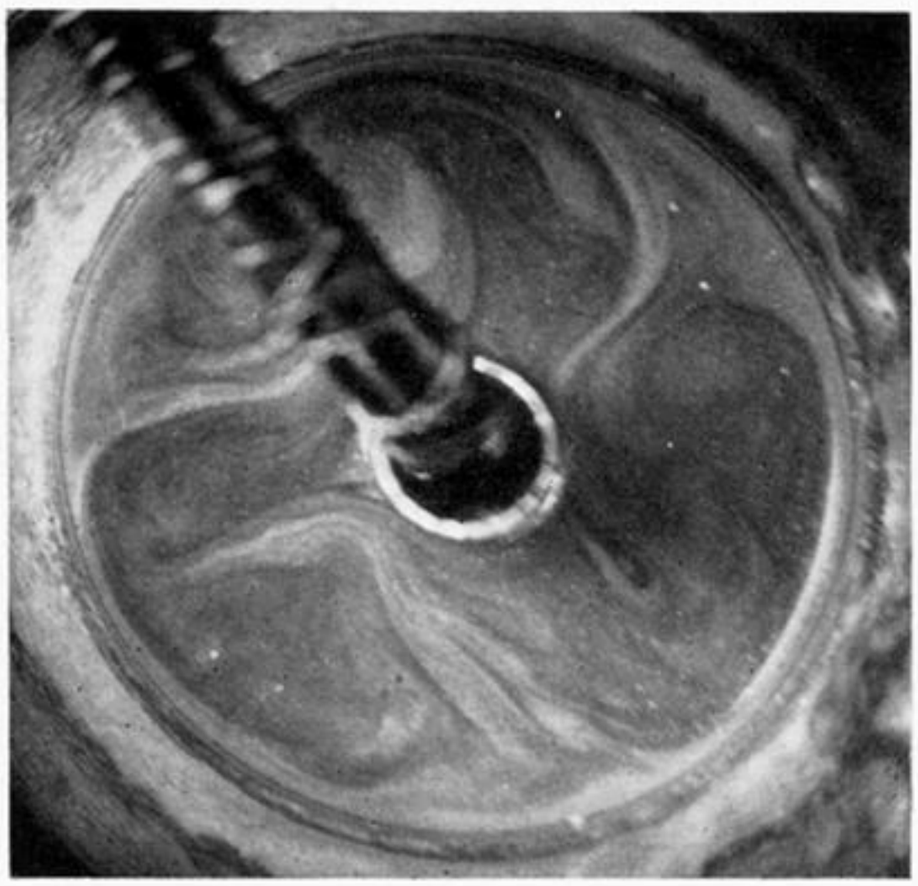

FIGURE 29

FIGURE 30

	Figure 29	Figure 30
Ω(rad/s)	6·28	6·28
$10^3\ \Delta\rho'/\rho_0$	−12	−4·7
$X'(10^{-3}$ cm s$^2)$	3·1	1·2
d (cm)	10·0	10·0

FIGURES 27 TO 30. Examples of the top-surface wave-flow pattern when the smallest ($a = 1{\cdot}06$ cm) inner cylinder was used.

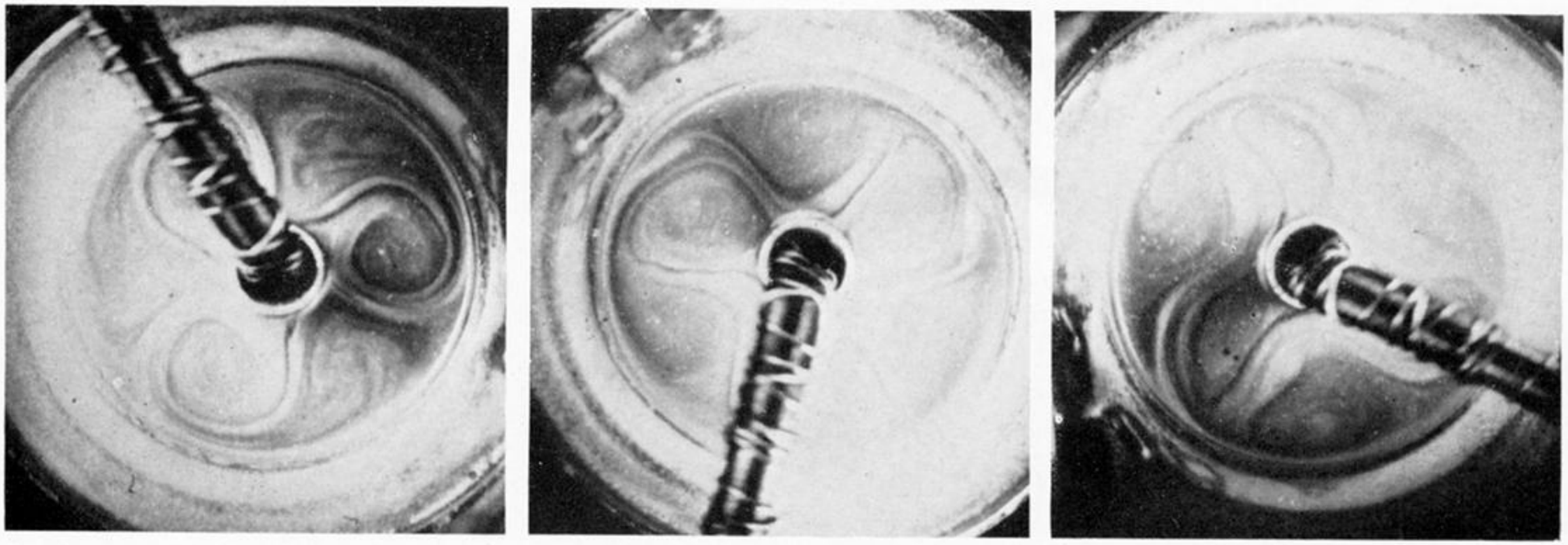

(*a*) $t = 0$ (*b*) $t = 6$ s (*c*) $t = 12$ s

(*d*) $t = 18$ *s* (*e*) $t = 24$ s (*f*) $t = 28$ *s*

FIGURE 31. 'Vacillation' cycle. Experimental details: $\Omega = 4{\cdot}71$ rad/s, $a = 1{\cdot}06$ cm, $b = 4{\cdot}85$ cm, $d = 10{\cdot}0$ cm, $\Delta\rho'/\rho_0 = -11{\cdot}8 \times 10^{-3}$, $X' = 5{\cdot}3 \times 10^{-3}$ cm s^2, rotation clockwise. For full description see text (§ 5 (*b*)).